

# FMCW Radar Applications for Automotive and Biomedical Applications

Thesis/Dissertation by

Vijith Varma Kotte

In Partial Fulfillment of the Requirements

For the Degree of

Doctor of Philosophy


King Abdullah University of Science and Technology

Thuwal, Kingdom of Saudi Arabia

©April, 2025

Vijith Varma

All rights reserved

 <https://orcid.org/0000-0003-1677-4249>

## ABSTRACT

### FMCW Radar Applications for Automotive and Biomedical Applications

Vijith Varma Kotte

Frequency Modulated Continuous Wave (FMCW) radar has emerged as a powerful sensing modality in both automotive and biomedical applications due to its ability to provide precise range, velocity, and Doppler measurements. This dissertation investigates novel methodologies to enhance FMCW radar's effectiveness in two critical domains: (1) forward-looking Synthetic Aperture Radar (SAR) imaging for automotive applications, and (2) biomedical monitoring for non-contact vital sign estimation and dehydration assessment. The proposed approaches leverage advanced signal processing, deep learning, and MIMO radar techniques to improve spatial resolution, classification accuracy, and robustness in real-world scenarios.

In the automotive domain, the research focuses on improving the azimuthal resolution of forward-looking SAR imaging by incorporating MIMO radar and deep learning-based reconstruction methods. Two key methodologies are proposed to address the resolution limitations of conventional SAR imaging techniques. The first approach employs an unsupervised Deep Basis Pursuit (DBP) framework, which enhances resolution through sparse recovery, significantly improving target scene clarity. The second approach utilizes a Convolutional Decoder for forward-looking MIMO SAR imaging, enabling high fidelity scene reconstruction in low measurement scenarios. These deep learning-based methods effectively mitigate the challenges associated with limited aperture size and mechanical scanning constraints, making them highly suitable for automotive radar applications, such as autonomous navigation and obstacle detection.

In the biomedical domain, this dissertation explores two critical applications: heart rate and breathing rate estimation from FMCW radar and non-invasive dehydration status monitoring. A novel joint estimation algorithm for high amplitude difference Doppler frequencies is introduced to accurately extract cardiac and respiratory signals from radar data, overcoming limitations posed by amplitude disparities in physiological motion. Additionally, a dehydration classification framework is developed using 77 GHz FMCW radar, combined with Wavelet Scattering Transform (WST) for feature extraction and machine learning classifiers for dehydration state identification. A custom fasting dataset is utilized for validation, demonstrating the feasibility of radar based hydration monitoring for continuous and remote healthcare applications.

The methodologies proposed in this dissertation are rigorously validated through extensive simulations and real-world experiments, showcasing their effectiveness in enhancing FMCW radar's performance for both automotive and biomedical applications. The findings contribute to the advancement of high-resolution radar imaging, physiological monitoring, and intelligent sensing technologies, paving the way for next generation autonomous systems and healthcare solutions.

## ACKNOWLEDGEMENTS

First and foremost, I would like to express my sincere gratitude to my supervisor, Prof. Tareq Y. Al-Naffouri, for offering me the opportunity to pursue my Ph.D. at KAUST and for allowing me to be a part of his outstanding research group. It has been a great privilege to work under his guidance. His unwavering support, insightful advice, and invaluable mentorship have been instrumental in shaping the direction of this research and in my growth as a researcher.

I am deeply grateful to Dr. Shahzad Gishkori, Dr. Sajid Ahmed, and Dr. Mahboob Ur Rahman for their assistance and continuous support throughout my research journey. Their guidance, technical expertise, and constructive feedback have played a crucial role in overcoming challenges and refining the ideas presented in this dissertation. I truly appreciate their dedication and the time they have invested in my work.

I would also like to extend my heartfelt appreciation to all those who have contributed, directly or indirectly, to the completion of this thesis. Whether through discussions, collaborations, or words of encouragement, their support has been invaluable.

Finally, my deepest gratitude goes to my family and friends for their unconditional love, patience, and unwavering support. Their encouragement and belief in me have been a constant source of motivation throughout this journey. This work would not have been possible without them.

## Contents

<b>Abstract</b>	<b>2</b>
<b>Acknowledgements</b>	<b>4</b>
<b>List of Figures</b>	<b>8</b>
<b>List of Tables</b>	<b>11</b>
<b>1 Introduction</b>	<b>12</b>
1.1 Background and Motivation . . . . .	12
1.2 Role of FMCW Radar in Modern Applications . . . . .	13
1.3 Research Objectives . . . . .	14
1.3.1 Automotive Applications . . . . .	15
1.3.2 Biomedical Applications . . . . .	15
1.4 Organization of the Thesis . . . . .	16
<b>2 Fundamentals of FMCW Radar</b>	<b>17</b>
2.1 Principles of FMCW Radar . . . . .	17
2.2 Range, Doppler, and Angle Estimation in FMCW Radar . . . . .	18
2.2.1 Range Estimation . . . . .	20
2.2.2 Doppler Estimation . . . . .	21
2.2.3 Angle Estimation . . . . .	22
<b>3 FMCW Radar for Automotive Applications</b>	<b>23</b>
3.1 Introduction . . . . .	23
3.2 Contributions . . . . .	26
3.3 MIMO SIGNAL MODEL . . . . .	27
3.4 FL-MIMO-SAR METHODOLOGY . . . . .	32
3.4.1 FL-MIMO-SAR Antenna Pattern . . . . .	32
3.5 Proposed Un-supervised Methodology . . . . .	36
3.5.1 Deep Basis Pursuit . . . . .	37
3.5.2 Convolutional Decoder . . . . .	41
<b>4 FMCW Radar of Bio-Medical Applications</b>	<b>43</b>
4.1 Heart Rate and Breathing Rate Estimation . . . . .	44

4.1.1	Introduction . . . . .	44
4.1.2	Contributions . . . . .	46
4.1.3	Signal Model . . . . .	47
4.1.4	Proposed Methodology . . . . .	51
4.2	Non-Contact Dehydration Status Monitoring . . . . .	61
4.2.1	Introduction . . . . .	61
4.2.2	Contributions . . . . .	62
4.2.3	Signal Model . . . . .	63
4.2.4	Proposed Methodology . . . . .	66
<b>5</b>	<b>Results and Discussion</b>	<b>70</b>
5.1	Results of FL-MIMO SAR Imaging . . . . .	70
5.1.1	Simulated Results . . . . .	71
5.1.2	Experimental Results . . . . .	78
5.1.3	Simulated Results for ConvDec . . . . .	80
5.2	Results of Heart Rate and Breathing Rate Estimation . . . . .	82
5.2.1	Simulated Results . . . . .	83
5.3	Results of Dehydration Status Monitoring . . . . .	90
5.3.1	Data Acquisition . . . . .	90
5.3.2	Experimental Results . . . . .	93
<b>6</b>	<b>Conclusion and Future Research Directions</b>	<b>97</b>
6.1	Summary of Contributions . . . . .	97
6.2	Limitations of the Study . . . . .	98
6.3	Future directions . . . . .	99
6.4	Final Remarks . . . . .	100
	<b>References</b>	<b>102</b>
	<b>Appendices</b>	<b>110</b>



## LIST OF FIGURES

3.1	MIMO array schematic. . . . .	28
3.2	FL-MIMO-SAR schematic. . . . .	31
3.3	FL-MIMO-SAR :Synthetic antenna array for a LA. . . . .	33
3.4	Composite antenna pattern (Normalized) for different Look Angles. . . . .	33
3.5	Composite antenna pattern (Normalized) for different number of MIMO virtual elements. . . . .	34
3.6	Proposed Structure for FL-MIMO-SAR Imaging . . . . .	37
3.7	DBP Architecture for estimating $\mathbf{x}^{(i)}$ . . . . .	37
3.8	Proposed Structure. . . . .	41
4.1	System model of the considered FMCW radar. . . . .	48
4.2	Proposed methodology. . . . .	51
4.3	Datacube representation of FMCW Intermediate Frequency (IF) signal with array dimension $n_R$ , and slow-time samples $N_s$ . . . . .	54
4.4	The transmitted and reflected signals from the patient's chest will vary depending on the body's dehydration level, which acts as a channel. Different frequencies will experience varying levels of attenuation based on the hydration status. . . . .	65
4.5	Proposed Methodology for dehydration classification. . . . .	66
5.1	Architecture of the CNN-based Denoiser. . . . .	71
5.2	Final reconstructed image results for simulated data using (a) Tar- get Scene (b) MF based FL-MIMO-SAR Imaging (c) Compressive sensing based FL-MIMO-SAR Imaging (d) DBP based FL-MIMO- SAR Imaging. . . . .	72
5.3	Comparison of simulated data Y-magnitude plots for MF, CS and DBP based FL-MIMO-SAR Imaging. . . . .	73
5.4	Comparison of MSE (at cross-range gap between the targets) on simulated data, for MF-based, CS-based and DBP-based FL-MIMO- SAR Imaging. . . . .	73
5.5	MSE plot of simulated target for DBP-based method for different SNRs. . . . .	74

5.6	Comparison of MSE plots for simulated data using MF-based, CS-based, and DBP-based methods at SNRs: (a) 0dB, (b) -10dB, (c) -20dB. . . . .	75
5.7	Comparison of PSFs for a point target using MF-based, CS-based, and DBP-based FL-MIMO-SAR Imaging. . . . .	76
5.8	Comparison of Y-magnitude plots on simulated data for DBP based FL-MIMO-SAR Imaging for different spacing between the targets along Y-axis. . . . .	76
5.9	Y-magnitude plots on simulated data of three point targets using proposed DBP based FL-MIMO-SAR Imaging for different spacing between the targets along Y-axis. . . . .	77
5.10	(a) Two targets (b) 77 GHz MIMO radarbook (c) FL-MIMO-SAR experimental setup. . . . .	78
5.11	Final reconstructed image results for experimental real data using (a) MF based FL-MIMO-SAR Imaging (b) Compressive sensing based FL-MIMO-SAR Imaging (c) DBP based FL-MIMO-SAR Imaging. . . . .	79
5.12	ConvDecoder architecture with up-sampling, convolutional, ReLU, and batch normalization layers. . . . .	80
5.13	Reconstructed image results (a) Target Scene (b) MF-based FL-MIMO-SAR Imaging (c) DBP-based FL-MIMO-SAR Imaging (d) ConvDecoder-based FL-MIMO-SAR Imaging. . . . .	81
5.14	Reconstructed image results considering only few aperture steps (a) DBP-based FL-MIMO-SAR Imaging (b) ConvDecoder-based FL-MIMO-SAR Imaging. . . . .	82
5.15	Range and DOA estimations for the scenario of five targets using (a) FFT, (b) MUSIC, and (c) Capon. . . . .	84
5.16	Doppler frequencies estimation using proposed method of three moving targets. (a) Target located at 9m introducing Doppler frequencies of -1Hz and -2Hz, (b) target located at 5m introducing Doppler frequencies of -1Hz and 4Hz, and (c) target located at 3m introducing Doppler frequencies of 1Hz and 2.5Hz. . . . .	84
5.17	Comparison of FFT, MUSIC, Yule-AR, and proposed Capon-based method for the Doppler frequency estimation of target 1 located at a distance of 3m and at an angle of $-30^\circ$ . The SNR = 0dB and the target induces Doppler frequencies of 1 Hz and 2.5 Hz. . . . .	85

5.18	Comparison of Doppler frequency estimation using FFT, MUSIC, and proposed Capon method for a target is located at the range 3m and angle $-30^\circ$ with SNR = 0dB and $\beta_2 = \beta_1/2$ . In the first row $f_{d_1} = 4\text{Hz}$ , $f_{d_2} = 1\text{Hz}$ , and $\Delta f_d = 3\text{Hz}$ , while in the second row $f_{d_1} = 1\text{Hz}$ , $f_{d_2} = 1.5\text{Hz}$ , and $\Delta f_d = 0.5\text{Hz}$ . . . . .	86
5.19	Comparison results of Doppler frequencies estimation with FFT (1st Column), MUSIC (2nd Column), and Yule-AR(3rd Column), and proposed method (4th Column) for a target placed at a distance of 3m and at an angle $-30^\circ$ with SNR = 0dB and Doppler frequencies 2 Hz and 1 Hz for different ratios of $\beta_1$ and $\beta_2$ . . . . .	87
5.20	MSE comparison for Doppler estimation using FFT, MUSIC, Yule-AR, and proposed Capon method for a target is located at the range 3m and angle $-30^\circ$ for a range of SNRs (-20dB to 10dB) with doppler frequencies $f_{d_1} = 1.333\text{Hz}$ and $f_{d_2} = 2.333\text{Hz}$ . . . . .	89
5.21	Experimental setup for dehydration monitoring using FMCW radar data collection for (a) Fasting Dataset and (b) Sports Dataset (c) Inras 77 GHz FMCW radar. . . . .	91
5.22	Confusion matrix for Naive Bayes . . . . .	96
5.23	Confusion matrix for SVM . . . . .	96
5.24	Confusion matrix for KNN . . . . .	96
5.25	Confusion matrix for NN . . . . .	96

**LIST OF TABLES**

5.1	Specification of MIMO Radar . . . . .	77
5.2	Target parameters for the considered experiment . . . . .	83
5.3	77GHz radar Performance Metrics for Bayes . . . . .	94
5.4	77GHz radar Performance Metrics for SVM . . . . .	94
5.5	77GHz radar Performance Metrics for KNN . . . . .	94
5.6	77GHz radar Performance Metrics for NN . . . . .	94

““

# Chapter 1

## Introduction

### 1.1 Background and Motivation

Radar (Radio Detection and Ranging) is a remote sensing technology that utilizes electromagnetic waves to detect, locate, and classify objects in various environments [1]. Originally developed for military applications, radar technology has evolved significantly and is now widely used in automotive safety, surveillance, weather forecasting, environmental monitoring, and biomedical applications [2]. The fundamental working principle of radar involves transmitting radio waves, receiving reflected signals from targets, and processing the received signals to extract meaningful information such as range, velocity, and object classification [3]. Radar systems are broadly classified into different types based on their operating principles. Pulse Radar, transmits short pulses and measures the time delay of returned signals to determine target distance. Continuous Wave (CW) Radar, continuously transmits a signal and detects Doppler shifts to measure velocity. Frequency Modulated Continuous Wave (FMCW) Radar, uses frequency variation over time to extract both range and velocity, making it ideal for high-resolution applications. Among the various radar types, FMCW radar has gained significant attention for its compact design, real-time processing, and robustness in diverse environmental conditions. FMCW radar enables precise range, velocity, and Doppler estimation, making it a crucial technology for advanced applications [4, 5, 6, 7, 8].

## 1.2 Role of FMCW Radar in Modern Applications

1. **Automotive and Transportation:** FMCW radar is widely used in advanced driver assistance systems (ADAS) for object detection and speed estimation. It helps in maintaining safe distances between vehicles and detecting obstacles in low visibility conditions such as fog or rain. Key applications include adaptive cruise control, collision avoidance, and blind-spot detection, enhancing vehicular safety and automation.
2. **Aerospace and Defense:** In military applications, FMCW radar enables real time tracking of aircraft, drones, and missiles. Its ability to operate in all weather conditions makes it invaluable for reconnaissance and threat detection. Key applications include Target tracking, missile guidance, and surveillance.
3. **Environmental Monitoring:** While pulse and Doppler radars are traditionally used in weather prediction and storm tracking, FMCW radar is primarily employed in ground-based remote sensing applications. It is particularly useful for measuring ice thickness, monitoring glaciers, and detecting changes in sea levels, playing a crucial role in climate change studies. Key applications include snow and ice measurement, glacier monitoring, and sea level monitoring.
4. **Biomedical and Healthcare:** Non contact physiological monitoring using FMCW radar is gaining traction in medical applications. It allows real-time tracking of vital signs, making it suitable for home based patient care and intensive care units. Key applications include Heart rate and breathing rate monitoring, dehydration assessment, and sleep monitoring.
5. **Industrial and Security Surveillance:** FMCW radar is widely deployed in perimeter security systems to detect unauthorized movement in restricted areas. In industrial automation, it is used to monitor machinery, ensure

worker safety, and enable smart factory automation by detecting objects in hazardous zones. Key applications include Perimeter security, intrusion detection, and machine monitoring.

- 6. Unmanned Aerial Vehicles (UAVs) and Robotics:** FMCW radar is integrated into autonomous drones, ground robots, and UAVs to assist in terrain mapping, object detection, and navigation in complex environments. It allows for safe maneuvering in low-light and visually degraded conditions. Key applications include obstacle avoidance, terrain mapping, and autonomous navigation.

FMCW radar's adaptability across multiple domains underscores its significance in modern technology, where precision sensing, environmental robustness, and real-time processing are essential. As traditional imaging and sensing methods often struggle with environmental constraints such as darkness, fog, or rain, radar technology has become increasingly vital in modern applications. This dissertation explores two major applications of FMCW radar: forward-looking radar imaging for automotive systems and physiological monitoring in biomedical contexts, demonstrating its versatility and reliability in diverse real world scenarios.

In subsequent chapters, each application area will be explored in depth, detailing the methods, data acquisition strategies, and experimental evaluations used to improve FMCW radar performance for these domains.

### **1.3 Research Objectives**

The growing demand for high resolution radar imaging and non-contact biomedical monitoring has driven significant advancements in MIMO radar and deep learning-based signal processing. Traditional radar solutions in automotive and biomedical applications often face challenges related to resolution, accuracy, and real-time feasibility. To address these limitations, innovative approaches that enhance radar performance and reliability are essential.

This dissertation focuses on two critical domains where radar technology plays a pivotal role: automotive and biomedical applications.

### 1.3.1 Automotive Applications

The rapid advancement of autonomous driving and advanced driver-assistance systems (ADAS) has increased the need for high-resolution forward-looking radar imaging to improve object detection, tracking, and navigation. However, conventional radar systems are constrained by limited angular resolution, which affects scene reconstruction and target discrimination in complex urban environments. To overcome this, MIMO radar combined with Forward-Looking Synthetic Aperture Radar (FL-SAR) techniques has been explored to enhance azimuthal resolution. Despite their potential, existing FL-SAR imaging approaches suffer from hardware limitations, computational inefficiencies, and low-resolution outputs.

This dissertation proposes two deep learning-based approaches to address these challenges:

- **Unsupervised Deep Basis Pursuit for Forward-Looking MIMO-SAR Imaging:** A novel deep learning framework designed to improve the resolution and clarity of forward-looking MIMO-SAR images while maintaining computational efficiency.
- **Convolutional Decoder for Forward-Looking MIMO-SAR Imaging:** A neural network-based reconstruction method that generates high-fidelity radar images from sparse or under-sampled data, enabling real-time applications in autonomous vehicles.

### 1.3.2 Biomedical Applications

Radar-based physiological monitoring has gained increasing attention for contactless health assessment, particularly in the monitoring of heart rate, respiration rate, and hydration status. Traditional biomedical sensors require physical contact, which can be intrusive, uncomfortable, and impractical for continuous

long-term monitoring. FMCW radar, with its ability to detect micro-movements, offers a non-invasive alternative for physiological signal extraction.

This dissertation introduces two radar-based biomedical monitoring techniques:

- **Joint Estimation of Heart and Respiration Rate:** A novel signal processing algorithm designed to simultaneously estimate heart and respiratory activity, addressing challenges posed by high-amplitude Doppler variations.
- **Dehydration Status Monitoring:** A machine learning-based approach leveraging Wavelet Scattering Transform (WST) to detect hydration status from radar-reflected signals, enabling remote health monitoring applications.

## 1.4 Organization of the Thesis

This dissertation is structured to provide a comprehensive understanding of FMCW radar applications in automotive and biomedical domains. The thesis is organized as follows: Chapter 2 lays the theoretical foundation, covering the principles of FMCW radar, and signal processing techniques. Chapter 3 delves into the automotive applications of radar, specifically FL-MIMO SAR imaging, while introducing deep basis pursuit and convolutional decoder methods for resolution enhancement. Chapter 4 shifts focus to biomedical applications, investigating contactless monitoring of heart rate and breathing rate estimation and dehydration status monitoring using FMCW radar and machine learning techniques. Chapter 5 presents a comparative analysis of simulated and experimental results, evaluating the performance of deep learning-based radar processing methods. Finally, Chapter 6 concludes the dissertation by summarizing key contributions, discussing challenges, and outlining future research directions. This structure ensures a logical progression from theoretical concepts to experimental validation, providing insights into FMCW radar advancements in automotive and biomedical applications.

## Chapter 2

### Fundamentals of FMCW Radar

#### 2.1 Principles of FMCW Radar

FMCW radar is a widely used radar technique that continuously transmits a frequency modulated signal rather than short pulses. This allows for precise range and velocity estimation, making it highly suitable for automotive perception, biomedical monitoring, military application and environmental sensing.

The fundamental principle of FMCW radar is based on transmitting a continuous wave signal that is linearly frequency modulated over time. The received echo signal is compared with the transmitted signal to extract a beat frequency, which is directly proportional to the range of the target. The key advantages of FMCW radar include:

- High range resolution due to its wideband frequency operation.
- Continuous operation without blind spots, unlike pulsed radar.
- Easy integration and low computation complexity.
- Capability to use a lower transmitted power to achieve the same detective range in comparison with classic pulse radar due to its average-to-peak power ration.
- Robustness to environmental conditions, making it ideal for autonomous driving and biomedical sensing.

Mathematically, the transmitted signal of an FMCW radar is represented as

$$s_{Tx}(t) = \exp(j2\pi f_c t + j\pi k t^2) \quad (2.1)$$

where  $f_c$  is the carrier frequency, chirp rate ( $k$ ) is defined as the ratio of transmitted bandwidth  $B$  and pulse repetition interval (PRI)  $T$ , and  $t$  is fast time index within the PRI, ( $0 < t < T$ ). The transmitted signal reflects from the target and is picked up by the receive antenna. The received signal can be written as

$$s_{Rx}(t) = s^{Tx}(t - \tau) = \tilde{\alpha} \exp(j2\pi f_c(t - \tau) + j\pi k(t - \tau)^2) \quad (2.2)$$

where  $\tilde{\alpha}$  is the attenuation factor,  $\tau = \frac{2R}{c}$  is the round trip delay,  $R$  is the distance at time  $t$  and  $c$  is speed of light. The received signal in (2.2) is demodulated by multiplying it with the transmitted chirp signal and passes through the low pass filter. Mathematically, the demodulated received signal in complex form can be written as

$$x(t) = s_{Rx}^*(t) * s_{tx}(t) = \tilde{\alpha} e^{j2\pi f_c \tau} e^{j2\pi(\frac{BR}{2T})t} \quad (2.3)$$

Substituting  $\tau$  in (2.3), the demodulated received signal can be written as

$$x(t) = \tilde{\alpha} e^{j\frac{4\pi f_c R}{c}} e^{j2\pi(\frac{BR}{cT})t}, \quad 0 \leq t \leq T \quad (2.4)$$

where the first term,  $e^{j\frac{4\pi f_c R}{c}}$ , is a constant factor, while the second term,  $e^{j2\pi(\frac{BR}{cT})t}$ , is a complex sinusoidal signal of frequency  $f_b = \frac{BR}{cT}$ , known as beat frequency. This allows FMCW radar to determine the distance of multiple targets simultaneously with high precision.

## 2.2 Range, Doppler, and Angle Estimation in FMCW Radar

FMCW radar simultaneously estimates three fundamental parameters of a target: Range (distance from the radar), Doppler velocity (speed of the target), and Angle of arrival (direction of the target).

Lets consider a scenario where target exhibits slow movement i.e., doppler

shift. Consider chirp signal of duration  $T$  is transmitted  $N_c$  times in a frame and  $n_R$  receiving antennas. Each chirp is repeated after a time interval called pulse-repetition-interval denoted as  $T_{\text{PRI}}(\geq T)$ . It is important to acknowledge that the beat frequency comprises both the Doppler and range components, posing a challenge for individual component estimation. For example, consider a FMCW radar that functions at a carrier frequency of 24 GHz and a bandwidth of 250 MHz, while employing a pulse duration of  $300\mu\text{s}$ . If there is a slow-moving target at a distance of 3m and a velocity of 1 m/sec, the resulting Doppler frequency will be 0.16 kHz, while the range component of the beat frequency will be 8.33 kHz. Consequently, we can ignore the contribution of the Doppler frequency to the beat frequency, and approximate it as  $f_b \approx \frac{BR}{cT}$ .

To estimate the Doppler shift of the target, the range of the target at the onset of the  $i$ th chirp can be expressed as

$$R^i = R_0 + iv_m T_{\text{PRI}}; \quad i = 0, 1, \dots, N_c - 1. \quad (2.5)$$

Substituting (2.5) in (2.4), the demodulated received signal after chirp  $i$  can be written as

$$\begin{aligned} x(t, i) &= \tilde{\alpha} e^{j \frac{4\pi f_c (R_0 + iv_m T_{\text{PRI}})}{c}} e^{j2\pi f_b t}, \\ &= \tilde{\alpha} e^{j \frac{4\pi R_0}{\lambda}} e^{j2\pi f_d i T_{\text{PRI}}} e^{j2\pi f_b t}. \end{aligned} \quad (2.6)$$

The utilization of (2.5) in (2.6) introduces a Doppler shift term,  $e^{j2\pi f_d i T_{\text{PRI}}}$ , in the received signal. The phase of this term changes with respect to the chirp index  $i$ . Unlike (2.4), the Doppler frequency is not coupled with any other frequency component and can be estimated by analyzing multiple chirps.

We consider  $n_R$  receiving antennas to estimate the target's angular location. The distance between any two adjacent receive antennas is  $\frac{\lambda}{2}$ . The demodulated

received signal after  $i$ th chirp at the  $m$ th antenna can be written as

$$x_m(t, i) = \alpha e^{j\pi \sin(\theta_0)(m-1)} e^{j2\pi f_d i T_{\text{PRI}}} e^{j2\pi f_b t}, \quad (2.7)$$

where  $\alpha = \tilde{\alpha} e^{j\frac{4\pi R_0}{\lambda}}$ ,  $\theta_0$  denotes the target direction. In (2.7), we have an additional spatial frequency term given by  $e^{j\pi \sin(\theta_0)(m-1)}$ , whose phase changes with respect to antenna number  $m$ . If after the transmission of  $i$ th chirp, the demodulated continuous signal is sampled at frequency  $F_s$ , the demodulated signal's  $n$ th sample can be written as

$$x_m(n, i) = \alpha e^{j\pi \sin(\theta_0)(m-1)} e^{j2\pi f_d i T_{\text{PRI}}} e^{j2\pi f_b n}. \quad (2.8)$$

Since the sampling time  $T_s = \frac{1}{F_s}$  is much lower than  $T_{\text{PRI}}$ , the samples indexed by  $n$  are called fast time samples, and the samples indexed by  $i$  are called slow time samples. We collect  $N_s = \frac{T}{T_s}$  samples after the transmission of a chirp pulse. It can be observed in (2.8) that there are three complex frequency terms  $e^{j\pi \sin(\theta_0)m}$ ,  $e^{j2\pi f_d i T_{\text{PRI}}}$ , and  $e^{j2\pi f_b n}$ . The frequencies of these terms can be estimated by applying FFT in the corresponding dimension.

### 2.2.1 Range Estimation

As discussed earlier, the beat frequency extracted from the received signal determines the range. Modern FMCW radar systems employ Fast Fourier Transform (FFT) processing to extract multiple beat frequencies, corresponding to different targets at different ranges. The  $N_r$  range bin FFT of the fast-time samples corresponding to demodulated received signal (2.4) can be written as

$$X_m(k, i) = \sum_{n=0}^{N_s-1} \alpha e^{j2\pi f_d i T_{\text{PRI}}} e^{j\pi \sin(\theta_0)(m-1)} e^{j2\pi f_b n} e^{-j\frac{2\pi kn}{N_r}}, \quad (2.9)$$

where  $k = 0, 1, \dots, N_r - 1$ . In (2.9), the phase of the first term depends on the index  $i$ , the phase of the second term on index  $m$ , and the third term on index

$n$ . It can be observed in the above equation, applying FFT does not affect terms depending on indices  $i$  and  $m$ . Therefore, (2.9) can be written as

$$X_m(k, i) = \alpha e^{j2\pi f_d i T_{\text{PRI}}} P(k) e^{j\pi \sin(\theta_0)(m-1)}, \quad (2.10)$$

where  $P(k) = \sum_{n=0}^{N_s-1} e^{j2\pi f_b n} e^{-j\frac{2\pi k n}{N_r}}$ . In (2.9), whenever  $\frac{k}{N_r} \approx \frac{BR_0}{cT}$  for  $k = 0, 1, \dots, N_r - 1$ ,  $P(k)$  will yield a peak to represent the presence of a target at index  $k$  and corresponding range can be easily found. For example, if  $P(k = \kappa)$  yields a peak value, the range of the corresponding target can be found as

$$R_0 = \frac{cT\kappa}{N_r B}. \quad (2.11)$$

The range of targets can be determined using the FFT on fast-time samples, commonly known as range FFT. It is worth noting that the FFT samples corresponding to any antenna and chirp can be selected for this purpose. To achieve higher range resolution, a wider transmit signal bandwidth is essential.

### 2.2.2 Doppler Estimation

The Doppler effect causes a frequency shift in the received signal due to the motion of the target. For an FMCW radar, Doppler estimation is achieved by transmitting multiple chirps and analyzing the phase difference between consecutive chirps. The Doppler shift is given by  $f_d = \frac{2f_c v}{c}$ . From (2.7),  $e^{j2\pi f_d i T_{\text{PRI}}}$ , is a complex sinusoidal signal of frequency  $f_d$ . The doppler frequency can be efficiently estimated by applying the FFT to the received signal along slow-time index [9, 10, 11]. However, these methods suffer from suboptimal resolution and exhibit high side-lobe levels that can obscure weak targets. To overcome these limitations, super-resolution techniques, such as MUSIC and Yule-Walker autoregressive (Yule-AR), have been employed to achieve improved Doppler frequency resolution [12, 13, 14, 15].

### 2.2.3 Angle Estimation

FMCW radar can also estimate the angle of arrival (AoA) of a target using Multiple-Input Multiple-Output (MIMO) configurations. By employing multiple receiving antennas, radar can form an aperture that enhances angular resolution. From (2.7),  $e^{j\pi \sin(\theta_0)(m-1)}$ , is a complex sinusoidal signal consisting of information about AoA. FFT along  $m$  index estimates AoA. However, these methods suffer from suboptimal resolution. Practical limitations arise regarding physical size when incorporating more antennas. Therefore, AoA is accurately estimated using techniques such as amplitude and phase estimation (APES), Capon, Multiple Signal Classification (MUSIC), and Estimation of Signal Parameters via Rotational Invariance Techniques (ESPRIT) have been explored [12, 13, 14, 16, 17, 18, 19, 20].

## Chapter 3

### FMCW Radar for Automotive Applications

#### 3.1 Introduction

Over the past few years, automotive radar has been getting a lot of attention in the context of self-driving cars and advanced driver assistance systems [21]. Optical sensors (e.g., lidar and camera) are mostly used for target scene imaging in most applications. However, in severe weather conditions, (e.g., fog, rain, etc.), imaging capability of the optical sensors is significantly reduced. The penetration capability of radar (operating at high frequencies), even in severe weather conditions, can provide substantial scene sensing. Therefore, radar is a decent option to choose for imaging along with subsequent tasks such as detection, classification, height estimation, etc. Autonomous driving application requires a few kilometers of range, thus, scene imaging is not problematic with radar [21]. One major challenge for automotive-radar imaging is range resolution and angular resolution. Range resolution primarily depends on transmit signal bandwidth and can be improved by increasing the bandwidth. Angular resolution depends on the physical aperture size of the radar antenna. In general physical aperture size depends on physical constraints and cannot be changed arbitrarily. We can mitigate this problem with two approaches. The first approach consists of using synthetic aperture radar and the second approach consists of using MIMO processing. In synthetic aperture radar, the radar illuminates a target scene at multiple locations, and reflections are combined coherently to induce a long synthetic aperture [22], [23], [24]. In general, a side looking SAR (SL-SAR) offers high gains of the synthetic aperture because the look angle (LA) is normal to the axis of radar

platform motion. Mostly, automotive-radar functionality is similar to a forward looking SAR i.e., the look angle is in the direction of the axis of radar platform motion. This reduces the effective aperture. Thus, it is difficult to achieve high angular resolution. Further, the high spatial resolution capabilities of SAR sensors are insufficient to reach the demanding goals with a limited number of antennas, especially in the forward looking direction. A significant amount of research has been carried out to improve the angular resolution of FL-SAR with single antenna [24, 25, 26, 27]. However, these methods encounter problems with mechanical (or electrical) scanning for slow speed, high cost, and high complexity to achieve enhanced spatial resolution. To overcome these problems and to improve the azimuth resolution (AR), researchers have turned to MIMO system. In MIMO processing, the radar either transmits the same signal over all transmit antennas in a time division multiplexing mode or transmits orthogonal signals over all transmit antennas. The target scene is extracted by combining all the return signals from all the receive antennas [28, 29, 30, 31]. MIMO radar received much attention in different applications due to its promising performance e.g., providing higher spatial resolution, degrees-of-freedom, etc. Considering limited spatial resolution and slow mechanical scanning in FL-SAR, combining MIMO and FL-SAR in automotive-radar imaging can provide promising results. In this work, we propose to replace the single antenna with MIMO antennas in FL-SAR. We call this process forward looking MIMO SAR (FL-MIMO-SAR). In this work, we demonstrate how FL-MIMO-SAR methodology improves the angular resolution.

Unlike optical images, the images acquired by MIMO-SAR (or SAR) mechanism suffer from many uncertainties due to clutter, and speckled noise. Therefore, reconstruction of high resolution images in MIMO-SAR (or SAR) is quite challenging.

Recent work in machine learning shows that deep neural networks can be used to solve a wide variety of inverse problems arising in computational radar imaging i.e., depicting the received radar echoes to extract meaningful information.

The high-resolution image reconstruction from small number of measurements is naturally an ill-posed inverse problem i.e., the number of unknowns can be much larger than the number of available measurements. By using some regularization techniques, it is possible to solve such ill-posed problems. In general, different regularized least-squares with various constraints are used to get the exact solution. The ill-posed inverse problem can be regularized with the help of some signal priors to extract the true solution [32, 33, 34, 35, 36, 37, 38]. However, it is impossible to come up with a suitable prior that makes the solution invincible. However, a possible approach is to use deep learning methods such as deep neural networks and convolutional neural networks [39]. In recent years, the deep learning based approaches have shown promising results for inverse problems related to the fields of image processing [40, 41, 42], natural language processing [43], and direction-of-arrival estimation [44], [45], etc. Unlike the analytical methods, deep neural networks use large datasets to find optimal representation and learn solution to the inverse problems. It has shown better performance compared with analytical de-convolution methods for various problems such as those in biomedical image processing, and compressive sensing domains. So, it is promising to employ deep neural networks to achieve the target information in radar processing [46, 47, 48]. This promising potential has been supported by recent research findings, indicating that CNN-based methods are capable of effectively handling radar signals [49], [50], [51].

In [52], a super-resolution convolutional neural network (SRCNN) is employed to enhance low-quality radar images and mitigate the effects of sidelobe/grating lobe artifacts. Similarly, authors of [53] proposes a deep learning approach for three-dimensional (3-D) reconstruction and imaging using millimeter-wave radar. This method generates two-dimensional (2-D) depth maps from the original data and subsequently reconstructs a 3-D point cloud.

Unlike the real-valued optical images, pixels in the radar image typically have complex values i.e., radar imaging is related to the processing of complex-valued

signals. To accommodate this complexity, the first layer of the neural network is extended to two channels, representing the real and imaginary parts of the radar image. This allows the network to effectively enhance radar images. Despite the challenges associated with research into complex-valued neural networks (CVNN), significant progress has been made in the field of radar imaging in recent years [50], [54], [55], [56]. Notably, the author of [54], proposes a complex-valued fully convolutional neural network (CVFCNN) with a generalized form of complex parametric rectified linear unit (CPRReLU) activation function specifically designed for MMW 3-D imaging.

However, for radar image processing with deep learning, the major challenge is the availability of labeled data (or ground truth). Unlike computer vision, acquiring a huge set of labeled training data in a radar imaging setup is generally impractical. A standard training dataset for this work does not exist. However, for the considered case of FL-MIMO-SAR, a significant number of measurements of the target scene can be acquired due to the forward motion of the radar. Therefore, we use this setup in our lab to acquire measurements of two targets by moving a MIMO radar towards the target scene. We consider the stop-and-go principle while collecting the measurements to keep the model simple. In this work, due to the unavailability of labeled training data, we use unsupervised learning. In unsupervised learning, the underlying neural network weights are updated in an end-to-end fashion by minimizing the average loss function in the measurement domain.

## 3.2 Contributions

In this work, we consider FL-MIMO-SAR and propose deep learning and back projection techniques to enhance angular resolution of an automotive radar in order to form a two-dimensional (2D) radar image. We use FMCW MIMO radar working at 77 GHz frequency. MIMO radar scans the target scene and then moves forward to the next scanning position/step along the aperture. We verify

the proposed approach for FL-MIMO-SAR methodology via simulation as well as real-data experiments in suitable conditions. The important features of the paper are highlighted below.

- We propose an FL-MIMO-SAR methodology. We use automotive radar as our primary application. However, the FL-MIMO-SAR methodology can be extended to other forward looking scenarios.
- We present a mathematical analysis for the composite antenna pattern generated by FL-MIMO-SAR. We show how FL-MIMO-SAR methodology contributes to an improvement in the effective aperture that results in the AR enhancement.
- We present a computationally efficient deep basis pursuit method and convolutional decoder method to estimate noise free images. Due to unavailability of ground truth data, we present unsupervised learning in the measurement domain during training. After estimating the noise free images, we present modified back projection (MBP) algorithm to reconstruct the final target image.
- We present experimental results to verify the proposed methodology and algorithm using both simulations and real measurements. We compare the performance of our approach with state-of-the-art compressed sensing (CS) based BP algorithm.

### 3.3 MIMO SIGNAL MODEL

Consider time division multiple access (i.e., alternately transmitting the same signal from each transmit antenna) based MIMO system consisting of  $N_T$  transmit (Tx) elements and  $N_R$  receive (Rx) elements. Without loss of generality, let the transmitting and the receiving arrays are parallel and co-located so that they see targets at the same directions. Considering far-field targets, the transmitter

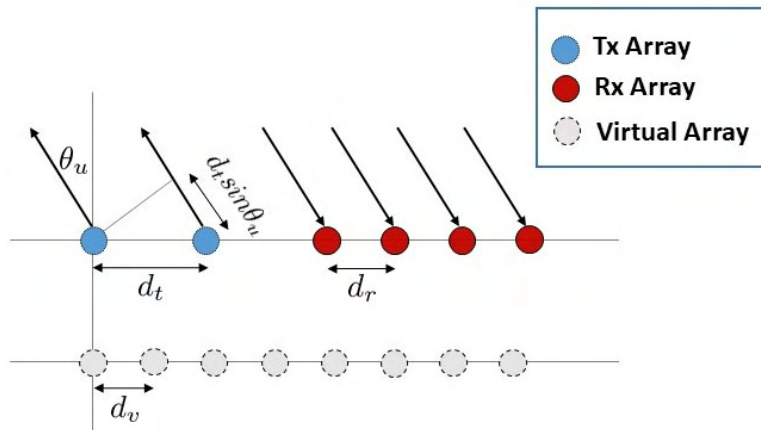


Figure 3.1: MIMO array schematic.

steering vector,  $\mathbf{a}^{Tx}(\theta)$ , and receiver steering vector,  $\mathbf{a}^{Rx}(\theta)$ , can be represented as

$$\mathbf{a}^{Tx}(\theta) = [1 \quad \exp(j2\pi \frac{d_t \sin \theta}{\lambda}) \quad \cdots \quad \exp(j2\pi \frac{(N_T-1)d_t \sin \theta}{\lambda})] \quad (3.1)$$

$$\mathbf{a}^{Rx}(\theta) = [1 \quad \exp(j2\pi \frac{d_r \sin \theta}{\lambda}) \quad \cdots \quad \exp(j2\pi \frac{(N_R-1)d_r \sin \theta}{\lambda})] \quad (3.2)$$

here  $d_t$  and  $d_r$  are the inter-antenna distances for transmitter and receiver arrays (shown in Fig. 3.1), respectively.  $d_v$  is inter-element distance of virtual antenna array. Further,  $\lambda$  is the wavelength and  $\theta$  denotes the target direction.

For a MIMO radar with  $N_T$  transmit elements and  $N_R$  receive elements, there will be  $N_T N_R$  distinct propagation channels from the Tx array to the Rx array. The transmitting source (Tx channel) of the received signals at the Rx array will generate  $N_v = N_T N_R$  virtual array. The virtual array  $\mathbf{a}(\theta)$  is defined as

$$\mathbf{a}(\theta) = \mathbf{a}^{Tx}(\theta) \otimes \mathbf{a}^{Rx}(\theta) \quad (3.3)$$

where  $\otimes$  denotes the Kronecker product.

FMCW chirp signal is transmitted from each MIMO Tx array elements. The chirp signal transmitted on transmit elements is expressed as:

$$s^{Tx}(t) = \exp(j2\pi f_c t + j\pi k t^2) \quad (3.4)$$

where  $f_c$  is the carrier frequency, chirp rate ( $k$ ) is defined as the ratio of transmitted bandwidth  $B$  and pulse repetition interval (PRI)  $T$ , and  $t$  is fast time index within the PRI, ( $0 < t < T$ ). For the ease of explanation, here we refer to virtual elements only (refer to Fig. 3.1). By assuming the far field condition, the return delay,  $\tau_j(u)$ , at  $j$ th virtual element for  $u$ th scatterer is defined as

$$\tau_j(u) = \frac{2R_u}{c} + \frac{v_j \sin \theta_u}{c} \quad (3.5)$$

where  $c$  is the speed of light and  $v_j$  is the  $j$ th virtual element. Further,  $\theta_u$  and  $R_u$  are respectively the angle w.r.t. broad side and the range of the  $u$ th scatterer.

The received signal at virtual array element  $v_j$  for  $U$  scatterers is expressed as

$$s_j^{Rx}(t) = \sum_{u=1}^U \alpha_u s^{Tx}(t - \tau_j(u)) \quad (3.6)$$

where  $\alpha_u$  is the reflectivity coefficient. The received signal (3.6) is deramped followed by low-pass filtering, The resulting signal is expressed as

$$\tilde{s}_j(t) = \sum_{u=1}^U \alpha_u \exp(j2\pi k \tau_j(u)t) \exp(j2\pi f_c \tau_j(u)) \exp(-j\pi k \tau_j^2(u)) \quad (3.7)$$

The  $\exp(j2\pi k \tau_j(u)t)$  term in equation (3.7) contains the targets range information which can be obtained by applying Fourier analysis along with the following linear transform.

$$f_j = k \tau_j(u) \approx \frac{2kR_u}{c} \quad (3.8)$$

Considering far-field conditions,  $\tau_j$  is dominated by  $\frac{2R_u}{c}$ . Therefore, it has a constant value along all the virtual channels. The phase term  $\{j2\pi f_c \tau_j(u)\}$  in equation (3.7) gives information about the arrival angle of reflected echos by beamforming with appropriate steering vectors.  $j\pi k \tau_j^2(u)$  is unwanted phase term (nearly constant for all the virtual channels), which can be removed via the

deskewing process [57]. The processed signal after deskewing can be written as

$$s_j(t) = \sum_{u=1}^U \alpha_u \exp(j2\pi k\tau_j(u)t + j2\pi f_c\tau_j(u)) \quad (3.9)$$

Let us define  $\psi = 2\pi f_c\tau_j(u)$  as the phase term. It contains a linear component  $2\pi f_c\tau_j$ , which reflects the arrival angle information of the echo. Specifically, using (3.5)

$$\psi = 2\pi f_c\tau_j = 2\pi f_c \frac{v_j \sin \theta}{c} + 2\pi f_c \frac{2R}{c} \quad (3.10)$$

$$= 2\pi \frac{v_j \sin \theta}{\lambda} + C \quad (3.11)$$

From (3.10), phase term is the sum of a phase component dependent on the element coordinates and a constant dependent on the scatterer range. Phase term  $\psi$  can be related to general steering vector of a MIMO virtual array. The steering vector can be used to extract the information along azimuth direction. The peaks in the corresponding range-azimuth target scene yield from FFT in fast time and beam forming in angular domain.

Applying Fourier transform to  $s_j(t)$  followed by linear transformation in the range profile, i.e.,

$$y_j(r) = \mathcal{F}_t\{s_j(t)\}|_{r=\frac{fc}{2k}}$$

where  $\mathcal{F}_t(\cdot)$  is Fourier transform operator w.r.t the time domain  $t$ ,  $f$  is frequency and  $r$  is range variable with linear transformation  $r = \frac{fc}{2k}$ .

The received signal for  $r$ th range bin across all virtual antennas can be written as

$$\mathbf{y} = \begin{bmatrix} y_1(r) & y_2(r) & \cdots & y_{N_v}(r) \end{bmatrix}^T \quad (3.12)$$

Neglecting the Doppler effect, in the presence of noise, the MIMO signal model for single aperture step can be written as

$$\mathbf{y} = \mathbf{A}\mathbf{x} + \mathbf{n} \quad (3.13)$$

where  $\mathbf{A} \in \mathbb{C}^{N_v \times n_\theta}$  is the steering matrix, defined as  $\mathbf{A} = \begin{bmatrix} \mathbf{a}(\theta_1) & \mathbf{a}(\theta_2) & \cdots & \mathbf{a}(\theta_{n_\theta}) \end{bmatrix}$ ,  $\mathbf{x} \in \mathbb{C}^{n_\theta \times 1}$  is the target scene reflectivity vector,  $\mathbf{n}$  is complex-valued Gaussian noise and,  $n_\theta$  and  $n_r$  are the number of angle bins and range bins, respectively. The FL-MIMO-SAR, collects the information from equidistant aperture positions

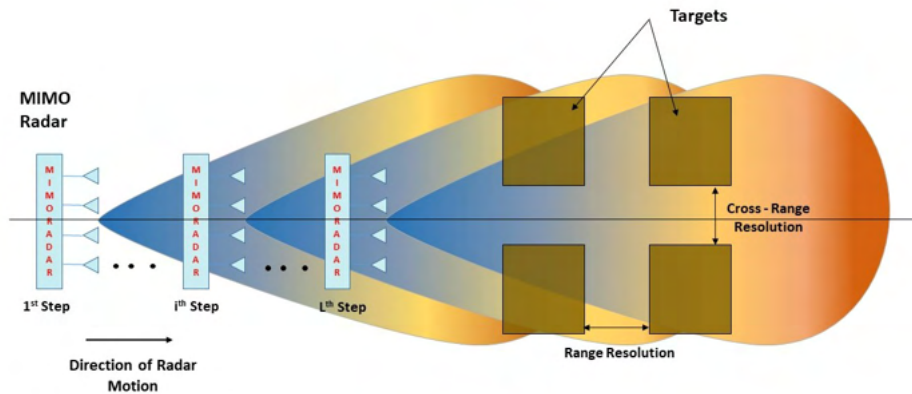


Figure 3.2: FL-MIMO-SAR schematic.

and processes the received information to reconstruct high resolution target scene. FL-MIMO-SAR schematic is shown in Fig. 3.2. From (3.13), signal model for  $i$ th aperture step/position of the radar is

$$\mathbf{y}^{(i)} = \mathbf{A}\mathbf{x}^{(i)} + \mathbf{n}^{(i)} \quad (3.14)$$

In this model, MIMO radar is moving along the x-axis. Thus, steering matrix ( $\mathbf{A}$ ) does not change for different aperture steps. However, that does not limit our proposed methodology. Since forward model operator  $\mathbf{A}$  is a wide matrix, i.e.,  $N_v \ll n_\theta$ , recovering  $\mathbf{x}^{(i)}$  from the observations  $\mathbf{y}^{(i)}$  is an an ill-posed problem. The general solution for such problems is given by the regularized least-squares optimization problem, i.e.,

$$\hat{\mathbf{x}} = \arg \min_{\mathbf{x}} \|\mathbf{A}\mathbf{x} - \mathbf{y}\|_2^2 + \lambda_0 \mathcal{R}(\mathbf{x}) \quad (3.15)$$

where  $\mathcal{R}(\mathbf{x})$  is a regularization term which is small for noise free data and high for noisy data, and  $\lambda_0$  is the strength of regularization.

### 3.4 FL-MIMO-SAR METHODOLOGY

Most of the times automotive radar functionality is similar to FL-SAR. Therefore, AR enhancement of an automotive radar with FL-SAR mechanism has very limited gains. The virtual array from MIMO helps in improving the angular resolution. Our main goal is to use MIMO and SAR concepts jointly to improve the angular resolution of an automotive radar. The FL-MIMO-SAR methodology impacts SAR capabilities with changing look angle. In this section, we show how FL-MIMO-SAR methodology can contribute to angular resolution enhancement.

#### 3.4.1 FL-MIMO-SAR Antenna Pattern

The synthetic aperture is similar to the phased antenna array except that all the antenna elements are not active simultaneously. The synthetic array output is computed by adding the individual contributions of each element. The synthetic aperture consists of overall synthetic array. In FL-SAR, the look angle of the radar is along radar platform motion, unlike SL-SAR, where look angle is normal to radar platform motion. Thus, in FL-SAR, the effective aperture decreases proportionally to the look angle. The single antenna element in FL-SAR is replaced with MIMO array to form FL-MIMO-SAR. Similar to FL-SAR, FL-MIMO-SAR look angle is not normal to the radar platform motion. Therefore, FL-MIMO-SAR effective aperture varies with respect to the LA. Fig. 3.3 shows the schematic of FL-MIMO-SAR, where  $\theta_L$  is the LA,  $N_l$  is the number of aperture steps, and  $d_l$  is the spacing between consecutive aperture steps. In order to explain FL-MIMO-SAR, let a continuous signal  $s(t) = \exp(j2\pi f_c t)$  be transmitted from  $n_v$ th MIMO virtual array element for,  $n_v = 1, 2, \dots, N_v$  from  $n_l$ th aperture element, for,  $n_l = 1, 2, \dots, N_l$  (where  $N_l$  is total number of aperture antenna elements). Considering a single target scatterer at distance  $r_u$  and angle

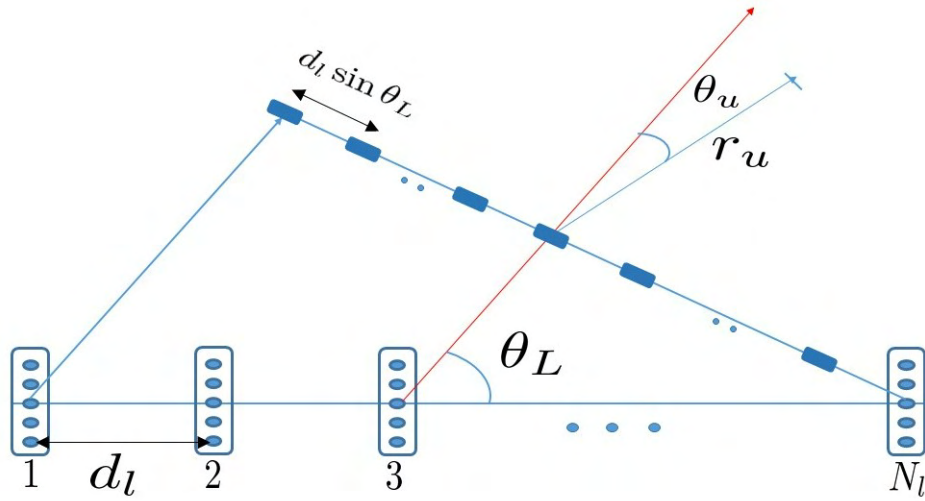


Figure 3.3: FL-MIMO-SAR :Synthetic antenna array for a LA.

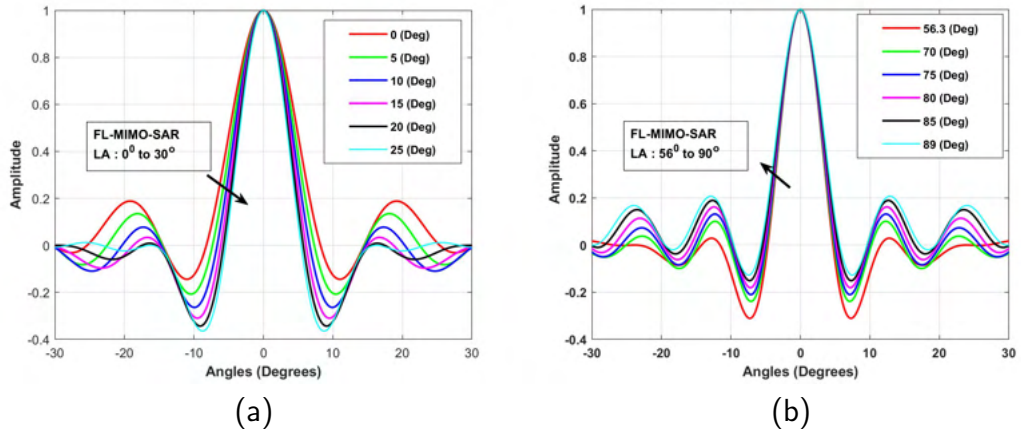


Figure 3.4: Composite antenna pattern (Normalized) for different Look Angles.

$\theta_u$ , the composite received signal of the synthetic antenna array is

$$R_{\theta_L}(t) = \sum_{n_l} \sum_{n_v} \exp\left\{j2\pi f_c \left(t - \frac{2r_u}{c} + 2(n_v - 1)d_v \cos \theta_L \sin \theta_u / c + 2(n_l - 1)d_l \sin \theta_L \sin \theta_u / c\right)\right\} \quad (3.16)$$

The received signal (3.16) depicts a 2-Dimensional (planar) antenna array, where one dimension is covered by the MIMO virtual array elements and the second dimension is covered by the synthetic array elements (refer to section 6.10 of

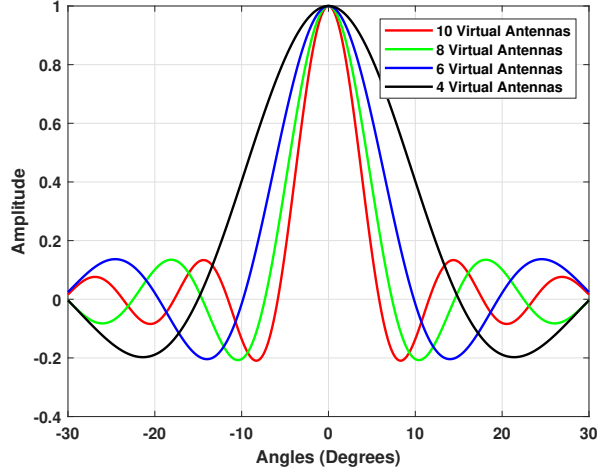


Figure 3.5: Composite antenna pattern (Normalized) for different number of MIMO virtual elements.

[58]). we can rewrite (3.16) as

$$R_{\theta_L}(t) = I_u \sum_{n_v} \exp\{j4\pi \frac{f_c}{c} (n_v - 1) d_v \cos \theta_L \sin \theta_u\} \sum_{n_l} \exp\{j4\pi \frac{f_c}{c} (n_l - 1) d_l \sin \theta_L \sin \theta_u\} \quad (3.17)$$

where  $I_u \triangleq \exp\{j2\pi f_c(t - \frac{2r_u}{c})\}$ . Using standard exponential sum formula, we can write (3.17) as

$$R_{\theta_L}(t) = I_u \frac{\sin(2N_v \pi d_v \cos \theta_L \sin \theta_u / \lambda)}{N_v \sin(2\pi d_v \cos \theta_L \sin \theta_u / \lambda)} \frac{\sin(2N_l \pi d_l \sin \theta_L \sin \theta_u / \lambda)}{N_l \sin(2\pi d_l \sin \theta_L \sin \theta_u / \lambda)} \quad (3.18)$$

By substituting  $K = 2\pi/\lambda$ , we can re-write (3.18) as

$$R_{\theta_L}(t) = I_u \frac{\sin(K N_v d_v \cos \theta_L \sin \theta_u)}{N_v \sin(K d_v \cos \theta_L \sin \theta_u)} \frac{\sin(K N_l d_l \sin \theta_L \sin \theta_u)}{N_l \sin(K d_l \sin \theta_L \sin \theta_u)} \quad (3.19)$$

By using the approximation  $\sin \theta \approx \theta$  (i.e., for small  $\theta$ ), we can obtain the following equation,

$$R_{\theta_L}(t) \approx I_u \text{sinc}(K N_v d_v \cos \theta_L \sin \theta_u) \text{sinc}(K N_l d_l \sin \theta_L \sin \theta_u) \quad (3.20)$$

By finding the angle at which the function (3.20) produces first null determines the angular resolution [58]. The first null is located at

$$K N_v d_v \cos \theta_L \sin \theta_u = \pm \pi \quad (3.21a)$$

$$K N_l d_l \sin \theta_L \sin \theta_u = \pm \pi \quad (3.21b)$$

solving (3.21a) and (3.21b) jointly reduces to

$$\sin \theta_u = \frac{\lambda}{2 (N_v d_v \cos \theta_L + N_l d_l \sin \theta_L)} \quad (3.22)$$

and AR can be calculated as

$$\Delta_{AR} = \frac{r_u \lambda}{2 (N_v d_v \cos \theta_L + N_l d_l \sin \theta_L)} \quad (3.23)$$

From (3.23), we can see that the effective aperture increases by increasing look angle till particular break look angle,  $\theta_b$ , and further increase in look angle decreases the effective aperture. By finding the look angle at which denominator in (3.23) (i.e.,  $N_v d_v \cos \theta_L + N_l d_l \sin \theta_L$ ) produces maximum value gives the best angular resolution (or maximum effective aperture). The maximum denominator value is located at

$$N_v d_v \cos \theta_L + N_l d_l \sin \theta_L = \sqrt{(N_v d_v)^2 + (N_l d_l)^2} \quad (3.24)$$

solving (3.24) determines the break look angle i.e.,

$$\theta_L = \theta_b = \pi/2 - \tan^{-1} \left( \frac{N_v d_v}{N_l d_l} \right) \quad (3.25)$$

Note,  $\theta_b$  depends on number of SAR elements ( $N_l$ ), number of MIMO virtual elements ( $N_v$ ), inter virtual antennas distance ( $d_v$ ) and inter SAR element distance ( $d_l$ ). From (3.23), we can see that angular resolution depends on MIMO virtual aperture ( $L_V = N_v d_v$ ), synthetic aperture ( $L_S = N_l d_l$ ) and look angle ( $\theta_L$ ).

To elaborate the effect of  $\theta_L$ , we consider a MIMO radar with two transmit antennas and four receive antennas. We consider a continuous signal  $\exp j2\pi f_c t$  with carrier frequency ( $f_c$ ) 77 GHz, bandwidth 2 GHz and other parameters  $N_l = 6$ ,  $d_l = \lambda/2$ ,  $N_v = 8$ ,  $d_v = \lambda/4$ . From Fig. 3.4a, we can see that increase in look angle reduces the beamwidth of the antenna pattern till break look angle  $\theta_b = 56.3^\circ$ , after that increase in look angle increases the beamwidth which is shown in Fig. 3.4b.

To elaborate the effect of MIMO virtual elements, we consider previous simulation setup with  $\theta_L = 5^\circ$  and varying number of virtual elements ( $N_v$ ) from 4 to 10. From Fig. 3.5, we can see that an increase in MIMO virtual elements reduces the beamwidth of antenna pattern i.e., increasing the angular resolution. In addition, we can see that the break look angle ( $\theta_b$ ) varies accordingly i.e.,  $\theta_b = 71.56^\circ, 63.43^\circ, 56.3^\circ, 50.12^\circ$  for  $N_v = 4, 6, 8, 10$ , respectively. To analyse the effect of SAR elements, we consider previous simulation setup and vary the number of SAR elements ( $N_l$ ) from 4 to 10. We can observe that the break look angle ( $\theta_b$ ) varies accordingly i.e.,  $\theta_b = 45^\circ, 56.31^\circ, 63.43^\circ, 68.19^\circ$  for  $N_l = 4, 6, 8, 10$  and beamwidth of antenna pattern decreases i.e., increasing the angular resolution. From the above observations, we can see the improvement in angular resolution till  $\theta_L = \theta_b$ , further increase in look angle decreases the angular resolution. These variations are based on SAR and MIMO.

### 3.5 Proposed Un-supervised Methodology

In this section, we propose a method that is used to implement FL-MIMO-SAR. We explore two deep learning methodologies for enhancing the azimuthal resolution of FL-MIMO SAR imaging: Deep Basis Pursuit (DBP) algorithm and Convolutional Decoder (ConvDecoder) algorithm. Both methods leverage data driven priors and iterative optimization to reconstruct high quality SAR images while addressing challenges related to noise, and limited measurements.

### 3.5.1 Deep Basis Pursuit

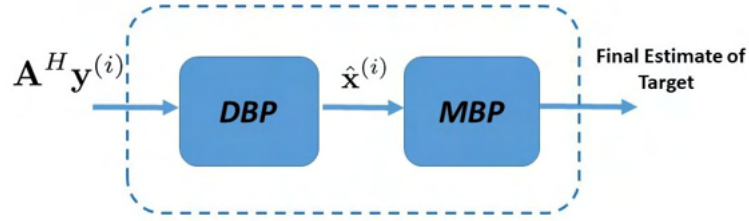


Figure 3.6: Proposed Structure for FL-MIMO-SAR Imaging

The structure of the proposed method is shown in Fig. 3.8. The proposed structure mainly consists of two blocks. First block represents the deep basis pursuit network, which helps in solving the ill-posed inverse problem. Second block represents the modified back projection step, which is used to generate the target image from per aperture reconstructed images [25]. In the following, we discuss the important aspects of the proposed methodology. Specifically, we will present the details about:

- Deep basis pursuit model,
- Training the network in unsupervised fashion, and
- Modified back projection algorithm.

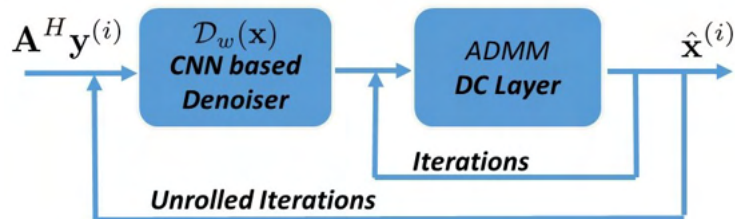


Figure 3.7: DBP Architecture for estimating  $\hat{\mathbf{x}}^{(i)}$ .

The first step of the proposed method is deep basis pursuit which is an unrolled network based on basis pursuit denoising. As presented earlier in (3.14), DBP is used to recover  $\mathbf{x}^{(i)}$  from the observations  $\mathbf{y}^{(i)}$ , which is an ill-posed problem [59]. The general solution for such problems can be obtained via regularized

least-squares (3.15). By considering model error due to noise, rearranging (3.15) to a constrained problem gives

$$\begin{aligned} & \arg \min_{\mathbf{x}} \mathcal{R}(\mathbf{x}) \\ & \text{subject to } \|\mathbf{y} - \mathbf{A}\mathbf{x}\|_2 \leq \epsilon \end{aligned} \quad (3.26)$$

where  $\epsilon$  is a function of noise power in the measurements. Combining the data consistency constraint of basis pursuit denoising (3.26) with the  $\ell_2$ -norm incorporating a CNN, the DBP formulation for the ill-posed problem is given by

$$\begin{aligned} & \arg \min_{\mathbf{x}} \frac{1}{2} \|\mathcal{N}_{\mathbf{w}}(\mathbf{x})\|_2^2 \\ & \text{subject to } \|\mathbf{y} - \mathbf{A}\mathbf{x}\|_2 \leq \epsilon \end{aligned} \quad (3.27)$$

where  $\mathcal{N}_{\mathbf{w}}(\mathbf{x}) \equiv \mathbf{x} - \mathcal{D}_{\mathbf{w}}(\mathbf{x})$  represents the noise and aliasing in  $\mathbf{x}$  [60],[61].  $\mathcal{D}_{\mathbf{w}}$  is a CNN designed to predict the denoised version of  $\mathbf{x}$  and is parameterized by weights  $\mathbf{w}$ . By allowing expected data inconsistency due to noise, the cleanest representation of  $\mathbf{x}$  is learnt.  $\epsilon$  is a function of noise variance ( $\sigma^2$ ). It is assumed that the measurement noise statistics ( $\epsilon$ ) are known to self regularize the solution. To solve (3.27), the following alternating minimization is used in an iterative manner [61].

$$\mathbf{r}_n = \mathcal{D}_{\mathbf{w}}(\mathbf{x}_{n-1}), \quad (3.28a)$$

$$\mathbf{x}_n = \arg \min_{\mathbf{x}} \frac{1}{2} \|\mathbf{x} - \mathbf{r}_n\|_2^2 \text{ s.t. } \|\mathbf{y} - \mathbf{A}\mathbf{x}\|_2 \leq \epsilon \quad (3.28b)$$

where  $n$  is the iteration index. Subproblem (3.28a) is a forward pass through CNN which is discussed the following subsection. As this CNN outputs a denoised version of  $\mathbf{x}$ , we also name it the CNN-based denoiser. Subproblem (3.28b) is a convex optimization problem which can be solved by alternating direction method of multipliers (ADMM) [59, 62].

The process of DBP alternates between two blocks namely, CNN layers (3.28a)

and data consistency (DC) layers (3.28b) as shown in the block diagram of Fig. 3.7. In this way, the target reflectivity corresponding to the  $i$ th aperture is estimated. Alternatively, the iterative architecture of DBP can be realized as an unrolled network where the two blocks are repeated a number of times equal to the number of iterations. Thus, the overall architecture contains the same number of DC layers and CNN layers in the unrolled network. The copies of CNN share the same weights in unrolled iterations.

## Unsupervised Learning

In general, supervised learning methods estimate the inverse operator by mapping measurements  $\mathbf{y}$  to the corresponding ground truth data  $\mathbf{x}$ . In traditional supervised learning, we have the knowledge about input  $\{\mathbf{y}^{(i)}, \mathbf{A}^{(i)}, \epsilon\}_{i=1}^{N_l}$  and ground truth  $\{\mathbf{x}^{(i)}\}_{i=1}^{N_l}$ . Thus, network weights are updated in an end-to-end fashion as

$$\min_{\mathbf{w}} \frac{1}{N_l} \sum_{i=1}^{N_l} \mathcal{L}(\hat{\mathbf{x}}_{\mathbf{w}}^{(i)}, \mathbf{x}^{(i)}) \quad (3.29)$$

where  $\hat{\mathbf{x}}_{\mathbf{w}}$  is the network output,  $\mathcal{L}$  is the loss function and  $\mathbf{w}$  is a vector of network weights.

In our case, ground truth data is not available. Therefore, we resort to unsupervised learning to update the network weights. In unsupervised learning, the loss function  $\hat{\mathcal{L}}$  is computed in the measurement domain. Thus, the network weights are updated as

$$\min_{\mathbf{w}} \frac{1}{N_l} \sum_{i=1}^{N_l} \hat{\mathcal{L}}(\mathbf{A}\hat{\mathbf{x}}_{\mathbf{w}}^{(i)}, \mathbf{y}^{(i)}) \quad (3.30)$$

The noisy measurements  $\mathbf{y}$  contain information about the ground-truth image  $\mathbf{x}$ . Thus, in the absence of ground truth data the measurement loss can act as a good substitute for the true loss [63], [64]. Therefore, the CNN weights are shared and trained in an unsupervised fashion in the measurement domain in our proposed methodology.

The proposed architecture of the CNN-based denoiser is shown in Fig. 5.1.

We use two separate input channels for real and imaginary components as the data is complex in nature. As shown in Fig. 5.1, we adopt ResNet architecture consisting of three convolutional layers. Each convolutional layer (except the last layer) is followed by a batch normalization layer and a nonlinear activation layer using rectified linear unit (ReLU) as the activation function. The final layer is just a convolutional layer. The convolutional layers extract the information of the targets from the received signals. The batch normalization layer is employed to improve the performance and stability of the deep neural network. This set of layers is repeated in the final architecture of DBP where the number of repetitions equals the number of unrolled iterations we choose to select.

## Modified Back Projection

The MBP upsamples the outputs of DBP (i.e.,  $\hat{\mathbf{x}}^{(i)}$ ) and projects them back to the target location. Thus, estimates corresponding to the target location are combined coherently to reconstruct final estimate of the enhanced FL-MIMO-SAR image.

The DBP reconstructs image in the polar domain. Therefore, we obtain extra information from the angular domain besides range domain. Thus, we can do interpolation in both the domains, while applying MBP. The outputs of DBP (i.e.,  $\hat{\mathbf{x}}^{(i)}$ ), after upsampling (in both range and angular domain) denoted as  $[\uparrow_{k,k}(\hat{\mathbf{x}}^{(i)})]$ , where  $\uparrow_{k,k}(\cdot)$  represents an upsampling function that upsamples a matrix by an order  $k$  along its rows and columns.

The reconstructed image from MBP can be written as

$$\mathbf{x}_{mn}^{final} = \sum_i [\uparrow_{k,k}(\hat{\mathbf{x}}^{(i)})]_{C_{\theta_{mn}}, C_{r_{mn}}} \quad (3.31)$$

where  $C_{r_{mn}}$  is the column index corresponding to range  $r_{mn} = \sqrt{(x_m - i)^2 + y_n^2}$  and  $C_{\theta_{mn}}$  is the row index corresponding to angle  $\theta_{mn} = \arctan((x_m - i)/y_n)$  in  $\uparrow_{k,k}(\hat{\mathbf{x}}^{(i)})$ . Accumulation of backscattered energy over the apertures results in

enhanced AR and better radar image reconstruction. Combining DBP-based reconstruction output with SAR processing guarantees enhanced angular resolution and better final radar image.

### 3.5.2 Convolutional Decoder

In this work, we use convolutional decoder[65] (i.e., Un-trained neural network) for solving an ill-posed inverse problem followed by modified back projection to reconstruct the radar image [25]. Fig. 3.8 shows the basic structure of the proposed method, i.e, to recover images,  $\mathbf{x}^{(i)}$  from measurements,  $\mathbf{y}^{(i)}$ , an un-trained network i.e., convolutional decoder (ConvDecoder) is used in the context of image priors [65].

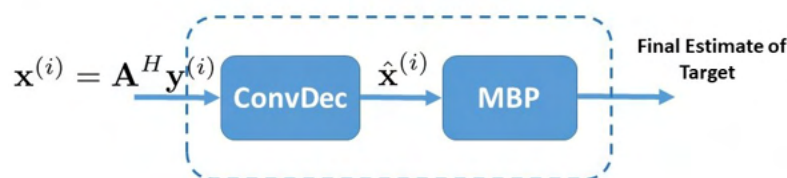


Figure 3.8: Proposed Structure.

The un-trained neural networks can be viewed as convolutional image priors which provide mapping from parameter space to the image space, i.e.,  $D : \mathbb{R}^p \rightarrow \mathbb{R}^{ch \times w \times h}$ , where  $ch$  denotes the number of channels of the output image, and  $w$  and  $h$  are width and height of the image. Note,  $ch$ ,  $w$  and  $h$  would change in the context of radar images (as mentioned in the next section). The ConvDecoder is an image model where the input of the network is fixed. The weights of the network are the parameters of the model, and the output of the model is an image. We can estimate an image from the measurements  $\mathbf{y}$  by minimizing the mean-squared loss function

$$\mathcal{L}(\mathbf{w}) = \sum_i \frac{1}{2} \|\mathbf{y}^{(i)} - \mathbf{A}D^{(i)}(\mathbf{w})\|^2 \quad (3.32)$$

where  $D(\mathbf{w})$  (i.e.,  $D^{(i)}(\mathbf{w}) = \hat{\mathbf{x}}^{(i)}$ ) is the reconstructed image for aperture steps.

We obtain a good estimate of  $\mathbf{w}$ , by minimizing the loss function ( $\mathcal{L}$ ). Here, we use one generator to produce multiple images at the same time. Therefore,  $D^{(i)}(\mathbf{w})$  is the reconstructed image associated with the  $i$ th aperture step measurement  $\mathbf{y}^{(i)}$ . The outputs of the ConvDecoder (i.e.,  $\hat{\mathbf{x}}^{(i)}$ ) fed to MBP , which upsamples the  $\hat{\mathbf{x}}^{(i)}$  and project them back to the target location. The final estimate of enhanced FL-MIMO-SAR image is obtained by combining the estimates corresponding to their target locations.

## Chapter 4

### FMCW Radar of Bio-Medical Applications

The COVID-19 pandemic and the growing aging population have significantly increased the demand for non-invasive and contactless sensing technologies in healthcare monitoring within hospitals and nursing homes [66, 67, 68]. These advanced sensing methods are crucial for continuous health monitoring, reducing the risk of infection transmission, and improving patient comfort and care. Non-contact sensing technologies are being leveraged for a variety of critical applications, including vital sign estimation, gesture recognition, road user classifications, emotion recognition, speech recognition and sleep monitoring, etc. To our knowledge, the primary non-contact sensing technologies are radio frequency-based sensing, vision-based sensing, and acoustic-based sensing [69]. Radio frequency signals for contactless sensing include WiFi, ultra-wideband (UWB), and millimeter-wave (mmWave) technologies. Vision-based technologies are based on visible light and infrared (IR), while acoustic methods typically involve the use of audio devices for signal acquisition or extraction. These non-contact sensing modalities offer unique advantages and have been integrated into various healthcare and non-healthcare applications, demonstrating their versatility and effectiveness.

This chapter presents radar-based physiological monitoring techniques, structured into two main sections. The first section introduces a signal model and a novel processing framework for jointly estimating Doppler frequencies related heart rate and breathing rate while mitigating motion artifacts. The second part discusses a non contact dehydration monitoring approach, detailing the signal modeling process and a machine learning driven classification method for hydra-

tion assessment.

## 4.1 Heart Rate and Breathing Rate Estimation

### 4.1.1 Introduction

Development of patient monitoring systems that leverage radar technology to enable non-invasive and probeless monitoring of vital signs. These systems offer a promising approach to address the challenges posed by traditional monitoring methods, as they can accurately measure vital signs and track patient location without the need for sensors or probes to be attached to the patient. Moreover, the non-contact nature of radar-based systems makes them an attractive option for patients who may experience discomfort when wearing sensors or probes for extended periods, suffer from skin allergies, or find it difficult to sleep with attached devices.

This work addresses the challenges involved in Doppler frequency estimation in FMCW radar when multiple targets are present at different locations, and each target introduces two distinct Doppler shifts with substantial difference in their signal amplitudes. Such situations commonly arise in radar-based vital sign monitoring applications. Due to the proximity of the heart and lungs within the same range bin [70, 71], combined with their substantial size difference, leads to potential signal masking where the reflected signal from the heart may be overshadowed by the dominant lung signal [72]. Consequently, extracting information related to heart rate becomes a challenging task. In this application, initially, targets present at different ranges and angular locations are localized [73]. Subsequently, Doppler frequencies corresponding to each target are estimated. The Doppler frequencies are directly proportional to the movement of the heart and chest and can be exploited to estimate heart and breathing rates.

A similar situation can also arise in detecting and classifying road users [74], where Doppler frequencies generated by a road user serve as valuable cues for its classification. For instance, when observing a pedestrian, Doppler frequencies

emerge from the motion of their torso, hands, and legs. Likewise, a cyclist's Dopplers result from the movement of the bicycle and the rotation of its wheels. Meanwhile, in the case of a car, Doppler frequencies originate from the vehicle's body movements and the rotation of its wheels. It is important to note that each road user introduces distinct Doppler frequencies with different signal amplitudes.

These applications involve a two-step process. The first step revolves around precise target localization, which necessitates improved range and angular resolution. Enhancing range resolution requires wide transmit signal bandwidth while augmenting angular resolution often entails additional antennas. However, practical limitations arise regarding physical size when incorporating more antennas. Consequently, extensive research has been conducted in recent years to achieve accurate estimation of the direction-of-arrival (DOA) of targets. Various algorithms such as amplitude and phase estimation (APES), Capon, MULTiple Signal Classification (MUSIC), and Estimation of Signal Parameters via Rotational Invariance Techniques (ESPRIT) have been explored [16, 17, 18, 19, 20, 12, 13, 14]. In this paper, we propose the utilization of the Capon method to enhance DOA estimation resolution.

The second step involves the accurate estimation of target Doppler frequencies. Conventional methods often rely on the utilization of FFT for the estimation of Doppler frequencies [9, 10, 11]. However, these methods suffer from suboptimal resolution and exhibit high side-lobe levels that can obscure weak targets. To overcome these limitations, super-resolution techniques, such as MUSIC and Yule-Walker autoregressive (Yule-AR), have been employed to achieve improved Doppler frequency resolution. Nevertheless, the performance of MUSIC and Yule-AR can deteriorate in the presence of noise, particularly under low signal-to-noise ratio (SNR) conditions [12, 13, 14, 15].

### 4.1.2 Contributions

This work proposes novel methods for the estimation of high-resolution targets' location and Doppler frequencies using FMCW radar. The proposed approach formulates the problem in a manner that enables the application of the Capon algorithm to estimate the angular locations of the targets. Furthermore, we introduce a Capon-like algorithm to estimate high-resolution Doppler frequencies. By employing these methods, we aim to enhance the accuracy and precision of target localization and Doppler frequency estimation.

The main contributions of our work are as follows:

- We have formulated a signal model for the purpose of localizing multiple targets, with each target contributing two Doppler shifts in the reflected signal. This model holds potential utility in mapping Doppler shifts resulting from the movement of the heart and chest, as well as in applications related to road user classification.
- By restructuring the received samples into a specific format, we are able to apply high angular and Doppler resolution algorithms such as APES and Capon. However, for the purpose of our study, we employ the Capon and Capon-like algorithms to estimate the target's angular location and Doppler frequencies respectively while leaving the utilization of APES for future research.
- Finally, we propose an innovative approach for target localization and the estimation of two Doppler frequencies introduced by each moving target. The proposed algorithm is designed to exhibit negligible sidelobe levels, high-frequency resolution, and resilience against individual target radar cross-sections and frequency differences. Notably, this approach yields a mirror solution, which offers its own unique set of benefits.

### 4.1.3 Signal Model

We leverage an FMCW radar system equipped with a single transmitting antenna and  $n_R$  receiving antennas [75, 76]. Both the transmit and receive antennas are positioned in close proximity, arranged in a uniform linear array configuration. The targets interact with the transmitted signals, causing reflections that are subsequently captured by the receiving antennas. The basic system model of the considered system is depicted in Figure 4.1. In an FMCW radar, a chirp signal of duration  $T$  is transmitted  $N_c$  times in a frame. Each chirp is repeated after a time interval called pulse-repetition-interval denoted as  $T_{\text{PRI}}(\geq T)$ . The total duration of  $N_c$  chirps is called coherent-processing-interval (CPI) i.e.,  $T_{\text{CPI}} = N_c T_{\text{PRI}}$ . The transmitted  $i$ th chirp signal in complex form can be expressed as

$$s(t) = e^{j2\pi(f_c + \frac{Bt}{2T})t}, \quad (4.1)$$

where  $iT_{\text{PRI}} \leq t \leq iT_{\text{PRI}} + T$  for  $i = 0, \dots, N_c - 1$ , while  $B$  and  $f_c$  are bandwidth and carrier frequency of the transmitted signal, respectively. The transmitted signal reflects from the target of interest and is picked up by the receive antenna. Considering  $L$  targets in the field-of-view of radar, the received signal can be written as

$$r(t) = \tilde{\alpha} e^{j2\pi((f_c + f_d) + \frac{Bt}{2T})(t - \tau)} + \bar{v}(t) \quad (4.2)$$

where  $\tilde{\alpha}$  is the attenuation factor,  $\tau = \frac{2R(t)}{c}$  is the round trip delay,  $R(t)$  is the distance at time  $t$ ,  $v$  is the speed, and  $f_d = \frac{2f_c v}{c}$  is the Doppler frequency corresponding to the target of interest. The term  $\bar{v}(t)$  includes the noise and interferences from other targets and it can be written as

$$\bar{v}(t) = \sum_{l=1}^{L-1} \tilde{\alpha}_l e^{j2\pi((f_c + f_{dl}) + \frac{Bt}{2T})(t - \tau_l)} + n(t), \quad (4.3)$$

where  $n(t) \sim \mathcal{N}(0, \sigma^2)$  is noise. The received signal in (4.2) is demodulated by multiplying it with the transmitted chirp signal and passes through the low pass

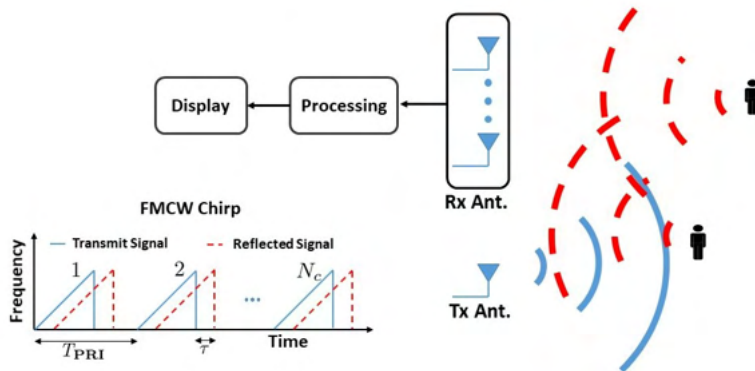


Figure 4.1: System model of the considered FMCW radar.

filter. Mathematically, the demodulated received signal in complex form can be written as

$$\begin{aligned}
 x(t) &= r^*(t)s(t), \\
 &= \tilde{\alpha} e^{-j2\pi((f_c+f_d)+\frac{Bt}{2T})(t-\tau)} e^{j2\pi(f_c+\frac{Bt}{2T})t} + v(t), \\
 &= \tilde{\alpha} e^{j2\pi f_c \tau} e^{j2\pi(-f_d+\frac{B\tau}{2T})t} + v(t),
 \end{aligned} \tag{4.4}$$

where  $v(t) = \bar{v}^*(t)e^{j2\pi(f_c+\frac{Bt}{2T})t}$ . Substituting  $\tau$  in (4.4), the demodulated received signal can be written as

$$x(t) = \tilde{\alpha} e^{j\frac{4\pi f_c R_0}{c}} e^{j2\pi(\frac{BR_0}{cT}-f_d)t} + v(t), \quad 0 \leq t \leq T \tag{4.5}$$

where the first term,  $e^{j\frac{4\pi f_c R_0}{c}}$ , is a constant factor, while the second term,  $e^{j2\pi(\frac{BR_0}{cT}-f_d)t}$ , is a complex sinusoidal signal of frequency  $f_b = \frac{BR_0}{cT} - f_d$ , known as beat frequency. The beat frequency can be efficiently estimated by applying the FFT to the received signal in (4.5). It is important to acknowledge that the beat frequency comprises both the Doppler and range components, posing a challenge for individual component estimation. However, in scenarios where targets exhibit slow movement, it can be mathematically demonstrated that  $f_d \ll \frac{BR_0}{cT}$ , which enables the estimation of the range component of the beat frequency. For example, consider a FMCW radar that functions at a carrier frequency of 24 GHz and a bandwidth of 250 MHz, while employing a pulse duration of  $300\mu s$ . If there is

a slow-moving target at a distance of 3m and a velocity of 1 m/sec, the resulting Doppler frequency will be 0.16 kHz, while the range component of the beat frequency will be 8.33 kHz. Consequently, we can ignore the contribution of the Doppler frequency to the beat frequency, and approximate it as  $f_b \approx \frac{BR_0}{cT}$ .

To estimate the Doppler shift of the target, the range of the target at the onset of the  $i$ th chirp can be expressed as

$$R_0^i = R_0 + iv_m T_{\text{PRI}}; \quad i = 0, 1, \dots, N_c - 1. \quad (4.6)$$

Substituting (4.6) in (4.5), the demodulated received signal after chirp  $i$  can be written as

$$\begin{aligned} x(t, i) &= \tilde{\alpha} e^{j \frac{4\pi f_c (R_0 + iv_m T_{\text{PRI}})}{c}} e^{j2\pi f_b t} + v(t, i), \\ &= \tilde{\alpha} e^{j \frac{4\pi R_0}{\lambda}} e^{j2\pi f_d i T_{\text{PRI}}} e^{j2\pi f_b t} + v(t, i). \end{aligned} \quad (4.7)$$

The utilization of (4.6) in (4.7) introduces a Doppler shift term,  $e^{j2\pi f_d i T_{\text{PRI}}}$ , in the received signal. The phase of this term changes with respect to the chirp index  $i$ . Unlike (4.5), the Doppler frequency is not coupled with any other frequency component and can be estimated by analyzing multiple chirps.

We consider  $n_R$  receiving antennas to estimate the target's angular location. The distance between any two adjacent receive antennas is  $\frac{\lambda}{2}$ . The demodulated received signal after  $i$ th chirp at the  $m$ th antenna can be written as

$$x_m(t, i) = \alpha e^{j\pi \sin(\theta_0)(m-1)} e^{j2\pi f_d i T_{\text{PRI}}} e^{j2\pi f_b t} + v_m(t, i), \quad (4.8)$$

where  $\alpha = \tilde{\alpha} e^{j \frac{4\pi R_0}{\lambda}}$ ,  $\theta_0$  denotes the target direction, and  $v_m(t, i)$  represents the contribution of noise and interference. In (4.8), we have an additional spatial frequency term given by  $e^{j\pi \sin(\theta_0)(m-1)}$ , whose phase changes with respect to antenna number  $m$ . If after the transmission of  $i$ th chirp, the demodulated continuous signal is sampled at frequency  $F_s$ , the demodulated signal's  $n$ th sample can be

written as

$$x_m(n, i) = \alpha e^{j\pi \sin(\theta_0)(m-1)} e^{j2\pi f_d i T_{\text{PRI}}} e^{j2\pi f_b n} + v_m(n, i). \quad (4.9)$$

Since the sampling time  $T_s = \frac{1}{F_s}$  is much lower than  $T_{\text{PRI}}$ , the samples indexed by  $n$  are called fast time samples, and the samples indexed by  $i$  are called slow time samples. We collect  $N_s = \frac{T}{T_s}$  samples after the transmission of a chirp pulse. It can be observed in (4.9) that there are three complex frequency terms  $e^{j\pi \sin(\theta_0)m}$ ,  $e^{j2\pi f_d i T_{\text{PRI}}}$ , and  $e^{j2\pi f_b n}$ . The frequencies of these terms can be estimated by applying FFT in the corresponding dimension.

In contrast to the above conventional signal model, our work considers a problem where a target from a unique location introduces two Doppler shifts in the reflected signal. For such application, the modified signal model can be written as

$$x_m(n, i) = e^{j\pi \sin(\theta_0)(m-1)} \left( \alpha_1 e^{j2\pi f_{d_1} i T_{\text{PRI}}} e^{j2\pi f_{b_1} n} + \alpha_2 e^{j2\pi f_{d_2} i T_{\text{PRI}}} e^{j2\pi f_{b_2} n} \right) + v_m(n, i), \quad (4.10)$$

where  $\alpha_1$  and  $\alpha_2$  are attenuation factors while  $f_{d_1}$  and  $f_{d_2}$  are Doppler shifts introduced by the single target. It should be noted that for most of the practical scenarios  $f_{d_p} \ll \frac{BR_0}{cT}$ , for  $p = 1, 2$ . Therefore, Doppler frequency contribution to the beat frequency can be ignored which allows us to write  $f_b = \frac{BR_0}{cT}$  and  $f_{b_1} \approx f_{b_2}$ . Using this assumption, the modified signal model in (4.10) can be written as

$$x_m(n, i) = \left( \alpha_1 e^{j2\pi f_{d_1} i T_{\text{PRI}}} + \alpha_2 e^{j2\pi f_{d_2} i T_{\text{PRI}}} \right) e^{j\pi \sin(\theta_0)(m-1)} e^{j2\pi f_b n} + v_m(n, i), \quad (4.11)$$

where  $f_b = f_{b_p}$ , for  $p = 1, 2$ . In contrast to (4.5), the signal model in (4.11) shows two Doppler frequency terms with different amplitudes. The lower am-

plitude Doppler frequency component can be masked if the difference between the amplitudes ( $\alpha_1$  and  $\alpha_2$ ) is high. Moreover, if the two frequencies are close to each other, it becomes challenging to resolve them using simple FFT-based algorithms. For such problems, high-resolution algorithms such as Capon and APES can be used [20]. In the following section, we will show that applying high-resolution algorithms for jointly estimating angular location and Doppler shifts is also challenging.

#### 4.1.4 Proposed Methodology

This section proposes a three-step method to estimate the target's location and Doppler frequencies. The first step estimates the targets' ranges, the second step estimates the targets' angular locations and the final step estimates the Doppler frequencies corresponding to each target. Fig. 4.2, describes the overall procedure in the block diagram.

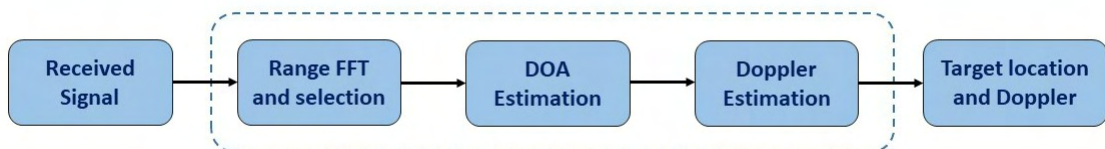


Figure 4.2: Proposed methodology.

#### Range Estimation and Selection:

The FFT can be applied to the demodulated received samples to estimate the ranges of different targets. The  $N_r$  range bin FFT of the fast-time samples corresponding to  $i$ th chirp signal at the  $m$ th antenna in (4.11) can be written as

$$X_m(k, i) = \sum_{n=0}^{N_s-1} \left( \alpha_1 e^{j2\pi f_{d_1} i T_{\text{PRI}}} + \alpha_2 e^{j2\pi f_{d_2} i T_{\text{PRI}}} \right) e^{j\pi \sin(\theta_0)(m-1)} e^{j2\pi f_b n} e^{-j\frac{2\pi kn}{N_r}} + V_m(k, i), \quad (4.12)$$

where  $k = 0, 1, \dots, N_r - 1$ . In (4.12), the phase of the first term depends on the index  $i$ , the phase of the second term on index  $m$ , and the third term on index  $n$ . It can be observed in the above equation, applying FFT does not affect terms depending on indices  $i$  and  $m$ . Therefore, (4.12) can be written as

$$X_m(k, i) = \left( \alpha_1 e^{j2\pi f_{d_1} i T_{\text{PRI}}} + \alpha_2 e^{j2\pi f_{d_2} i T_{\text{PRI}}} \right) P(k) e^{j\pi \sin(\theta_0)(m-1)} + V_m(k, i), \quad (4.13)$$

where  $P(k) = \sum_{n=0}^{N_s-1} e^{j2\pi f_b n} e^{-j\frac{2\pi k n}{N_r}}$ . In (4.12), whenever  $\frac{k}{N_r} \approx \frac{BR_0}{cT}$  for  $k = 0, 1, \dots, N_r - 1$ ,  $P(k)$  will yield a peak to represent the presence of a target at index  $k$  and corresponding range can be easily found. For example, if  $P(k = \kappa)$  yields a peak value, the range of the corresponding target can be found as

$$R_0 = \frac{cT\kappa}{N_r B}. \quad (4.14)$$

The range of targets can be determined using the FFT on fast-time samples, commonly known as range FFT. It is worth noting that the FFT samples corresponding to any antenna and chirp can be selected for this purpose. In our proposed algorithm, we utilize the first antenna to obtain  $N_s$  samples for the first chirp. Subsequently, we apply FFT to these samples and identify the peak values that indicate the ranges of multiple targets, thereby enabling us to estimate their respective ranges. Next, we determine the corresponding index for each target and collect samples with the same index from all antennas to estimate their angular location.

## High-Resolution DOA Estimation:

To estimate the angular location of the target that corresponds to  $k = \kappa$ , we can represent the sample from the corresponding antenna  $m$  as follows

$$Y_m(\kappa, i) = \left( \alpha_1 e^{j2\pi f_{d_1} i T_{\text{PRI}}} + \alpha_2 e^{j2\pi f_{d_2} i T_{\text{PRI}}} \right) P(\kappa) e^{j\pi \sin(\theta_0)(m-1)} + V_m(\kappa, i),$$

$$m = 1, 2, \dots, n_R$$

For a fixed value of  $i = \mathcal{I}$ , if we collect samples from all antennas at index  $k = \kappa$ , the sampled signal vector can be written as

$$\mathbf{y}(\kappa) = \mathbf{a}(\theta_0) \left( \alpha_1 e^{j2\pi f_{d_1} i T_{\text{PRI}}} + \alpha_2 e^{j2\pi f_{d_2} i T_{\text{PRI}}} \right) P(\kappa) + \mathbf{v}(\kappa, i), \quad (4.15)$$

where  $\mathbf{y}(\kappa) = \left[ Y_1(\kappa, i) \ Y_2(\kappa, i) \ \dots \ Y_{n_R}(\kappa, i) \right]^T$  and  $\mathbf{a}(\theta) = \left[ 1 \ e^{j\pi \sin(\theta)} \ \dots \ e^{j\pi(n_R-1)\sin(\theta)} \right]^T$ . Applying the FFT to (4.15) enables estimation of the target's angular location. However, the angular resolution is dependent on the number of receive antennas used. To enhance the angular resolution, one can cascade the vectors in (4.15) for  $i = 0$  to  $i = N_c - 1$ , creating a matrix  $\mathbf{Y}(\kappa)$  of dimension  $n_R \times N_c$ . This matrix can be represented as

$$\mathbf{Y}(\kappa) = \mathbf{a}(\theta_0) \left( \alpha_1 \mathbf{a}^T(f_{d_1}) + \alpha_2 \mathbf{a}^T(f_{d_2}) \right) P(\kappa) + \mathbf{V}(\kappa) \quad (4.16)$$

where  $\mathbf{a}(f_{d_p}) = \left[ 1 \ e^{j2\pi f_{d_p}} \ \dots \ e^{j2\pi(N_c-1)f_{d_p}} \right]^T$  for  $p = 1, 2$ . Similarly, incorporating matrices for all range bins a data cube matrix can be formed as shown in Fig. 4.3. Setting  $\beta_1 = \alpha_1 P(\kappa)$  and  $\beta_2 = \alpha_2 P(\kappa)$ , (4.16) can be re-written in more compact form as

$$\mathbf{Y}(\kappa) = \mathbf{a}(\theta_0) \left( \beta_1 \mathbf{a}^T(f_{d_1}) + \beta_2 \mathbf{a}^T(f_{d_2}) \right) + \mathbf{V}(\kappa). \quad (4.17)$$

Expressing the received samples in the format presented in (4.17) enables us to

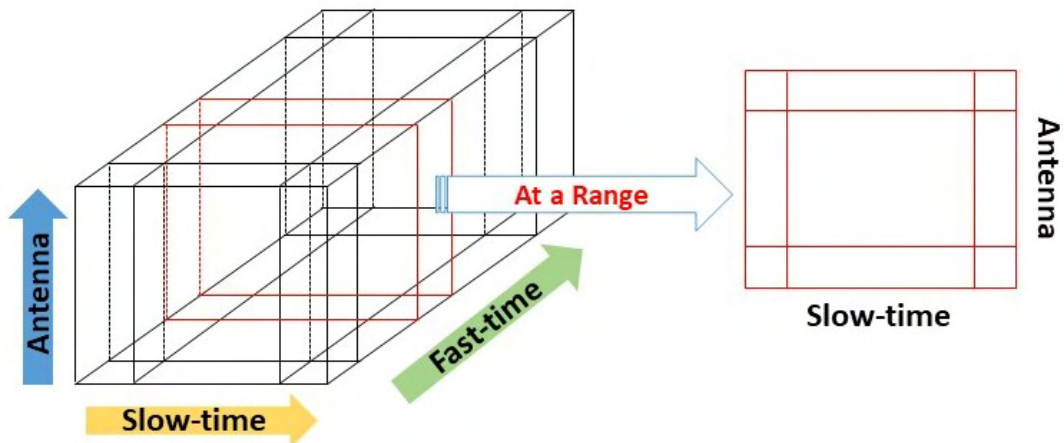


Figure 4.3: Datacube representation of FMCW Intermediate Frequency (IF) signal with array dimension  $n_R$ , and slow-time samples  $N_s$ .

formulate a weight vector similar to Capon's method, which effectively suppresses noise and interference while preserving the signal component. The weight vector, denoted as  $\mathbf{w}$ , can be obtained by solving the following optimization problem with constraints, as proposed in [20]

$$\min_{\mathbf{w}} \mathbf{w}^H \mathbf{E} \{ \mathbf{Y}(\kappa) \mathbf{Y}^H(\kappa) \} \mathbf{w} \quad \text{subject to} \quad \mathbf{w}^H \mathbf{a}(\theta) = 1.$$

The solution to this problem leads to the derivation of a weight vector that offers superior angular resolution and can be expressed as follows

$$\mathbf{w} = \frac{\mathbf{R}^{-1} \mathbf{a}(\theta)}{\mathbf{a}^H(\theta) \mathbf{R}^{-1} \mathbf{a}(\theta)}, \quad (4.18)$$

where  $\mathbf{R} = \mathbf{E} \{ \mathbf{Y}(\kappa) \mathbf{Y}^H(\kappa) \}$  and  $\theta$  is a sweep angle. Whenever  $\theta = \theta_0$  the spectrum of  $\mathbf{w}^H \mathbf{E} \{ \mathbf{Y}(\kappa) \mathbf{Y}^H(\kappa) \} \mathbf{w}$  yields a clear peak value that satisfies the constraint  $\mathbf{w}^H \mathbf{a}(\theta_0) = 1$ .

In the signal model, we have assumed that there is only one target at the given range. However, in practice, multiple targets with different angular locations can be present at the same range. We are interested only in moving targets, therefore stationary targets can be eliminated by taking the mean along each row and subtracting it from each column entry along that row.

To estimate the values of  $\beta_p$  for  $p = 1, 2$ , the following cost-function can be defined

$$\min_{\beta_p} \left| \mathbf{w}^H \mathbf{Y}(\kappa) - (\beta_1 \mathbf{a}^T(f_1) + \beta_2 \mathbf{a}^T(f_2)) \right|^2,$$

which yields

$$\hat{\beta}_1 = \frac{\mathbf{w}^H \mathbf{Y}(\kappa) \mathbf{a}^*(f_1)}{\mathbf{a}^H(f_1) \mathbf{a}(f_1)} - \beta_2 \frac{\mathbf{a}^T(f_2) \mathbf{a}^*(f_1)}{\mathbf{a}^H(f_1) \mathbf{a}(f_1)}, \quad (4.19)$$

$$\hat{\beta}_2 = \frac{\mathbf{w}^H \mathbf{Y}(\kappa) \mathbf{a}^*(f_2)}{\mathbf{a}^H(f_2) \mathbf{a}(f_2)} - \beta_1 \frac{\mathbf{a}^T(f_1) \mathbf{a}^*(f_2)}{\mathbf{a}^H(f_2) \mathbf{a}(f_2)}, \quad (4.20)$$

where  $f_1$  and  $f_2$  are sweep frequencies. To further analyze the above equations, we find

$$\mathbf{w}^H \mathbf{Y}(\kappa) = \beta_1 \mathbf{a}^T(f_{d_1}) + \beta_2 \mathbf{a}^T(f_{d_2}) + \mathbf{w}^H \mathbf{V}(\kappa).$$

Inserting  $\mathbf{w}^H \mathbf{Y}(\kappa)$  in (4.19) and (4.20), we can have three cases to discuss.

**Case 1:**  $f_1 = f_{d_1}$  and  $f_2 = f_{d_2}$

Inserting these values in (4.19) and (4.20) yields

$$\hat{\beta}_1 = \beta_1 + \epsilon_1.$$

$$\hat{\beta}_2 = \beta_2 + \epsilon_2.$$

Here, we define  $\epsilon_1$  as the ratio of  $\mathbf{w}^H \mathbf{V}(\kappa) \mathbf{a}^T(f_{d_1})$  to  $\mathbf{a}^H(f_{d_1}) \mathbf{a}(f_{d_1})$ , and  $\epsilon_2$  as the ratio of  $\mathbf{w}^H \mathbf{V}(\kappa) \mathbf{a}^T(f_{d_2})$  to  $\mathbf{a}^H(f_{d_2}) \mathbf{a}(f_{d_2})$ . As the Capon beamformer is designed to suppress noise and interference signals, and since  $\mathbf{a}^H(f_{d_p}) \mathbf{a}(f_{d_p}) = N_c$  for  $p = 1, 2$ , we can expect the values of  $\epsilon_1$  and  $\epsilon_2$  to be extremely small.

**Case 2:**  $f_1 = f_{d_1}$  and  $f_2 \neq f_{d_2}$

Inserting these values in (4.19) and (4.20) yields

$$\hat{\beta}_1 = \beta_1 + \beta_2 \frac{(\mathbf{a}^T(f_{d_2}) - \mathbf{a}^T(f_2)) \mathbf{a}^*(f_{d_1})}{\mathbf{a}^H(f_{d_1}) \mathbf{a}(f_{d_1})} + \epsilon_1, \quad (4.21)$$

$$\hat{\beta}_2 = \beta_2 \frac{(\mathbf{a}^T(f_{d_2}) \mathbf{a}^*(f_2))}{\mathbf{a}^H(f_2) \mathbf{a}(f_2)} + \epsilon_2. \quad (4.22)$$

In this case, it can be observed in (4.21) that  $\hat{\beta}_1$  can be measured accurately iff  $f_2 = f_{d_2}$ . Here, depending on the difference between the true and assumed value of  $f_{d_2}$ , the second term in (4.21) contributes to the value of  $\beta_1$ . This also suggests a wide lobe along the  $f_2$  axis for a fixed value of  $f_1$ . Similarly, as expected when  $f_2 \neq f_{d_2}$ , the value of  $\beta_2$  cannot be estimated accurately.

**Case 3:**  $f_1 \neq f_{d_1}$  and  $f_2 = f_{d_2}$

Similar to Case 2, we can expect the same results for Case 3. Both Case 2 and Case 3 reveal that the width of the estimation lobes of  $\beta_p$ 's will be wide along the Doppler axis.

Based on the results obtained from the aforementioned cases, it can be concluded that using this technique enables achieving good resolution for estimating  $\theta$  (the angle of the target), but it may not provide the same level of resolution for estimating Doppler shifts. Another issue that arises using the conventional algorithms for this and the similar other problem is if the difference between the amplitudes of both frequencies is high, the low-frequency component can be masked. To overcome such challenges, our novel proposed technique, reformulate the problem given in (4.17) and couples  $\beta_1$  and  $\beta_2$  to estimate both quantities jointly. Therefore, our technique not only enhances the resolution of the Doppler frequencies but also overcomes the high amplitude difference problem as described in the next section.

### **High-Resolution Doppler Frequencies Estimation:**

This section proposes a Capon-like algorithm to estimate the Doppler frequencies. Unlike the Capon algorithm, our proposed algorithm applies constraints on two terms. We reformulate the model given in (4.12) for high-resolution Doppler

frequency estimation as

$$\begin{aligned} \mathbf{Y}_t(\kappa) &= \mathbf{Y}^T(\kappa) = \left( \beta_1 \mathbf{a}(f_{d_1}) + \beta_2 \mathbf{a}(f_{d_2}) \right) \mathbf{a}^T(\theta_0) + \mathbf{V}_t(\kappa), \\ &= \begin{bmatrix} \mathbf{a}(f_{d_1}) & \mathbf{a}(f_{d_2}) \end{bmatrix} \begin{bmatrix} \beta_1 \\ \beta_2 \end{bmatrix} \mathbf{a}^T(\theta_0) + \mathbf{V}_t(\kappa), \end{aligned} \quad (4.23)$$

where  $\mathbf{Y}_t(\kappa) \in \mathcal{C}^{N_c \times n_R}$ . Similar to the previous case, the Capon-like weight vector,  $\mathbf{w}$ , to maximize the SINR for the estimation of  $\beta_p$  can be derived by solving the following constrained optimization problem

$$\begin{aligned} \min_{\mathbf{w}} & \left( \mathbf{w}^H \mathbf{E} \{ \mathbf{Y}_t \mathbf{Y}_t^H \} \mathbf{w} \right) \\ \text{subject to} & \quad \mathbf{w}^H \begin{bmatrix} \mathbf{a}(f_1) & \mathbf{a}(f_2) \end{bmatrix} = \begin{bmatrix} 1 & 1 \end{bmatrix}. \end{aligned} \quad (4.24)$$

The solution to the constrained optimization problem in (4.24) can be derived by minimizing the cost function

$$J = \mathbf{w}^H \mathbf{R}_t \mathbf{w} + \left( \mathbf{w}^H \begin{bmatrix} \mathbf{a}(f_1) & \mathbf{a}(f_2) \end{bmatrix} - \begin{bmatrix} 1 & 1 \end{bmatrix} \right) \bar{\lambda},$$

which yields

$$\mathbf{w} = \mathbf{R}_t^{-1} \begin{bmatrix} \mathbf{a}(f_1) & \mathbf{a}(f_2) \end{bmatrix} \mathbf{H}^{-1} \begin{bmatrix} 1 \\ 1 \end{bmatrix}, \quad (4.25)$$

where  $f_1$  and  $f_2$  are sweep Doppler frequencies,

$$\begin{aligned} \mathbf{R}_t &= \mathbf{E} \{ \mathbf{Y}_t(\kappa) \mathbf{Y}_t^H(\kappa) \}, \\ \text{and } \mathbf{H} &= \begin{bmatrix} \mathbf{a}^H(f_1) \\ \mathbf{a}^H(f_2) \end{bmatrix} \mathbf{R}_t^{-1} \begin{bmatrix} \mathbf{a}(f_1) & \mathbf{a}(f_2) \end{bmatrix}. \end{aligned}$$

Applying the derived beamformer on (4.23), when  $f_1$  and  $f_2$  in weight vector  $\mathbf{w}$  are true quantities, we get

$$\begin{aligned}\mathbf{w}^H \mathbf{Y}_t(\kappa) &= \mathbf{w}^H \begin{bmatrix} \mathbf{a}(f_{d_1}) & \mathbf{a}(f_{d_2}) \end{bmatrix} \begin{bmatrix} \beta_1 \\ \beta_2 \end{bmatrix} \mathbf{a}^T(\theta_0) + \mathbf{w}^H \mathbf{V}_t, \\ &= (\beta_1 + \beta_2) \mathbf{a}^T(\theta_0) + \mathbf{w}^H \mathbf{V}_t.\end{aligned}$$

The above equation allows us to estimate  $\beta_1$  and  $\beta_2$  jointly, and to estimate the joint quantity the corresponding problem can be set up as

$$\beta = \min_{\tilde{\beta}} \left| \mathbf{w}^H \mathbf{Y}_t - \tilde{\beta} \mathbf{a}^T(\theta_0) \right|^2,$$

where  $\beta = \beta_1 + \beta_2$ . The solution to the above minimization problem yields

$$\hat{\beta} = \frac{\mathbf{w}^H \mathbf{Y}_t \mathbf{a}^*(\hat{\theta})}{\mathbf{a}^H(\hat{\theta}) \mathbf{a}(\hat{\theta})}. \quad (4.26)$$

To see the effectiveness of the proposed algorithm, we conduct a further analysis of previously mentioned equation. By substituting (4.25) into the expression  $\mathbf{w}^H \mathbf{Y}_t(\kappa)$ , we can express it as

$$\begin{aligned}\mathbf{w}^H \mathbf{Y}_t(\kappa) &= \begin{bmatrix} 1 & 1 \end{bmatrix} \left( \begin{bmatrix} \mathbf{a}^H(f_1) \\ \mathbf{a}^H(f_2) \end{bmatrix} \mathbf{R}_t^{-1} \begin{bmatrix} \mathbf{a}(f_1) & \mathbf{a}(f_2) \end{bmatrix} \right)^{-1} \begin{bmatrix} \mathbf{a}^H(f_1) \\ \mathbf{a}^H(f_2) \end{bmatrix} \mathbf{R}_t^{-1} \\ &\quad \times \begin{bmatrix} \mathbf{a}(f_{d_1}) & \mathbf{a}(f_{d_2}) \end{bmatrix} \begin{bmatrix} \beta_1 \\ \beta_2 \end{bmatrix} \mathbf{a}^T(\theta_l) + \mathbf{w}^H \mathbf{V}_t\end{aligned} \quad (4.27)$$

Assuming  $\alpha_{p,q} = \mathbf{a}^H(f_p) \mathbf{R}_t^{-1} \mathbf{a}(f_q)$ , (4.27) can be written in compact form as

$$\mathbf{w}^H \mathbf{Y}_t = \mathbf{w}^H \mathbf{V}_t + \begin{bmatrix} 1 & 1 \end{bmatrix} \begin{bmatrix} \alpha_{1,1} & \alpha_{1,2} \\ \alpha_{2,1} & \alpha_{2,2} \end{bmatrix}^{-1} \begin{bmatrix} \alpha_{1,d_1} & \alpha_{1,d_2} \\ \alpha_{2,d_1} & \alpha_{2,d_2} \end{bmatrix} \begin{bmatrix} \beta_1 \\ \beta_2 \end{bmatrix} \mathbf{a}^T(\theta_l).$$

Therefore, the estimated value of  $\hat{\beta}$  using (4.26) and  $\alpha_{q,p} = \alpha_{p,q}^*$  can be written

as

$$\hat{\beta} = [1 \ 1] \begin{bmatrix} \alpha_{1,1} & \alpha_{1,2} \\ \alpha_{1,2}^* & \alpha_{2,2} \end{bmatrix}^{-1} \begin{bmatrix} \alpha_{1,d_1} & \alpha_{1,d_2} \\ \alpha_{2,d_1} & \alpha_{2,d_2} \end{bmatrix} \begin{bmatrix} \beta_1 \\ \beta_2 \end{bmatrix} + \epsilon_3. \quad (4.28)$$

where  $\epsilon_3 = \frac{\mathbf{w}^H \mathbf{V}_t \mathbf{a}^*(\theta_t)}{n_R}$  is a small quantity as mentioned earlier and will be ignored in the following derivations. Now we will analyze the estimated value of  $\beta$  for different values of sweep Doppler frequencies.

**Case 1:** When  $f_1 = f_{d_1}$  and  $f_2 = f_{d_2}$ , the value of  $\beta$  comes out to be

$$\begin{aligned} \hat{\beta} &= \begin{bmatrix} 1 & 1 \end{bmatrix} \begin{bmatrix} \alpha_{d_1,d_1} & \alpha_{d_1,d_2} \\ \alpha_{d_2,d_1} & \alpha_{d_2,d_2} \end{bmatrix}^{-1} \begin{bmatrix} \alpha_{d_1,d_1} & \alpha_{d_1,d_2} \\ \alpha_{d_2,d_1} & \alpha_{d_2,d_2} \end{bmatrix} \begin{bmatrix} \beta_1 \\ \beta_2 \end{bmatrix}, \\ &= \begin{bmatrix} 1 & 1 \end{bmatrix} \begin{bmatrix} \beta_1 \\ \beta_2 \end{bmatrix}, \\ &= \beta_1 + \beta_2. \end{aligned}$$

It is evident from the preceding scenario that precise estimation of the value of  $\beta$  can be achieved when the test values match the actual values of the Doppler frequencies. It is important to note that in scenarios where  $\beta_1 = -\beta_2$ , the proposed method will not be applicable. This is because the individual terms of  $\beta$  can potentially cancel each other. However, it's crucial to emphasize that encountering this specific scenario is exceptionally rare.

**Case 2:** When  $f_1 = f_{d_1}$  and  $f_2 \neq f_{d_2}$ , the estimated value of  $\beta$  using (4.28) can be written as

$$\hat{\beta} = [1 \ 1] \begin{bmatrix} \alpha_{d_1,d_1} & \alpha_{d_1,2} \\ \alpha_{d_1,2}^* & \alpha_{2,2} \end{bmatrix}^{-1} \begin{bmatrix} \alpha_{d_1,d_1} & \alpha_{d_1,d_2} \\ \alpha_{2,d_1} & \alpha_{2,d_2} \end{bmatrix} \begin{bmatrix} \beta_1 \\ \beta_2 \end{bmatrix}. \quad (4.29)$$

Upon further analysis of (4.29), it becomes apparent that the value of  $\beta$  can be expressed as

$$\hat{\beta} = \beta_1 + \epsilon\beta_2 \approx 0, \quad (4.30)$$

where  $\epsilon \approx -\beta_1/\beta_2$ . Detailed proof of this relationship can be found in Appendix A.

**Case 3:** When  $f_1 \neq f_{d_1}$  and  $f_2 = f_{d_2}$ , the estimated value of  $\beta$  again becomes zero and can be expressed as

$$\hat{\beta} = \epsilon\beta_1 + \beta_2 \approx 0. \quad (4.31)$$

where  $\epsilon \approx -\beta_2/\beta_1$ , which results in  $\hat{\beta} = 0$ . To prove this case, one can follow the steps similar to outlined in Appendix A. This finding further confirms the effectiveness of the proposed technique.

**Case 4:** When  $f_1 \neq f_{d_1}$  and  $f_2 \neq f_{d_2}$ . In this case,  $\hat{\beta}$  can be written as

$$\hat{\beta} \approx 0$$

Detailed proof for this case can be found in Appendix B. The steps of the overall algorithm are summarized in algorithm 1.

---

**Algorithm 1** Proposed Algorithm

---

**1. Range Estimation and Selection:**  $R_0$

**2. DOA Estimation:**

$$\mathbf{R} = \frac{\mathbf{Y}\mathbf{Y}^H}{N_c}$$

$$\mathbf{w} = \frac{\mathbf{R}^{-1}\mathbf{a}(\theta_0)}{\mathbf{a}^H(\theta_0)\mathbf{R}^{-1}\mathbf{a}(\theta_0)}$$

$$\hat{\theta} = \arg \max_{\theta} \mathbf{w}^H \mathbf{E} \{ \mathbf{Y}\mathbf{Y}^H \} \mathbf{w}$$

**3. Doppler frequency Estimation:**

$$\mathbf{Y}_t = \mathbf{Y}^T$$

$$\mathbf{R}_t = \frac{\mathbf{Y}_t\mathbf{Y}_t^H}{N_R}$$

$$\mathbf{H} = \begin{bmatrix} \mathbf{a}^H(f_1) \\ \mathbf{a}^H(f_2) \end{bmatrix} \mathbf{R}_t^{-1} [ \mathbf{a}(f_1) \quad \mathbf{a}(f_2) ]$$

$$\mathbf{w} = \mathbf{R}_t^{-1} [ \mathbf{a}(f_1) \quad \mathbf{a}(f_2) ] \mathbf{H}^{-1} \begin{bmatrix} 1 \\ 1 \end{bmatrix}$$

$$\hat{\beta} = \frac{\mathbf{w}^H \mathbf{Y}_t \mathbf{a}^*(\hat{\theta})}{\mathbf{a}^H(\hat{\theta}) \mathbf{a}(\hat{\theta})}$$

$$\hat{f}_d = \arg \max_{f_d} \mathbf{w}^H \mathbf{E} \{ \mathbf{Y}_t \mathbf{Y}_t^H \} \mathbf{w}$$


---

## 4.2 Non-Contact Dehydration Status Monitoring

### 4.2.1 Introduction

Beyond monitoring vital signs, falling detection, and depression, monitoring dehydration levels is crucial in healthcare. Dehydration occurs when the body loses more fluid than it takes in, affecting normal function. It can happen on hot days with excessive sweating or from not drinking enough water. Dehydration is a serious health issue, especially for vulnerable groups like the elderly, infants, and those with chronic illnesses. Early detection and continuous monitoring are essential to prevent severe complications and ensure timely treatment. Effective monitoring of dehydration in healthcare care can significantly improve patient care, reduce hospital admissions, and improve overall health outcomes. Traditional methods of measuring dehydration include assessing physical signs such as dry mouth, rapid heartbeat, and low blood pressure. Blood tests can measure electrolyte levels, blood urea nitrogen (BUN), and serum osmolality, offering precise insights into a patient's hydration status. Urine analysis involves monitoring urine output and specific gravity, which also indicate hydration levels. However, these methods are invasive, uncomfortable, and not ideal for continuous monitoring.

Non-invasive dehydration monitoring methods often use wearable sensors, such as oximeters, smartwatches, and wristbands to capture photoplethysmography (PPG) and electro-dermal activity (EDA) signals, which are then analyzed using ML algorithms. For example, [77] used EDA and PPG data from 17 subjects to detect mild dehydration through autonomic responses to cognitive stress, achieving notable results. The authors in [78] used EDA data from 16 subjects in different postures to classify hydration levels with a hybrid Bi-LSTM neural network. The work in [79] used PPG data from 17 dehydrated patients in an emergency setting, achieving 67.91% precision with an SVM classifier. Similarly, the work in [80] combined data on EDA, skin temperature, heart rate, and

BMI of 16 participants during physical activity to quantify fluid loss. A real-time Android tool was developed using EDA data in [81], achieving an accuracy of 84.5%. Similarly, [82] used EDA data from five subjects in different activities and achieved 91.3% accuracy with a random forest classifier. In another study, [83] reported an accuracy of 87.78% for the detection of dehydration using a k-NN classifier with EDA data. Finally, [84] took a different approach using data from the leg skin microbiome of 63 female subjects to predict skin hydration levels and other biomarkers.

Integrating non-contact monitoring technologies into healthcare systems has the potential to revolutionize dehydration management. These technologies provide continuous and accurate monitoring, improving patient comfort and compliance. They can be easily incorporated into existing healthcare settings, such as hospitals, nursing homes and remote patient monitoring systems, offering comprehensive and efficient care. As the demand for advanced healthcare solutions grows, developing and implementing non-contact dehydration monitoring technologies is a significant step forward. This work aims to explore radar-based dehydration monitoring.

However, for radar-based applications that use machine learning and deep learning, a major challenge is the availability of labeled data. Purchasing a large set of labeled training data for radar applications is generally impractical. Due to the lack of publicly available labeled radar data sets suitable for assessing dehydration, we developed custom data sets for this work. We collected data set under controlled conditions: from fasting individuals, called the Fasting data set. These data sets provide the necessary ground truth for training and validating our radar-based dehydration monitoring system.

#### **4.2.2 Contributions**

In this work, we consider ML methods and introduce wavelet scattering transform to extract features to improve the accuracy of non-invasive and non-contact based

dehydration classification. We use FMCW radar working at 77 GHz frequency with 2 GHz bandwidth. Radar scans the target scene and collect reflections from target which contains the information related to dehydration. We have collected measurements from multiple subjects and labelled them under suitable conditions and verify the proposed methodology. The important contributions of the paper are highlighted as follows:

- We introduce an innovative non-invasive approach to dehydration classification using FMCW radar.
- Due to the lack of labeled data for radar-based dehydration monitoring, we develop and label two distinct datasets under controlled conditions. The Sports Dataset includes measurements from athletes, and The Fasting Dataset contains data from individuals observing fasting.
- We propose a pre-processing technique to isolates the target of interest (TOI) from the received signals, ensuring that the features used for classification accurately reflect the subject's dehydration status. This step is crucial for improving the reliability and performance of our proposed methodology.
- We proposed wavelet scattering transform feature extraction method to extract nonlinear features to enhance the classification.

### 4.2.3 Signal Model

The permittivity,  $\epsilon = \epsilon' - j\epsilon''$ , of a material is a complex quantity. The real part of the permittivity,  $\epsilon'$ , determines how much the material slows down the EM wave, while the imaginary part,  $\epsilon''$ , represents the material's ability to dissipate energy. In a vacuum, there is nothing to interact with the EM waves, so the wave propagates at the speed of light without slowing down. Thus, the real part of the permittivity is  $\epsilon_o$  (a non-zero constant), while the imaginary part is zero because the vacuum cannot dissipate or store energy. For an insulator, the

material slows down the EM waves relative to a vacuum, so its real part  $\epsilon'$  is greater than  $\epsilon_0$ . Additionally, if the insulator is not perfect, it can store some energy, resulting in a small but non-zero imaginary part  $\epsilon''$ . For a conductor, the permittivity is dominated by the imaginary part  $\epsilon''$ , which is very large due to the metal's high conductivity. This large imaginary part indicates that the material strongly dissipates the energy of the EM wave, causing it to attenuate rapidly within a very short distance (known as the skin depth). The real part  $\epsilon'$  of the permittivity of conductor is typically negative at high frequencies, reflecting the material's ability to reflect EM waves rather than slow them down. This is why metals are highly reflective and opaque to EM waves.

The reflection of millimeter waves depends on the skin's permittivity, which is inversely proportional to the incident frequency, and influenced by the water content in its various layers [85, 86]. Frequencies above 30GHz attenuates to zero at the epidermis, layer close to the skin, the 24GHz can penetrate further and attenuates to zero at the dermis, while the lower frequencies can penetrate further deep.

Consider a scenario, as shown in Fig. 4.4, where a patient's chest is exposed to electromagnetic (EM) radiation from a radar transmitting a FMCW signal

$$s(t) = Ae^{j2\pi(f_c + \frac{Bt}{2T})t}, \quad (4.32)$$

where  $f_c$  is the carrier frequency of the radar,  $T$  is the pulse width, and  $B$  is the signal bandwidth. The frequency of the transmitted signal at time  $t$ ,  $f(t)$ , can be estimated by differentiating the phase of the signal in (4.32).

As illustrated in Fig. 4.4, when the transmitted waveform interacts with the human body, part of it reflects off the surface, while the rest penetrates the chest and reflects from various internal layers. These reflections originate from different depths, resulting in a received signal composed of multiple frequency components, each with a distinct amplitude. The amplitude of each component is influenced by the body's water content, enabling the analysis of physiological changes based

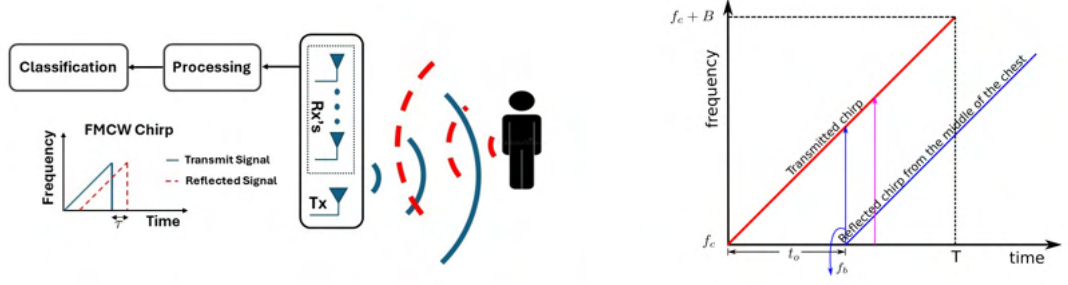


Figure 4.4: The transmitted and reflected signals from the patient’s chest will vary depending on the body’s dehydration level, which acts as a channel. Different frequencies will experience varying levels of attenuation based on the hydration status.

on the reflected signal. Consequently, the exposed body of the patient can be modeled as a dynamic channel, where the impulse response varies in response to fluctuations in the water content. Given this model and defining  $h(t)$  as the body’s impulse response, the signal after reflection from the human’s body at the surface of the chest can be expressed as

$$\begin{aligned}
 r(t) &= h(t) * s(t - t_o), \\
 &= \int h(\tau) e^{j2\pi(f_c + \frac{B\tau}{T})(t - t_o - \tau)} d\tau.
 \end{aligned} \tag{4.33}$$

where  $t_o$  is the time a waveform takes to go from the radar to the surface of the body. It is important to note that the above response holds true only if the body’s impulse response,  $h(t)$ , remains consistent across all frequencies. However, in most practical scenarios,  $h(t)$  may vary with frequency. In such cases, a time-frequency analysis is required to accurately capture the body’s behavior.

In radar systems, where the transmitter and receiver are collocated, the received signal undergoes demodulation at the receiver. This process can be math-

ematically expressed as

$$\begin{aligned}
x(t) &= r(t - t_o)s^*(t), \\
&= \int h(\tau)e^{j2\pi(f_c + \frac{Bt}{2T})(t-2t_o-\tau)}e^{-j2\pi(f_c + \frac{Bt}{2T})t}d\tau, \\
&= e^{-j2\pi(f_c + \frac{Bt}{2T})2t_o} \int h(\tau)e^{-j2\pi(f_c + \frac{Bt}{2T})\tau}d\tau, \\
&= e^{-j2\pi(f_c + \frac{Bt}{2T})2t_o} H\left(f_c + \frac{Bt}{2T}\right) = e^{-j\frac{4\pi R_o}{\lambda}} H\left(f_c + \frac{Bt}{2T}\right) e^{-j2\pi\frac{Bt_o}{T}t}.
\end{aligned}$$

where  $H\left(f_c + \frac{Bt}{2T}\right)$  represents the gain of the human body channel at the time-varying frequency  $\left(f_c + \frac{Bt}{2T}\right)$ . In this formulation, if the body's gain for the input frequency remains constant at any given time  $t$ , the receiver will produce a consistent beat frequency. However, variations in the body's water content can lead to fluctuations in this gain. Consequently, to comprehensively analyze the human body channel response, time-frequency analysis emerges as the most suitable approach and will be employed in the subsequent discussion.

#### 4.2.4 Proposed Methodology

This section outlines the methodology for the proposed dehydration classification problem in three key steps. The first step is the data pre-processing block, which involves cleaning and preparing the received demodulated data for analysis. This is followed by the feature extraction block, where relevant features are identified and extracted from the pre-processed data. Finally, the classification block utilizes these features to classify the dehydration status of the target. Fig. 4.5 provides a block diagram illustrating the overall proposed methodology.

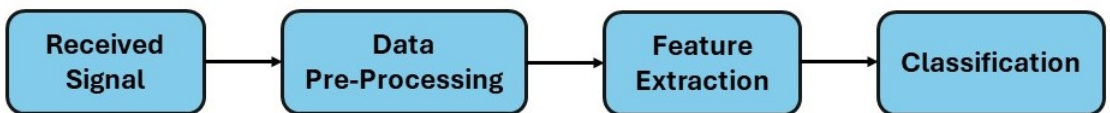


Figure 4.5: Proposed Methodology for dehydration classification.

## Data Pre-Processing:

The data pre-processing block involves cleaning (such as noise removal, clutter reduction, etc.) and preparing the demodulated received data to ensure it is suitable for analysis. The received demodulated signal is passed through a window function (e.g., Hamming or Hanning) to reduce sidelobes and improve target detection which is given by

$$x_{\text{windowed}}(t) = x(t) \times w(t) \quad (4.34)$$

where  $w(t)$  represents Hamming or Hanning window function.

Fast Fourier Transform (FFT) is employed on the windowed demodulated received signal (4.34) to compute the range profiles of different targets. In our approach, we identify the specific beat frequencies ( $f_{b_{min}} < f_{b_0} < f_{b_{max}}$ ) corresponding to the target of interest ( $f_{b_0}$ ) while suppressing undesired beat frequencies i.e., interference or targets other than target of interest. This is achieved by applying a second-order section (SOS) butterworth bandpass filter, designed to maintain a flat frequency response in the passband [87, 88]. This effectively isolates the target of interest signal with minimal distortion while attenuating unwanted frequencies, such as signals from other objects or undesired peaks/targets:

$$y(t) = \text{SOS\_filter}(x_{\text{windowed}}(t)) \quad (4.35)$$

Integrating multiple received antenna's coherently improves the signal-to-noise ratio and enhances target detection. However, in this paper we consider the single receiving antenna. Next, we extract relevant features from pre-processed data using Wavelet Scattering Transform (WST).

## Wavelet Scattering Transform:

Wavelet scattering network allows the extraction of low-variance features from real-valued time series data, suitable for machine learning and deep learning ap-

plications. These features are robust to translations of the input based on a user-defined invariance scale and remain continuous in the presence of deformations. The WST is simply an iterative combination of a deep convolution network, consisting of low-pass filter averaging, wavelet transform, and nonlinear modulus operations [89].

Let consider a  $\Phi(t)$  be the low-pass filter that provides locally translation invariant descriptions of  $y$ . For given time-domain signal,  $y(t)$ , the WST proceeds iteratively: Initially, convolves the input signal with the scaling filter,  $\Phi(t)$  to derive the zeroth-order scattering coefficients  $S_0(t) = y(t) * \Phi(t)$ . This generates a locally translation invariant feature of  $y$ , but also results in the loss of high frequency information. However, lost high frequencies can be recovered subsequent steps of the WST process:

1. **Wavelet Transform and Modulus:** Apply the wavelet transform to the input data using each wavelet filter,  $\Psi_{j_1}(t)$ , from the first filter bank followed by modulus of each filtered output, resulting in the scalogram,  $U_1$  expressed as

$$U_1 = \{|y * \Psi_{j_1}(t)|\}_{j_1 \in \Lambda_1} \quad (4.36)$$

2. **Averaging:** Average each modulus with the scaling filter to obtain the first-order scattering coefficients,  $S_1$  expressed as

$$S_1 = \{|y * \Psi_{j_1}(t)| * \Phi(t)\}_{j_1 \in \Lambda_1} \quad (4.37)$$

After step 2,  $S_1$  have information about the low frequency components of  $|y * \Psi_{j_1}(t)|$ . To recover the high frequency information lost by averaging, repeat the step 1 i.e, Wavelet and modulus operation to  $S_1$  with second filter bank,  $\Psi_{j_2}(t)$ , which is given by

$$U_2 = \{||y * \Psi_{j_1}(t)| * \Psi_{j_2}(t)|\}_{j_1 \in \Lambda_1, j_2 \in \Lambda_2} \quad (4.38)$$

and second order scattering coefficients obtained by

$$S_2 = \{ \|y * \Psi_{j_1}(t) | * \Psi_{j_2}(t) | * \Phi(t) \}_{j_1 \in \Lambda_1, j_2 \in \Lambda_2} \quad (4.39)$$

By iterating the above process will define the wavelet scattering coefficients for higher orders ( $m \geq 2$ ), which can be expressed as

$$S_m = \{ | \dots \|y * \Psi_{j_1}(t) | * \Psi_{j_2}(t) | \dots * \Psi_{j_m}(t) | * \Phi(t) \}_{j_i \in \Lambda_i} \quad (4.40)$$

where  $i = 1, 2, \dots, m$ . After extracting features using the WST, the next step is to feed these features into multiple classifiers to identify the dehydration status.

### **Classification:**

In this section, we detail the final component of our proposed methodology: classification. We train and evaluate a comprehensive range of machine learning and deep learning models to classify dehydration levels accurately. The machine learning methods we implemented include K-Nearest Neighbors (KNN), Support Vector Machines (SVM), Kernel methods, Naive Bayes, and Neural Networks. Each method is selected for its unique ability to capture diverse patterns within the radar data, essential for precise dehydration classification. By rigorously training and testing these models, we aim to determine the most effective algorithm for reliable and efficient non-invasive dehydration monitoring.

## Chapter 5

### Results and Discussion

This chapter presents a comprehensive analysis of the results obtained from both simulated and experimental data for FL-MIMO SAR imaging and biomedical radar applications. The primary objective is to evaluate the effectiveness of the proposed deep learning-based approaches in enhancing SAR imaging resolution and improving biomedical radar-based monitoring techniques. The results are structured to provide a clear comparison between simulated and real-world data, highlighting performance differences and benchmarking these methods against traditional approaches. This chapter is divided into three major sections: FL-MIMO SAR Imaging Results - analyzes the improvements in azimuthal resolution achieved using Deep Basis Pursuit (DBP) and Convolutional Decoder (ConvDecoder) methods compared to traditional approaches. Both simulated and experimental results are presented to validate the effectiveness of these techniques. Biomedical Radar Applications – evaluates the performance of radar-based heart rate (HR) and breathing rate (BR) estimation, as well as dehydration status monitoring. While HR and BR results are presented only for simulated data, the dehydration monitoring analysis includes both simulated and experimental results to assess its feasibility for real-world applications.

The following sections provide an in-depth analysis of the results obtained for both SAR imaging and biomedical radar applications.

#### 5.1 Results of FL-MIMO SAR Imaging

In this section, we present verification of the proposed method on simulated data as well as experimental real data. For all experiments in this work, we have

used a ResNet architecture for the CNN. Input data is vectorized over columns before entering the architecture. Since the data is complex, we consider real and imaginary parts as separate input channels to the CNN. As shown in Fig. 5.1 input to the architecture is a two channel tensor. The proposed architecture consists of 32, 32, and 2 filters, respectively. The final layer consists of only convolution block which is mapped back to the two channels. We implement all convolutional layers with filters of size  $3 \times 1$ . We use euclidean norm loss function for training. The loss is computed in the image domain when ground truth is available i.e., supervised learning and in measurement domain when ground truth is not available i.e., unsupervised learning. We use PyTorch for network implementation.

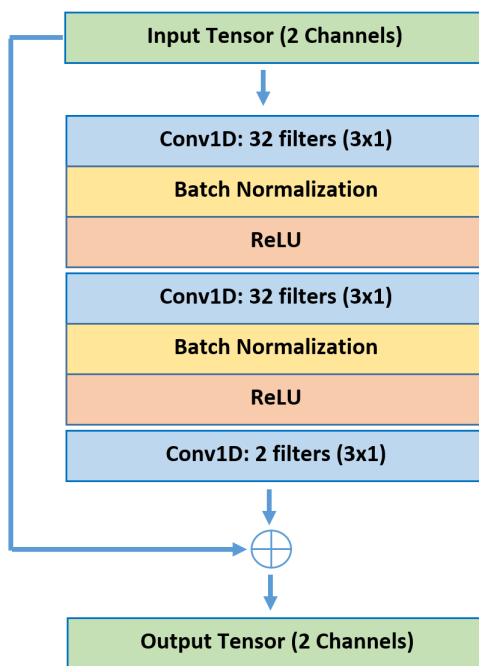


Figure 5.1: Architecture of the CNN-based Denoiser.

### 5.1.1 Simulated Results

We consider FMCW-MIMO radar with two transmit antennas and four receive antennas. MIMO radar is operating at carrier frequency 77GHz. We consider signal bandwidth of 2 GHz. We consider the target scene as a grid in Cartesian

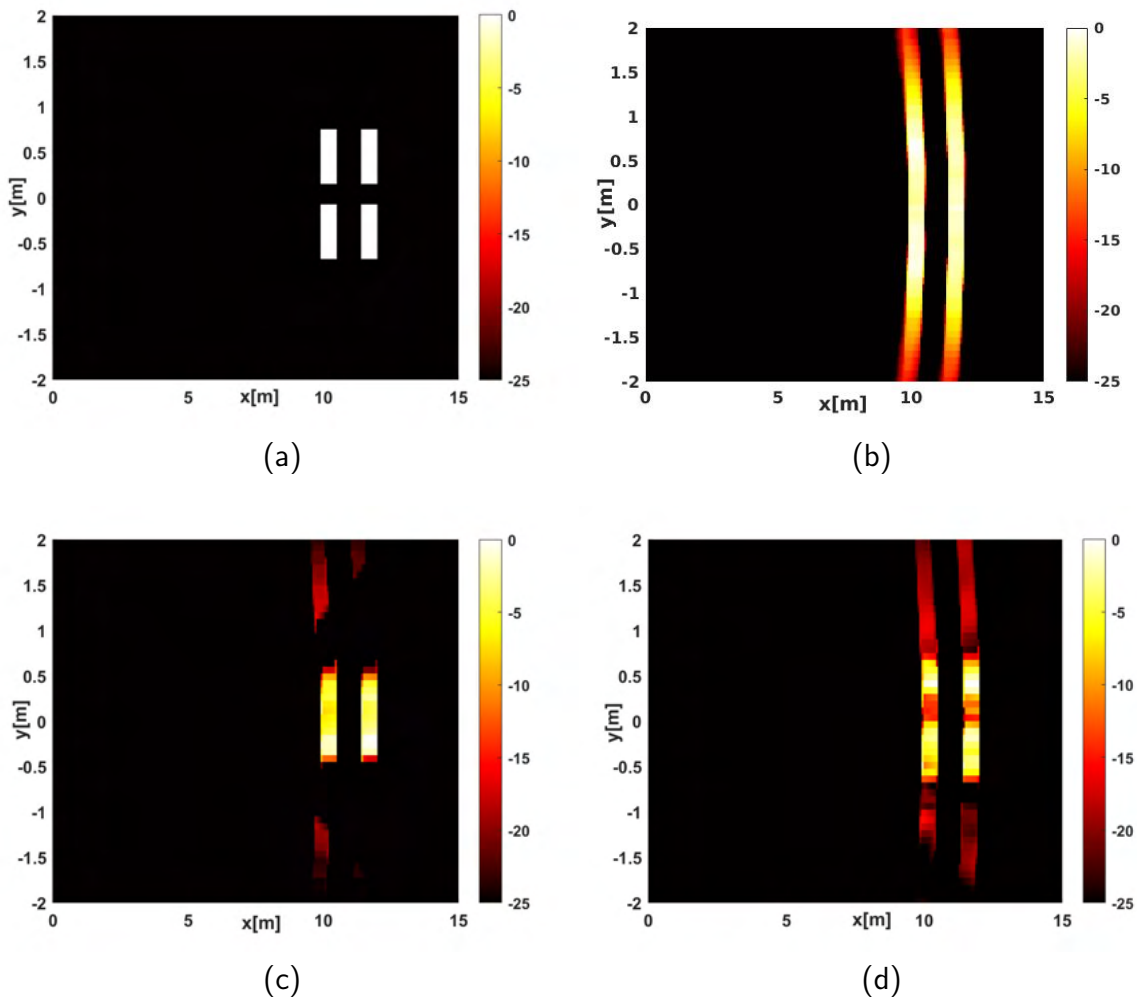


Figure 5.2: Final reconstructed image results for simulated data using (a) Target Scene (b) MF based FL-MIMO-SAR Imaging (c) Compressive sensing based FL-MIMO-SAR Imaging (d) DBP based FL-MIMO-SAR Imaging.

coordinate system. We consider extended targets which occupy a set of cells in the target grid. The size of the cell is same as range resolution in both x and y axis. For simulations, radar moves along the x-axis at  $y = 0$ . We setup the target scene similar to the nature of a typical road scene. We consider 4 targets in this experiment. The targets are separated by 0.375m along y-axis i.e., consist of five cells. Along x-axis, the targets are separated by 0.9m i.e., consist of twelve cells. We place the targets center at a distance of 10m from the radar. Fig. 5.13a shows the simulated target scene. We consider angular coverage of  $50^\circ$  and angular steps of  $0.5^\circ$ . We limit max range per aperture to 25m. We generate the FL-MIMO-SAR measurements by moving MIMO radar along x-axis till 8m

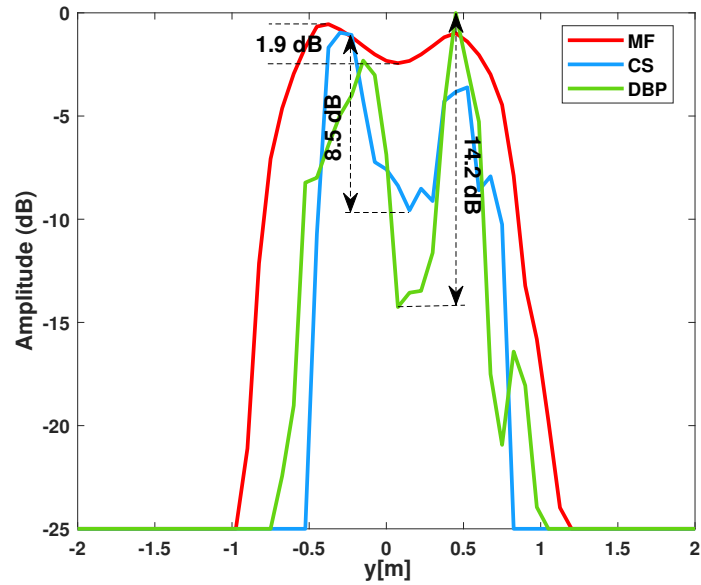


Figure 5.3: Comparison of simulated data Y-magnitude plots for MF, CS and DBP based FL-MIMO-SAR Imaging.

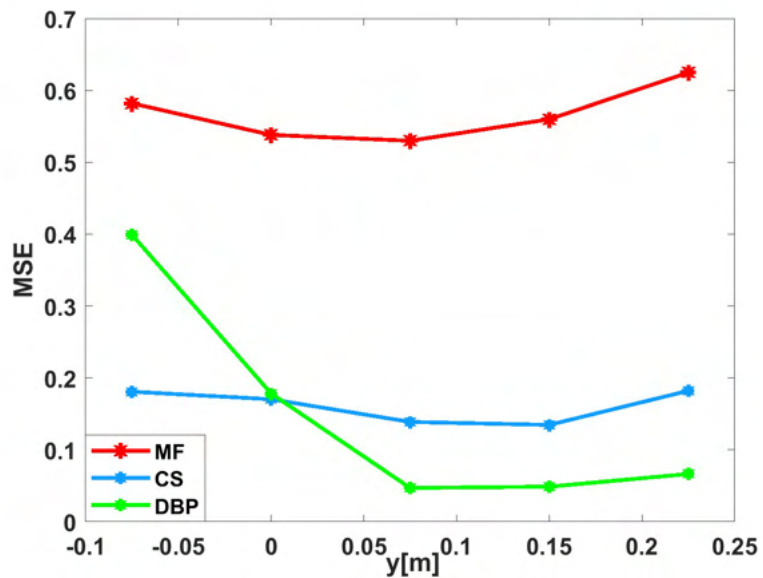


Figure 5.4: Comparison of MSE (at cross-range gap between the targets) on simulated data, for MF-based, CS-based and DBP-based FL-MIMO-SAR Imaging.

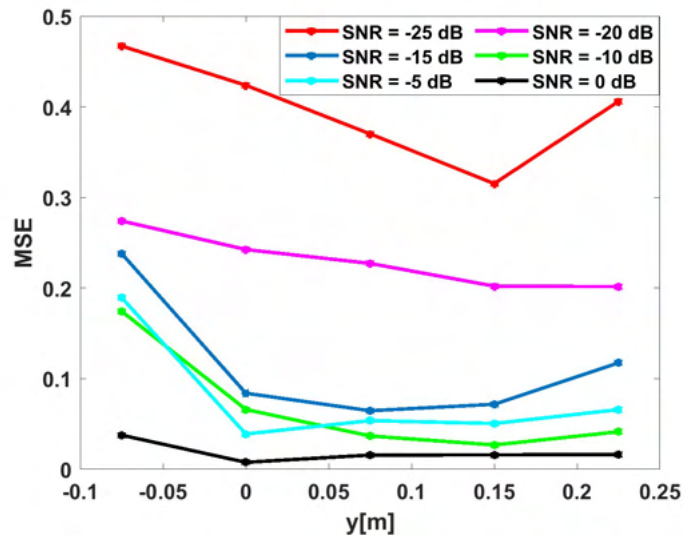


Figure 5.5: MSE plot of simulated target for DBP-based method for different SNRs.

from the origin i.e., 107 aperture steps, where the distance between consecutive aperture steps is one grid cell i.e., 7.5cm (which is the range resolution). The matched filtering (MF)-based reconstruction ( $\mathbf{A}^H \mathbf{y}$ ) with MBP is shown in Fig. 5.13b. As we can see from Fig. 5.13b, targets along the x-axis (range domain) are distinguishable but along the azimuth direction we cannot distinguish the targets. Fig. 5.13d shows the results of state-of-the-art compressive sensing (CS) based reconstructions [25]. CS-based reconstruction is better than MF-based reconstruction but unable to separate the targets clearly along azimuth direction (and takes more time (304.5 minutes) compared with DBP (5.7 minutes)). Fig. 5.13c shows the results of proposed DBP-based reconstruction. We can see better results compared to MF-based and CS-based reconstructions. The targets are easily distinguishable both in range and azimuth domains. From Fig. 5.3 we can see that DBP has better performance in restoring the non-target space, thus, reducing the noise and improving the resolution, in comparison to the other two methods. All the reflectivities in Fig. 5.13, and Fig. 5.3 are in dBs.

We consider the previous scenario of 4 extended targets placed at a distance of 10 m along x-axis. To evaluate the performance of our proposed method, we provide mean squared error (MSE) plots. Specifically, we evaluate the MSE

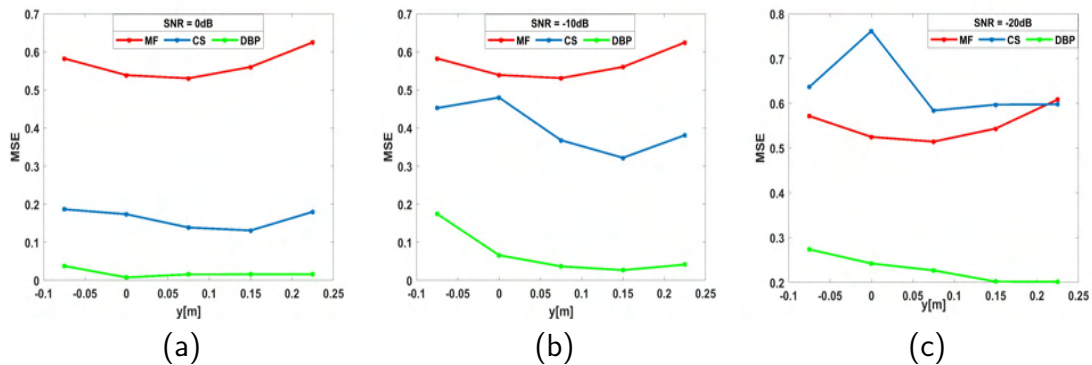


Figure 5.6: Comparison of MSE plots for simulated data using MF-based, CS-based, and DBP-based methods at SNRs: (a) 0dB, (b) -10dB, (c) -20dB.

at the gaps between the targets, along the cross-range (averaged over different range bins). This analysis provides valuable insight into the effectiveness of our method in capturing and reconstructing the gaps accurately, which reflects the statistical nature of resolution enhancement. In Fig. 5.4, we present the MSE plots for different reconstruction methods, i.e., MF, CS, and DBP. From the figure, it can be observed that the DBP-based method outperforms the CS-based and MF-based methods. This indicates that our proposed DBP-based method yields superior resolution enhancement compared to the other methods.

We consider the previous scenario of 4 extended targets placed at a distance of 10m along x-axis. To demonstrate the resilience of our proposed DBP-based method against varying noise levels, we consider the reconstruction performance for different signal-to-noise ratios (SNRs) (i.e., -25 dB, -20 dB, -15 dB, -10 dB, -5 dB, and 0 dB). To evaluate the impact of noise on our method, we present the MSE analysis. The MSE is evaluated at the gaps between the targets along the cross-range. The MSE plots for DBP-based method for different SNRs are shown in Fig. 5.5. From Fig. 5.5, we observe that the DBP-based method excels at reducing the MSE as the SNR increases. Further, we compare the MSE results of the DBP-based method with CS-based and MF-based methods, for different SNRs, as shown in Fig. 5.6. From these results, it is evident that the DBP-based method outperforms the CS-based and MF-based methods in the presence

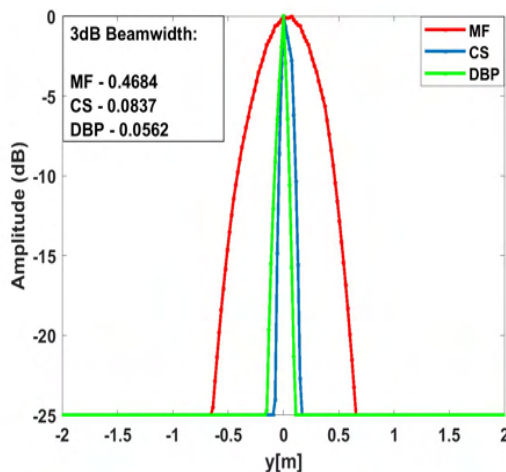


Figure 5.7: Comparison of PSFs for a point target using MF-based, CS-based, and DBP-based FL-MIMO-SAR Imaging.

of varying levels of noise as well.

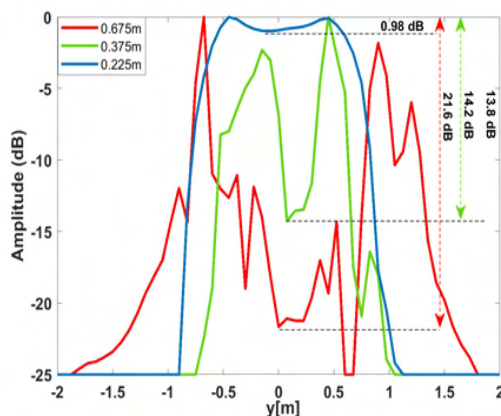


Figure 5.8: Comparison of Y-magnitude plots on simulated data for DBP based FL-MIMO-SAR Imaging for different spacing between the targets along Y-axis.

We considered a scenario with a single point target placed at a distance of 10 m along the x-axis. We generate the FL-MIMOSAR measurements by moving MIMO radar along x-axis till 8 m from the origin i.e., 107 aperture steps, where the distance between consecutive aperture steps is one grid cell i.e., 7.5 cm (which is the range resolution). The point spread function (PSF) of the target for MF-based, CS-based, and DBP-based methods are shown in Fig. 5.7. From Fig. 5.7, we can see that the DBP-based method has better (i.e., smaller) 3-dB beamwidth compared with both MF-based and CS-based methods.

We consider different scenarios with 4 extended targets by varying the sep-

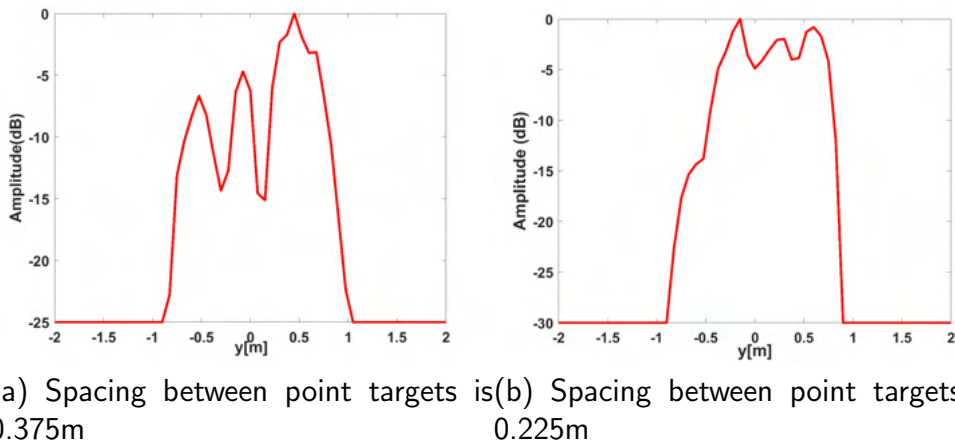


Figure 5.9: Y-magnitude plots on simulated data of three point targets using proposed DBP based FL-MIMO-SAR Imaging for different spacing between the targets along Y-axis.

Table 5.1: Specification of MIMO Radar

Parameter	Value
Carrier frequency	77 GHz
Frequency range	76 - 78 GHz
Transmit bandwidth	2 GHz
Tx activation sequence	[1 2]
Ramp duration	200 $\mu$ s
Sampling rate	10 MHz
Number of samples	2000
Horizontal 3 dB beamwidth (TX)	51 $^\circ$
Horizontal 3 dB beamwidth (RX)	76.5 $^\circ$

aration between targets as, 0.225m, 0.375m and 0.675m along y-axis (azimuth). The magnitude plots are shown in Fig. 5.8. In this case, targets are at 0 $^\circ$  look angle (therefore, we do not expect any SAR gain). In the present scenario of the targets (at a distance of 10m), FL-MIMO-SAR can traditionally resolve the targets separated by a distance of 2.5m (i.e., cross-range resolution). However, our proposed method is able to resolve the targets with a separation of 0.375m (along with suppression of the noise floor), which is an improvement by almost 7

times. Nonetheless, the target separation of 0.225m was not fully recovered.

We have also considered a scenario with three point targets, one in the center and two on the sides, placed at a distance of 10m along x-axis and each target is separated by a distance of a) 0.375m along y-axis and b) 0.225m along y-axis, from the target center. The Y magnitude plots of the recovered image are shown in Fig. 5.9. From Fig. 5.9, we can see the point targets are separated clearly. Theoretically, in such a scenario (with targets at an angle  $2.14^\circ$ ,  $0^\circ$  and  $-2.14^\circ$ ), FL-MIMO-SAR can resolve the targets separated by a distance of 1.24m (i.e., cross-range resolution). However, in this case targets are separated by distance of 0.375m and 0.225m, which is substantially smaller separation than the expected resolution and our proposed method is still able to resolve the targets.

### 5.1.2 Experimental Results

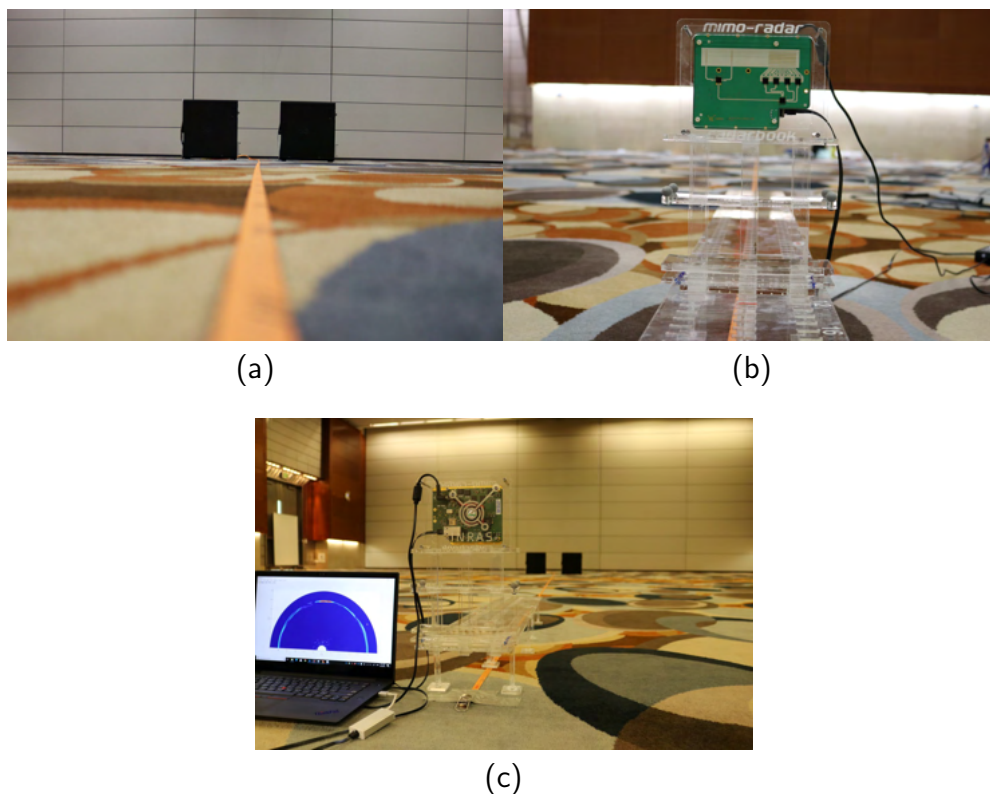


Figure 5.10: (a) Two targets (b) 77 GHz MIMO radarbook (c) FL-MIMO-SAR experimental setup.

We use Inras 77 GHz FMCW-MIMO radarbook [90, 91] with two transmit

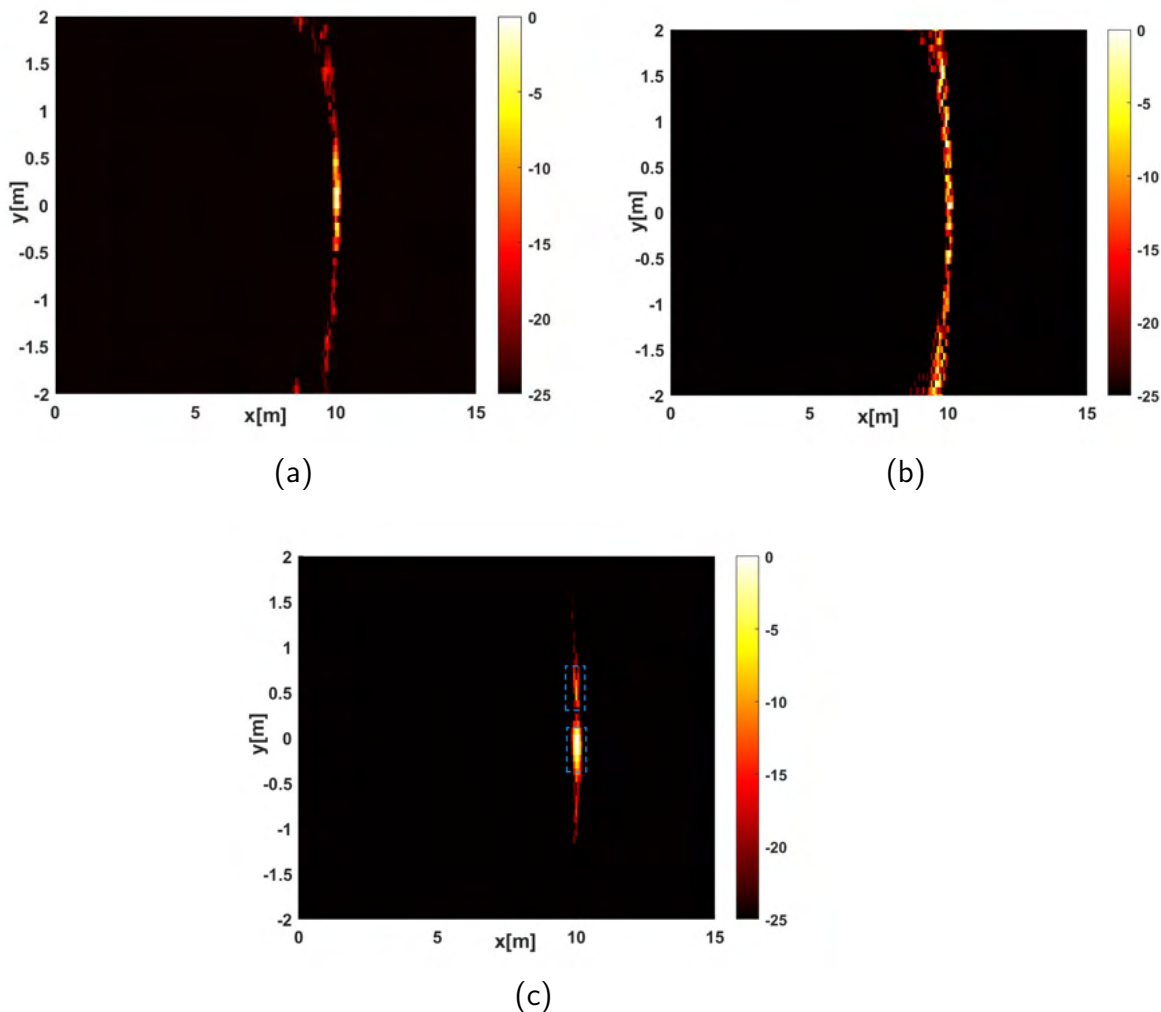


Figure 5.11: Final reconstructed image results for experimental real data using (a) MF based FL-MIMO-SAR Imaging (b) Compressive sensing based FL-MIMO-SAR Imaging (c) DBP based FL-MIMO-SAR Imaging.

(Tx) and 16 receive (Rx) antennas. MIMO radarbook is shown in Fig. 5.10b. The Tx antennas can be activated alternately in order to generate a virtual array. The specifications of FMCW-MIMO radar are shown in table 5.1. We consider two rectangular metallic boxes as stationary targets for experiment. The target scene setup is shown in Fig. 5.10a. The targets are placed at a distance of 10m from MIMO radar along x-axis and separated by 0.4m along y-axis. We have collected the measurements by moving MIMO radar along x-axis till 8m from the origin. The distance between consecutive aperture steps is 2.5cm. The matched filtering based reconstruction ( $\mathbf{A}^H \mathbf{y}$ ) with MBP result is shown in Fig. 5.11a. From Fig. 5.11a, we can observe that the targets along the azimuth direction are

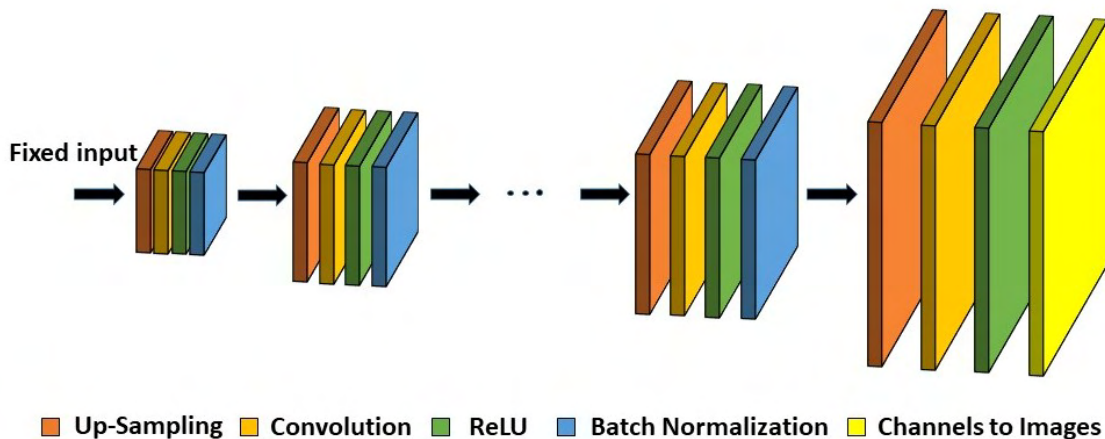


Figure 5.12: ConvDecoder architecture with up-sampling, convolutional, ReLU, and batch normalization layers.

non-distinguishable. Fig. 5.11b shows the results of compressive sensing based reconstruction. CS-based reconstruction is also unable to distinguish the targets along azimuth direction. Fig. 5.11c shows the results of deep learning i.e., DBP based reconstruction. Note, we do not know the target noise statistics ( $\epsilon$ ). So, we considered histogram based noise floor estimation to estimate noise statistics. We can see better results for DBP-based reconstruction compared to MF-based and CS-based reconstructions. Here, targets are easily distinguishable in azimuth domain. All the reflectivities in Fig. 5.11 are in dBs.

### 5.1.3 Simulated Results for ConvDec

We verify the proposed method via simulations. In this work, instead of just point targets, we considered extended targets. In ConvDecoder architecture, real and imaginary parts of images are considered by two separate channels. In the proposed architecture, each layer (except the last layer) consists of the following components: up-sampling, a convolutional operation, ReLU activation function, and Batch Normalization (BN). Fig. 5.12 shows the ConvDecoder architecture. We choose a fixed input (specifically, a randomly generated initialization). The proposed architecture learns the weights by minimizing the loss function (3.32).

We considered FMCW-MIMO radar with two transmitting antennas and four

receiving antennas. The bandwidth and carrier frequency of the radar are 2 GHz and 77 GHz respectively. Four extended targets are placed at a distance of 10m with a separation of 0.375m along the y-axis and 0.9m along the x-axis (shown in Fig. 5.13a). We considered the angular coverage of  $50^\circ$  with angular step  $0.1^\circ$ , i.e.,  $n_\theta = 500$ . By moving toward the target along the x-axis in steps of 1 range bin (7.5cm), we generated the FL-MIMO measurements for each aperture step for a total aperture length of 8m.

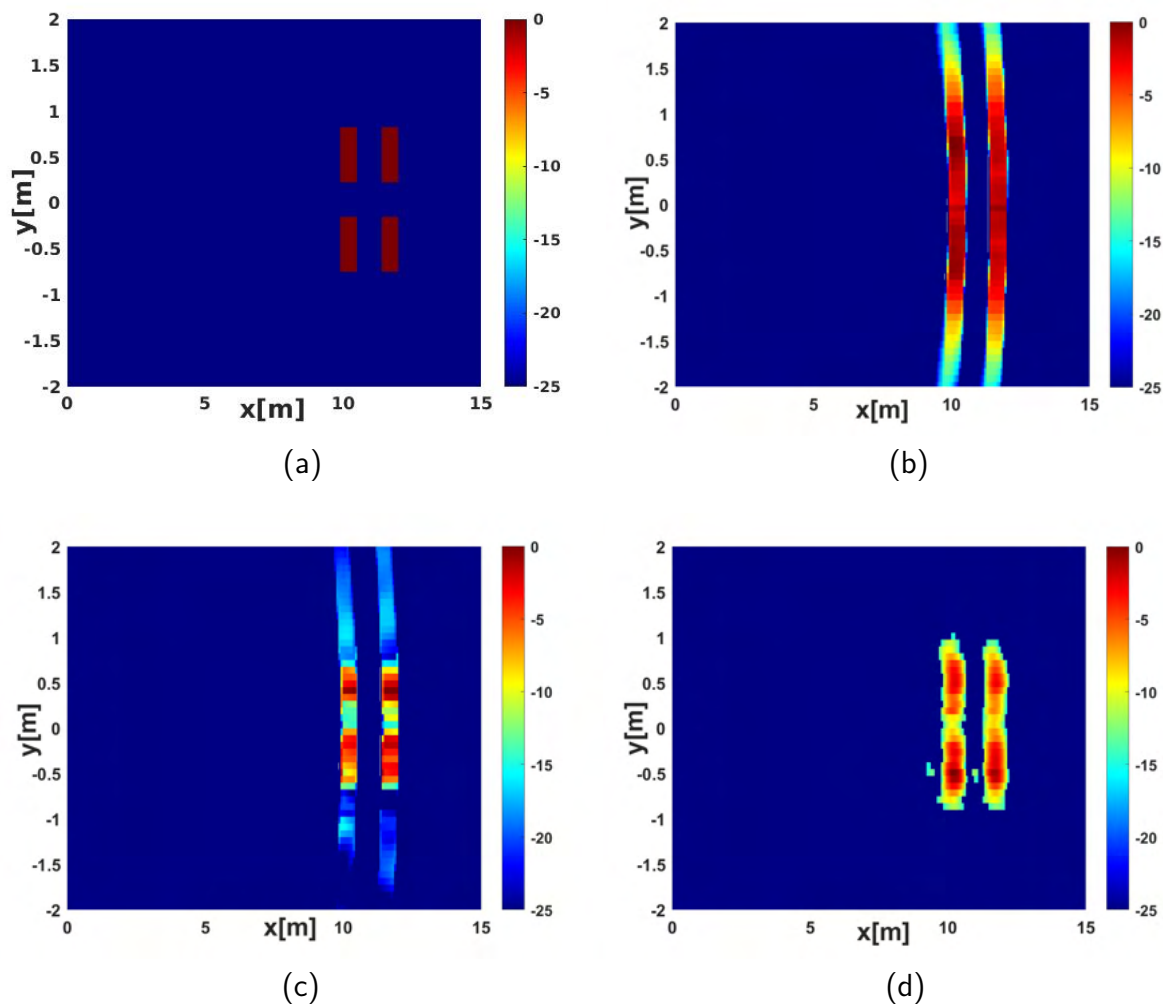


Figure 5.13: Reconstructed image results (a) Target Scene (b) MF-based FL-MIMO-SAR Imaging (c) DBP-based FL-MIMO-SAR Imaging (d) ConvDecoder-based FL-MIMO-SAR Imaging.

Fig. 5.13a shows the target scene. The match-filtering (MF)-based reconstruction ( $\mathbf{A}^H \mathbf{y}$ ) with MBP results are shown in Fig. 5.13b. We can observe that targets along the x-axis (range direction) are clearly separable but not along the

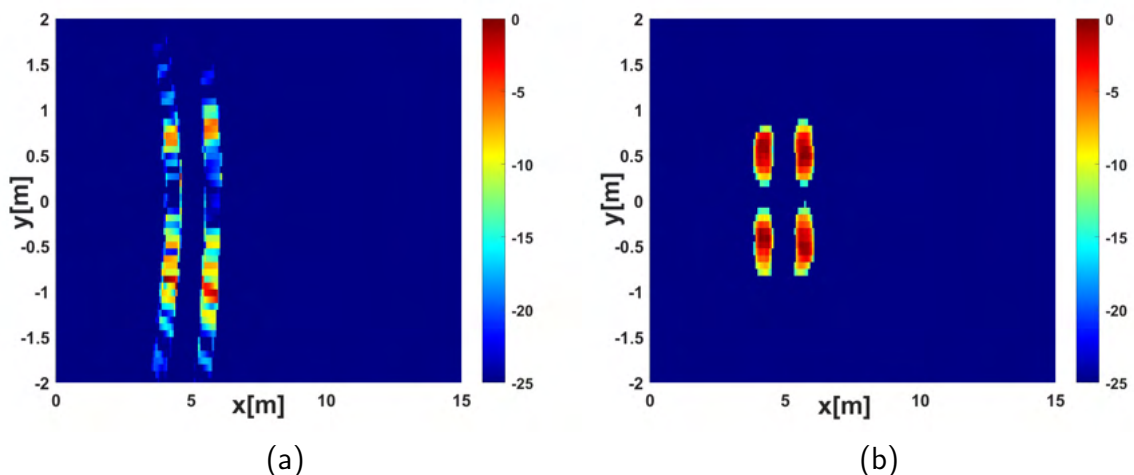


Figure 5.14: Reconstructed image results considering only few aperture steps (a) DBP-based FL-MIMO-SAR Imaging (b) ConvDecoder-based FL-MIMO-SAR Imaging.

y-axis (azimuth direction). The DBP-based reconstructed image is shown in Fig. 5.13c. We can observe that targets are clearly separable along both the x-axis and y-axis. Fig. 5.13d shows the reconstructed image by the proposed ConvDecoder-based method. We can observe that targets are clearly separable along the x-axis and y-axis as well. Additionally, we can observe that sidelobes are suppressed clearly compared to the DBP-based method and MF-based reconstruction.

To compare the ConvDecoder method with the DBP-based method in the case of reduced number of available measurements, we considered only the last few SAR aperture steps (27 steps) of the generated simulated data. The performance results for the DBP-based reconstruction and ConvDecoder-based reconstruction, are shown in Fig. 5.14. We can observe that the proposed ConvDecoder-based method has outperformed the DBP-based method, both in terms of the resolution/separation as well the sidelobe levels.

## 5.2 Results of Heart Rate and Breathing Rate Estimation

We present verification of the proposed method on simulated data. We simulate different scenarios to evaluate the effectiveness of the proposed algorithm.

### 5.2.1 Simulated Results

Table 5.2: Target parameters for the considered experiment

	Range	Angle	Doppler Frequencies	Amplitude(s)
Target 1	3m	$-30^\circ$	1 Hz and 2.5 Hz	$\frac{1+i}{\sqrt{2}}, \frac{1-i}{\sqrt{2}}$
Target 2	9m	$50^\circ$	-1 Hz and -2 Hz	$\frac{0.5-i}{\sqrt{2}}, \frac{1+0.5i}{\sqrt{2}}$
Target 3	5m	$10^\circ$	-1 Hz and 4 Hz	$\frac{1-i}{\sqrt{2}}, \frac{1+0.5i}{\sqrt{2}}$
Target 4	1m	$-60^\circ$	0 Hz	1
Target 5	7m	$0^\circ$	0 Hz	1

In our simulation, we utilize an FMCW radar system equipped with one transmit and 20 receive antennas. The radar operates at a frequency of 24 GHz with a bandwidth of 250 MHz. Each FMCW radar pulse has a duration of  $300\mu\text{s}$  and is transmitted with a pulse-repetition-interval of 50ms. A total of  $N_c = 16$  chirp pulses are transmitted during the experiment. The received signal is sampled at a frequency of 42.66MHz, with  $N_s = 128$  samples collected after the transmission of each chirp pulse. The signal-to-noise ratio is calculated using the following equation

$$\text{SNR} = 10 \log \left( \frac{|\beta_1|^2 + |\beta_2|^2}{\sigma^2} \right),$$

where  $\sigma^2$  is the noise power. In the first simulation, our experimental scenario includes three moving and two stationary targets. The range, angle, and Doppler frequency of each target are given in Table 5.2. During this simulation, we apply the FFT across the fast-time samples collected from each receive antenna. Each FFT output corresponds to a range. For a particular transmitted chirp  $i = \mathcal{I}$ , the fast time FFT outputs from each antenna are collected to form a matrix. By applying FFT across the rows, the angular location of targets, if present in any range bins, can be estimated. The FFT algorithm uses samples from different antennas corresponding to a particular chirp to estimate the angular location. However, the FFT algorithm cannot leverage data from multiple chirps and antennas to achieve high angular resolution. Our proposed algorithm (explained in

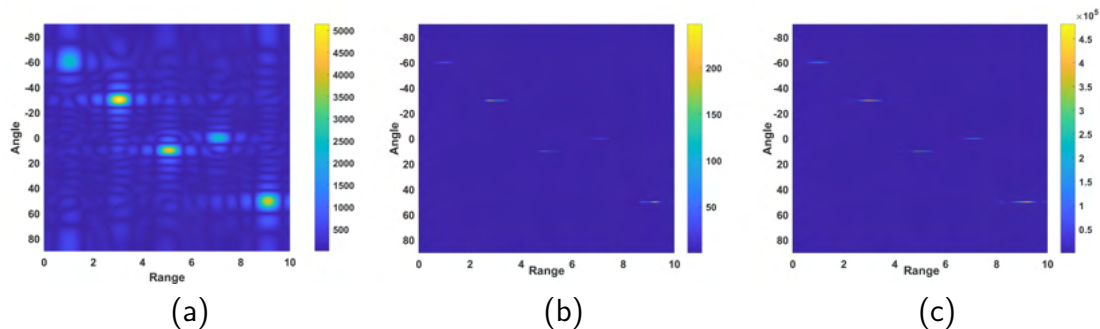


Figure 5.15: Range and DOA estimations for the scenario of five targets using (a) FFT, (b) MUSIC, and (c) Capon.

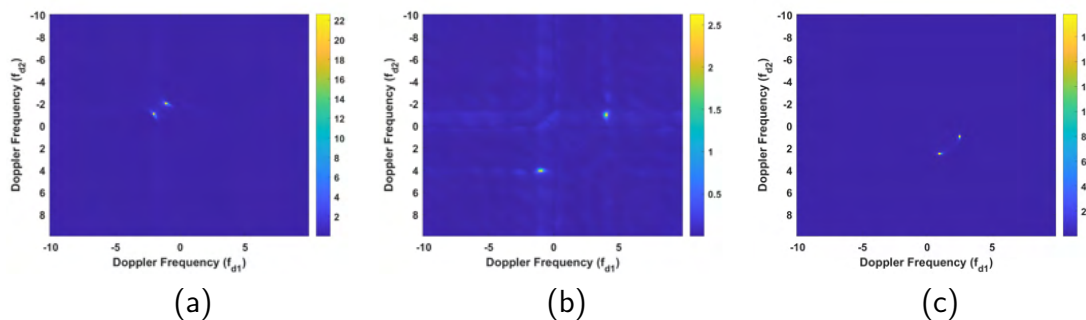


Figure 5.16: Doppler frequencies estimation using proposed method of three moving targets. (a) Target located at 9m introducing Doppler frequencies of -1Hz and -2Hz, (b) target located at 5m introducing Doppler frequencies of -1Hz and 4Hz, and (c) target located at 3m introducing Doppler frequencies of 1Hz and 2.5Hz.

Sec. 4.1.4) and MUSIC algorithm are designed to exploit data from all antennas and chirps to provide higher angular resolution. In Fig. 5.15, we compare the performance of the FFT, MUSIC, and our proposed algorithms. The results demonstrate that MUSIC and our proposed algorithm provide much better angular resolution compared to the FFT-based algorithm. Moreover, our proposed algorithm yields clearer peaks compared to the MUSIC algorithm, as shown in the bar chart.

After successfully estimating the DOA of targets using the Capon algorithm, we utilized our proposed algorithm (as explained in Sec. 4.1.4) to estimate the Doppler frequencies of three moving targets. The corresponding results are illustrated in Fig. 5.16, which exhibit high-resolution sharp peaks for all three targets. These peaks can be easily found by applying any 2D matrix peak search algorithm. It should be noted that the proposed method yields two symmetric,

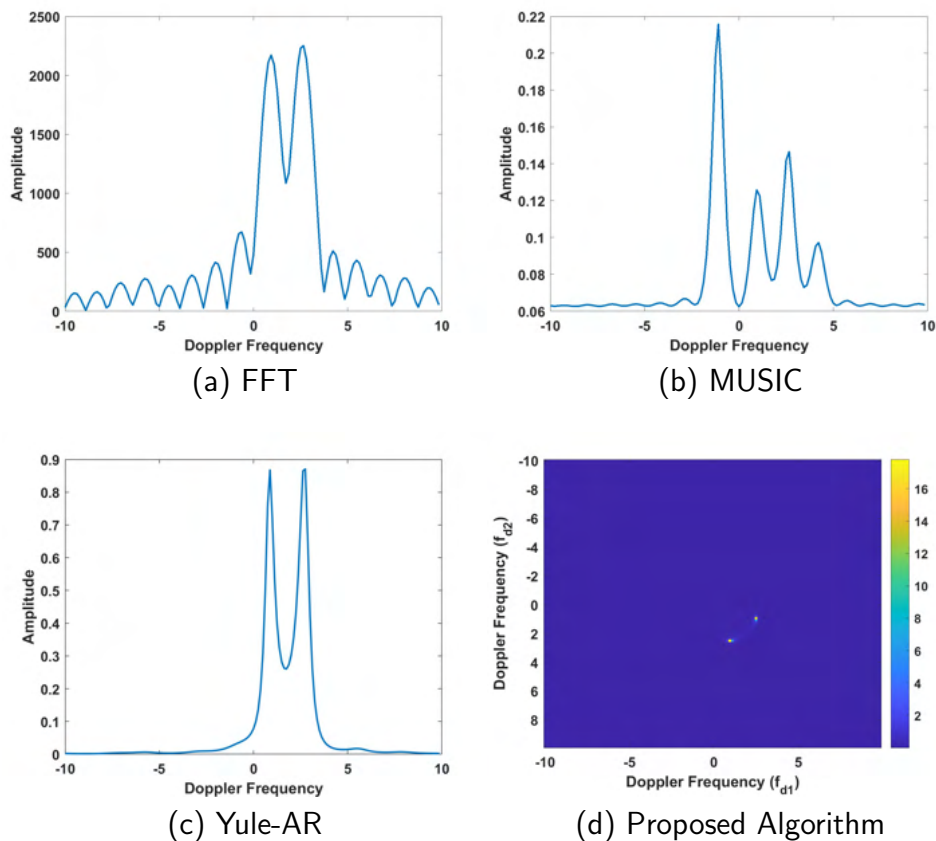


Figure 5.17: Comparison of FFT, MUSIC, Yule-AR, and proposed Capon-based method for the Doppler frequency estimation of target 1 located at a distance of 3m and at an angle of  $-30^\circ$ . The SNR = 0dB and the target induces Doppler frequencies of 1 Hz and 2.5 Hz.

interchangeable solutions, which isn't a major concern when prior knowledge of Doppler frequencies exists. For instance, in vital signs estimation, we know that the heart rate's Doppler frequency is higher than the breathing rate's.

In the third simulation, we conducted a comparative assessment of our proposed algorithm's performance for estimating the Doppler frequencies of target 1 against three established algorithms: FFT, MUSIC, and Yule-AR, the corresponding outcomes are presented in Fig. 5.17. Fig. 5.17a illustrates the results obtained using the FFT algorithm, yielding a poor frequency resolution with significant side lobes. Conversely, Fig. 5.17b displays the output generated by the MUSIC algorithm, which exhibits two additional peaks in addition to the true peak values, albeit with notably reduced side lobes when compared to the FFT-based approach. The Yule-AR algorithm, depicted in Fig. 5.17d, produces

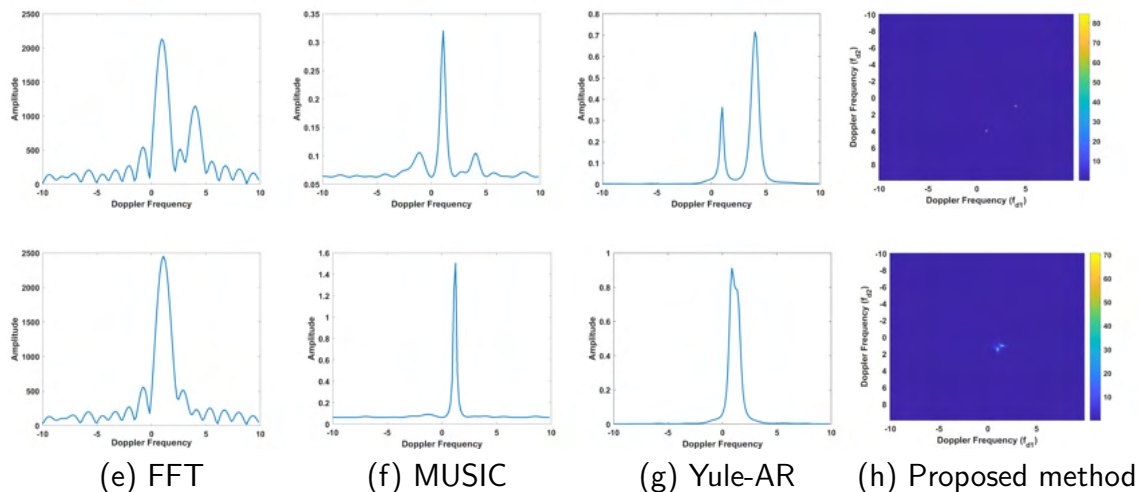


Figure 5.18: Comparison of Doppler frequency estimation using FFT, MUSIC, and proposed Capon method for a target is located at the range 3m and angle  $-30^\circ$  with  $\text{SNR} = 0\text{dB}$  and  $\beta_2 = \beta_1/2$ . In the first row  $f_{d_1} = 4\text{Hz}$ ,  $f_{d_2} = 1\text{Hz}$ , and  $\Delta f_d = 3\text{Hz}$ , while in the second row  $f_{d_1} = 1\text{Hz}$ ,  $f_{d_2} = 1.5\text{Hz}$ , and  $\Delta f_d = 0.5\text{Hz}$ .

two distinct peaks with a good frequency resolution and negligible side lobes. In contrast, our proposed algorithm's output shown in Fig. 5.17d presents two well-defined peaks with nearly imperceptible side lobes.

To demonstrate the effectiveness of our proposed Doppler frequency estimation method across varying amplitudes of Doppler frequency signals introduced by a target, we positioned a target at a distance of 3m and an angular location of  $-30$  degrees, characterized by  $\beta_1 = \frac{1+j}{\sqrt{2}}$  and  $\beta_2 = \frac{\beta_1}{2}$ . We explored two scenarios: In the first case, we set  $f_{d_1} = 4\text{Hz}$  and  $f_{d_2} = 1\text{Hz}$ , while in the second case, we configured  $f_{d_1} = 1.5\text{Hz}$  and  $f_{d_2} = 1\text{Hz}$ . In Figure 5.18, we conducted a comprehensive comparison of our proposed algorithm against FFT, MUSIC, and Yule-AR. The first row of the figure shows the simulation results for the first case, where we observe that FFT has broad frequency estimation lobes but can accurately estimate both frequencies. The MUSIC algorithm has narrow frequency estimation lobes, but it yields two frequency peaks corresponding to a lower amplitude frequency component. Notably, the Yule-AR method yields two peaks with more precise frequency estimation lobes. Therefore, our proposed algorithm offers sharp, impulse-like frequency peaks, thereby surpassing other methods in

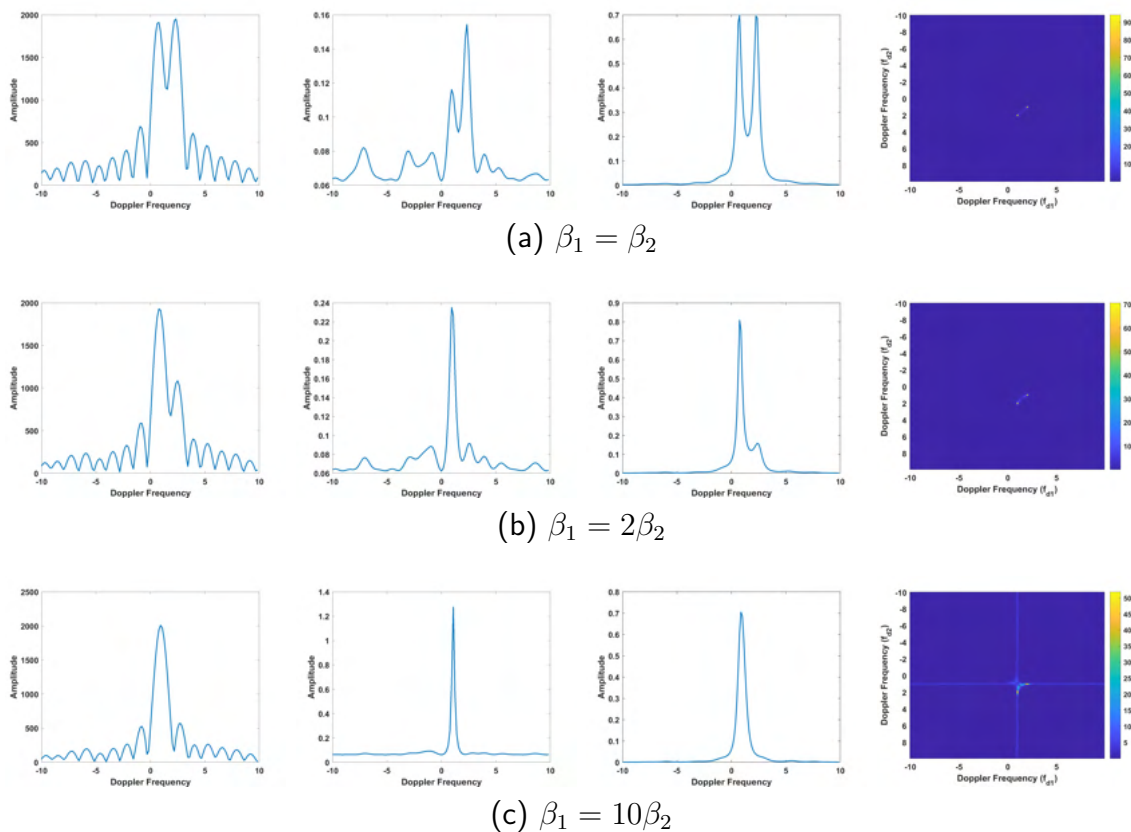


Figure 5.19: Comparison results of Doppler frequencies estimation with FFT (1st Column), MUSIC (2nd Column), and Yule-AR(3rd Column), and proposed method (4th Column) for a target placed at a distance of 3m and at an angle  $-30^\circ$  with  $\text{SNR} = 0\text{dB}$  and Doppler frequencies 2 Hz and 1 Hz for different ratios of  $\beta_1$  and  $\beta_2$ .

terms of frequency resolution. In the second row of the figure, we examine the simulation outcomes for the second case. Here, it is evident that FFT encounters difficulties in accurately detecting the  $f_{d_2}$  frequency component, primarily due to its poor resolution and the lower amplitude of this frequency component. Notably, both the MUSIC and Yule-AR algorithms are unable to detect the  $f_{d_2}$  frequency component, yielding only one peak corresponding to the  $f_{d_1}$  frequency component. In contrast, our proposed algorithm again shows two distinct peaks with negligible side lobes.

In our previous simulation, we examined scenarios where we varied the Doppler frequencies while keeping the amplitudes of the Doppler frequency signals constant. In the subsequent simulation, we will maintain fixed Doppler frequencies and vary the amplitudes of the Doppler frequency signals. For this simulation,

the target is placed at a distance of 3m and at an angular location of  $-30^\circ$ , with Doppler frequencies of 2 Hz and 1 Hz. Here, we consider three distinct scenarios: In the first scenario, we set  $\beta_1 = \frac{1+j}{\sqrt{2}}$  and  $\beta_2 = \beta_1$ . In the second scenario,  $\beta_1 = \frac{1+j}{\sqrt{2}}$  and  $\beta_2 = \frac{\beta_1}{2}$ , Lastly, in the third scenario,  $\beta_1 = \frac{1+j}{\sqrt{2}}$  and  $\beta_2 = \frac{\beta_1}{10}$ . The results of our proposed algorithm, along with FFT, MUSIC, and Yule-AR algorithms, are presented in Fig. 5.19. The first row of the figure displays the results for the first scenario, where it is evident that both the FFT and MUSIC algorithms can estimate frequencies but yield poor Doppler resolution. In contrast, Yule-AR and our proposed algorithms accurately detect two distinct peaks with negligible sidelobes. The second row of the figure displays the results for the second scenario, where it can be observed that both the FFT and our proposed algorithm can detect both frequency components. However, our proposed algorithm performs much better than FFT in terms of sidelobes levels and frequency resolution. On the other hand, the MUSIC and Yule-AR algorithms only detect one peak and fail to detect the second frequency component. Similarly, the last row of the figure presents the results for the third scenario. Here, FFT, MUSIC, and Yule-AR algorithms produce only one peak and completely fail to detect the second frequency component having a lower amplitude. In contrast, our proposed algorithm detects two distinct peaks with significantly lower sidelobes. In summary, the simulation results showcased the remarkable performance of our proposed algorithm, especially in scenarios where there is a substantial difference in the Doppler frequency signal amplitudes from a single target.

To evaluate the statistical performance of our proposed method, we consider two scenarios with a target placed at a distance of 3m and an angular location of  $-30^\circ$ . The target introduces Doppler frequencies of 2.333 Hz and 1.333 Hz in the reflected signal. We generate 10,000 Monte Carlo realizations of noise for each SNRs. In the first scenario,  $\beta_1 = \frac{1+j}{\sqrt{2}}$  and  $\beta_2 = \beta_1$  while in the second scenario  $\beta_1 = \frac{1+j}{\sqrt{2}}$  and  $\beta_2 = \frac{\beta_1}{2}$ . We have evaluated the Mean Square Estimation Error (MSEE) of the Doppler frequency estimation using our proposed algorithm, FFT,

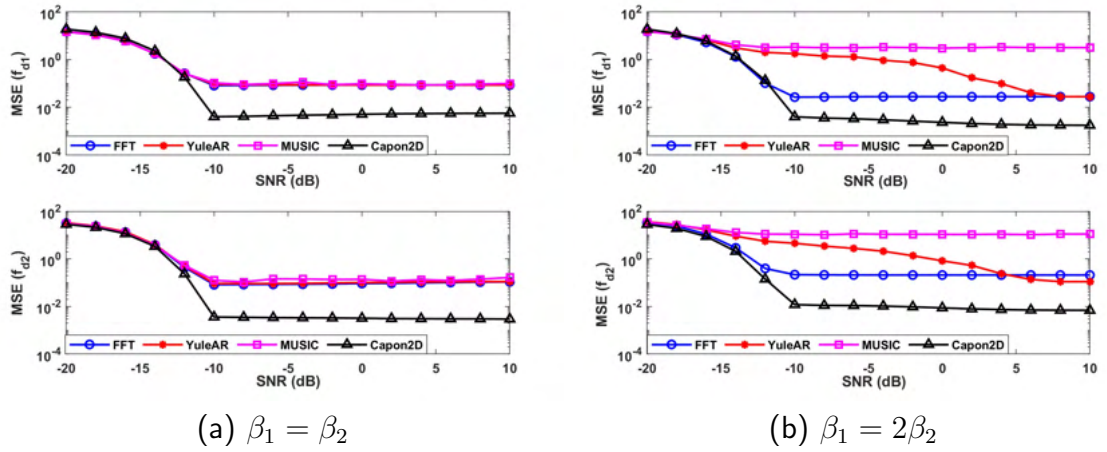


Figure 5.20: MSE comparison for Doppler estimation using FFT, MUSIC, Yule-AR, and proposed Capon method for a target is located at the range 3m and angle  $-30^\circ$  for a range of SNRs (-20dB to 10dB) with doppler frequencies  $f_{d1} = 1.333\text{Hz}$  and  $f_{d2} = 2.333\text{Hz}$ .

MUSIC, and Yule-AR. The results are illustrated in Fig. 5.20, revealing that our method's MSEE outperforms all other algorithms.

## 5.3 Results of Dehydration Status Monitoring

This section describes the major contribution of our work i.e., the creation of a new labeled FMCW radar dataset for non-invasive and non-contact based dehydration monitoring. Subsequently, we present a comprehensive comparative analysis that assesses the performance metrics of 77 GHz radar system.

### 5.3.1 Data Acquisition

In radar-based applications employing deep learning and machine learning, a significant challenge is the availability of labeled data or ground truth and acquiring a large set of labeled training data for radar applications is generally impractical. Due to the lack of publicly available labeled radar datasets suitable for dehydration assessment, we develop custom datasets. This lack of public datasets for non-invasive dehydration monitoring is due to the challenges in obtaining accurate dehydration labels. While collecting raw radar data is relatively straightforward, labeling this data requires a clinical setting. In such settings, trained medical professionals collect and analyze blood and urine samples to determine dehydration-related biomarkers, such as plasma/urine osmolality and urine specific gravity. To address these challenges and ensure the availability of accurately labeled data for our study, we developed custom datasets. These datasets provide the necessary ground truth for training and validating our radar-based dehydration monitoring system. We use Inras 77 GHz FMCW-MIMO radarbook [90, 91] with two transmit (Tx) and 16 receive (Rx) antennas for collecting new labeled FMCW radar dataset. The FMCW radar operates at a frequency of 77 GHz with a bandwidth of 2 GHz. We have collected two different data sets, named the Sports dataset and the Fasting Dataset. Please refer to Fig. 5.21.

#### **Sports Dataset:**

In the Sports dataset, the focus is on athletes/sports persons, specifically ultimate frisbee players. The study includes 15 subjects, with data collected at the

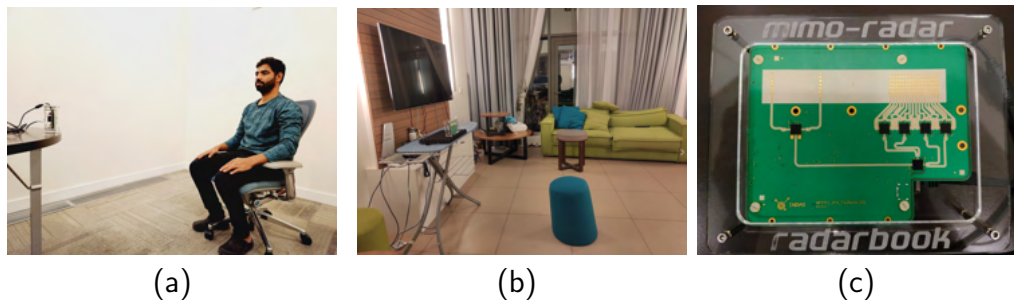


Figure 5.21: Experimental setup for dehydration monitoring using FMCW radar data collection for (a) Fasting Dataset and (b) Sports Dataset (c) Inras 77 GHz FMCW radar.

KAUST university during October month (in 2023). The hot and humid weather conditions during these months enhance the likelihood of dehydration. Subjects are asked to refrain from drinking water for 2 hours while playing frisbee. Data collection is conducted in two phases:

1. *Hydrated Phase*: Data is collected before the start of the sports activity. Participants were instructed to drink a sufficient amount of water at least 15 minutes prior to data collection to ensure they were fully hydrated.
2. *Dehydrated Phase*: Data is collected after the participants had engaged in the sports activity for 2 hours without consuming any water, ensuring they were fully dehydrated at the time of the second data collection phase. This data collection phase aimed to capture the physiological changes associated with dehydration.

During the data collection for the sports dataset, we use a single Tx antenna and 16 receiving antennas. Each FMCW radar pulse has a duration of  $102.4\mu\text{s}$ , with  $N_s = 256$  fast-time samples collected and  $N_c = 256$  chirp pulses are transmitted during the experiment. For the measurements, each subject is asked to sit on a chair at a distance of 1 meter from the radar for a duration of 1-2 minutes. FMCW radar positioned to face toward the subject and focus on the chest area for optimal results. However, in this work, we utilize data from a single receive antenna and a single chirp for dehydration monitoring.

## Fasting Dataset:

In the Fasting Dataset, data is collected from fasting subjects during the Ramadan, when subjects fast from sunrise until sunset. During this study, we collect the measurements from the 16 different subjects (in 2024) in KAUST academic campus. All subjects fasted for approximately 12 hours, from early morning until evening, under hot weather conditions. The progressive decrease in hydration levels throughout the day provided an ideal scenario for our measurements. We leveraged the natural decline in hydration levels from morning to evening, allowing us to collect five distinct measurements at regular intervals (2 hours gap between the measurements) from each fasting subject between sunrise and sunset. The measurements are collected as follows:

1. *8 AM Data or DeHydL0*: The first measurement was taken when the subjects were fully hydrated, having consumed water/food before sunrise.
2. *10 AM Data or DeHydL1*: The second measurement was taken, representing a partially hydrated state as the fasting period began to take effect.
3. *12 Noon Data or DeHydL2*: The third measurement was taken at midday, indicating a mildly dehydrated state as the fasting period progressed.
4. *2 PM Data or DeHydL3*: The fourth measurement was taken, reflecting a moderately dehydrated state as the effects of fasting continued.
5. *4 PM Data or DeHydL4*: The final measurement was taken, by which time the subjects are significantly dehydrated after nearly 12 hours of fasting.

This structured approach provides a comprehensive dataset that captures the progressive changes in hydration levels throughout the day, enabling a detailed analysis of dehydration patterns in fasting individuals.

Similar to the sports data collection, during the Fasting data collection, we use a single Tx antenna and 16 receiving antennas. Each FMCW radar pulse has a duration of  $512\mu\text{s}$ , with  $N_s = 256$  and  $N_c = 256$  chirp pulses are transmitted.

For the measurements, each subject is asked to sit on a chair at a distance of 1.2 meter from the radar for a duration of 1-2 minutes. FMCW radar positioned to face toward the subject and focus on the chest area for optimal results. However, in this work, we utilize data from a single receive antenna and a single chirp for dehydration monitoring.

### 5.3.2 Experimental Results

Data collection is conducted using the Inras 77G Hz radar, which produces a data matrix of size 256x256x16. For our analysis, we selected the fast-time samples of a specific chirp and receiving antenna, resulting in a 1x256 data vector. The initial step involves pre-processing the received demodulated data to remove noise and interference. This is achieved by passing the signal through a second-order section (SOS) Butterworth bandpass filter, isolating the target at 1.2 meters in the Fasting dataset. This filtered signal contains the relevant information related to the subject, or target of interest. Next, the filtered signal is fed to a wavelet scattering transform to extract meaningful features related to the target of interest. Finally, these extracted features are input into various machine learning classifiers, including Naive Bayes, KNN, SVM, and NN, to determine the dehydration status at 5 levels for the Fasting Dataset.

For the Fasting datasets, we utilized Gabor (analytic Morlet) wavelets to perform wavelet decomposition, with a Gaussian function serving as the corresponding low-pass filter. The invariance scale is set to the default i.e., half the signal length (128 samples). The constructed wavelet scattering network comprised two filter banks. Specifically, we use  $Q$  factor [8 1] for the Fasting Dataset. Although various settings for the invariance scale and wavelet octave resolution are tested, this configuration preserved the signal information best for classification.

For the Fasting dataset, the wavelet scattering network's output forms a matrix of size  $31 \times 8 \times 10000$ . Each slice of the tensor represents the scattering coefficients containing the dehydration information of the signal. These coeffi-

Class Name	Precision	Recall	F1 score
DeHydL0	0.7236	0.7200	0.7218
DeHydL1	0.6402	0.7650	0.6970
DeHydL2	0.7000	0.6300	0.6632
DeHydL3	0.8652	0.6100	0.7155
DeHydL4	0.6515	0.7850	0.7120
Accuracy	0.7020		
Macro-F1	0.7019		

Table 5.3: 77GHz radar Performance Metrics for Bayes

Class Name	Precision	Recall	F1 Score
DeHydL0	1.0000	0.9300	0.9637
DeHydL1	0.8889	1.0000	0.9412
DeHydL2	0.9898	0.9750	0.9824
DeHydL3	0.9948	0.9600	0.9771
DeHydL4	0.9899	0.9850	0.9875
Accuracy	0.9700		
Macro-F1	0.9704		

Table 5.4: 77GHz radar Performance Metrics for SVM

Class Name	Precision	Recall	F1 score
DeHydL0	0.9849	0.9800	0.9825
DeHydL1	0.9846	0.9600	0.9722
DeHydL2	0.9431	0.9950	0.9684
DeHydL3	0.9949	0.9750	0.9848
DeHydL4	0.9849	0.9800	0.9825
Accuracy	0.9780		
Macro-F1	0.9781		

Table 5.5: 77GHz radar Performance Metrics for KNN

Class Name	Precision	Recall	F1 Score
DeHydL0	0.9608	0.9800	0.9703
DeHydL1	0.9561	0.9800	0.9679
DeHydL2	0.9898	0.9750	0.9824
DeHydL3	0.9849	0.9800	0.9825
DeHydL4	0.9897	0.9650	0.9772
Accuracy	0.9760		
Macro-F1	0.9760		

Table 5.6: 77GHz radar Performance Metrics for NN

cients are also down-sampled based on the low-pass filter’s bandwidth, producing 8 time windows for each of the 31 scattering paths. To align with the classifiers data structure requirements and for better results, we reshaped this matrix into a  $10000 \times 248$ , where each column corresponds to a scattering path and a time window. The 248 columns result from the 8 time windows for each of the 10000 signals in the Fasting dataset. We employed a 5-fold cross-validation method for both datasets, splitting 90% of the data for training and reserving the remaining 10% for testing. Our proposed methodology was evaluated using Naive Bayes, SVM, KNN, and NN. All classifiers except Naive Bayes performed effectively in distinguishing dehydration levels, achieving high accuracy for the Fasting dataset (5-level classification). Notably, even basic classification methods demonstrated strong performance on the 5-level classification of the Fasting Dataset.

The performance of four different classifiers NN, KNN, Naive Bayes, and SVM

are evaluated using confusion matrix (shown in Fig. 5.22, 5.23, 5.24, 5.25) and standard classification metrics, including precision, recall, F1-score, accuracy, and misclassification rate as shown in Table 5.3, 5.4, 5.5, 5.6.

The Naive Bayes classifier exhibits an accuracy of 70.2%, with a macro-F1 score of 0.7019. It demonstrates moderate performance, with Class 3 (DeHydL3) achieving the highest precision (0.8652) and recall (0.6100). The overall F1 score for this class is 0.7155. However, other classes, such as Class 1 (DeHydL1) and Class 2 (DeHydL2), show relatively lower precision and recall scores, especially in comparison to the other classifiers. Class 1, for instance, has a precision of 0.6402 and recall of 0.7650, indicating room for improvement in the classifier's ability to correctly identify this class.

The SVM classifier significantly outperforms Naive Bayes with an impressive accuracy of 97.0% and a macro-F1 score of 0.9704. The precision and recall values across all classes are consistently high, particularly for Class 1 (DeHydL1), which achieved perfect recall (1.0000) and high precision (0.8889), resulting in an F1 score of 0.9412. Class 0 (DeHydL0) also performs exceptionally well with a precision of 1.0000 and recall of 0.9300, yielding an F1 score of 0.9637. Overall, the SVM classifier exhibits robust classification capabilities, showing excellent generalization across all classes (shown in Fig. 5.23).

The KNN classifier also performs admirably with an accuracy of 97.8% and a macro-F1 score of 0.9781. Precision and recall values for all classes are very strong, with Class 2 (DeHydL2) achieving near-perfect precision (0.9431) and recall (0.9950), leading to an outstanding F1 score of 0.9684. Similar to SVM, KNN shows consistent performance across the different classes, with Class 3 (DeHydL3) achieving an F1 score of 0.9848, reflecting its high precision (0.9949) and recall (0.9750). KNN, therefore, presents a competitive alternative to SVM with only marginal differences in performance.

The NN classifier achieves a near-identical performance to KNN, with an accuracy of 97.6% and a macro-F1 score of 0.9760. The precision and recall for

True Class	Predicted Class				
	DeHydL0	DeHydL1	DeHydL2	DeHydL3	DeHydL4
DeHydL0	196	2	1	1	
DeHydL1	1	196	1	1	1
DeHydL2	1	4	195		
DeHydL3	1	2		196	1
DeHydL4	5	1		1	193

Figure 5.22: Confusion matrix for Naive Bayes

True Class	Predicted Class				
	DeHydL0	DeHydL1	DeHydL2	DeHydL3	DeHydL4
DeHydL0	186	11	1		2
DeHydL1		200			
DeHydL2		4	195	1	
DeHydL3		8		192	
DeHydL4		2	1		197

Figure 5.23: Confusion matrix for SVM

True Class	Predicted Class				
	DeHydL0	DeHydL1	DeHydL2	DeHydL3	DeHydL4
DeHydL0	196		3		1
DeHydL1	2	192	4	1	1
DeHydL2	1		199		
DeHydL3		2	2	195	1
DeHydL4		1	3		196

Figure 5.24: Confusion matrix for KNN

True Class	Predicted Class				
	DeHydL0	DeHydL1	DeHydL2	DeHydL3	DeHydL4
DeHydL0	196	2	1	1	
DeHydL1	1	196	1	1	1
DeHydL2	1	4	195		
DeHydL3	1	2		196	1
DeHydL4	5	1		1	193

Figure 5.25: Confusion matrix for NN

most classes are close to the highest observed, with Class 0 (DeHydL0) yielding an F1 score of 0.9703, which is slightly lower than SVM and KNN. Class 1 (DeHydL1) exhibits a strong recall of 0.9800, resulting in a precision of 0.9561 and an F1 score of 0.9679. NN provides high overall performance but does not outperform the other models in any particular area.

Overall, integrating WST features significantly improved classification performance. The SVM, KNN, and NN classifiers achieved high accuracy and reliable classification results, making them well-suited for dehydration level detection based on radar data. The poor performance of Naive Bayes suggests that it is less effective for this application due to its underlying assumptions about feature independence. The results demonstrate the importance of selecting appropriate machine learning models and feature extraction techniques for robust non-invasive dehydration monitoring.

## Chapter 6

### Conclusion and Future Research Directions

#### 6.1 Summary of Contributions

This thesis has explored deep learning-based resolution enhancement in FL-MIMO SAR Imaging and bio-medical radar applications, presenting novel methodologies and experimental validations. The key contributions of this research are:

- Development of deep basis pursuit and convolutional decoder methods for FL-MIMO SAR imaging, improving azimuthal resolution beyond traditional techniques. Implementation and validation of deep learning-based SAR image reconstruction, demonstrating improved peak signal-to-noise ratio and structural similarity index over conventional methods.
- Application of radar-based physiological monitoring for heart rate and breathing rate estimation using signal processing techniques, showing good accuracy and reduced estimation errors.
- Development of a dehydration monitoring system using FMCW radar, validated through experimental data, achieving high classification accuracy. Collection and processing of custom dehydration data, allowing real-world evaluation of hydration status monitoring through radar signal analysis.
- Extensive data acquisition and implementation of a sophisticated hardware setup (INRAS MIMO Radarbook), and real-world testing for both SAR imaging and biomedical monitoring, alongside the development of a custom dehydration dataset for validating hydration status monitoring using radar.

The findings indicate that deep learning-based SAR imaging significantly enhances resolution, while biomedical radar applications show promise in non-contact health monitoring. However, challenges remain in real-world implementation, requiring further refinements and optimizations.

## 6.2 Limitations of the Study

Despite the promising results, several limitations must be acknowledged:

- **Hardware constraints:** The effectiveness of FL-MIMO SAR imaging is partly limited by radar hardware specifications, such as antenna array size and signal processing speed.
- **Computational complexity:** Deep learning-based methods, especially ConvDecoder, require significant computational resources, which may limit real-time applications.
- **Data dependency:** While deep learning eliminates the need for explicit priors, model performance is still dependent on the quality and diversity of training data.
- **Experimental variability:** Biomedical radar applications, especially dehydration monitoring, are affected by subject-specific differences and environmental conditions, which can lead to variations in accuracy.
- **Challenges in acquiring large-scale labeled biomedical radar data:** The reliance on controlled environments for data collection may affect generalization to diverse real-world scenarios.

Addressing these limitations will require a combination of hardware improvements, algorithmic optimizations, and more extensive real-world testing.

### 6.3 Future directions

The advancements presented in this research provide a strong foundation for future exploration in FMCW radar applications across automotive and biomedical domains. However, several challenges and opportunities remain that warrant further investigation. One key area for future work is enhancing FL-MIMO SAR for real-world deployment, focusing on optimizing deep learning-based imaging techniques for real-time execution on embedded hardware such as GPUs and FPGAs. Additionally, improving the robustness of radar systems in dynamic environments, including varying traffic conditions, urban landscapes, and extreme weather, will be crucial for ensuring reliable performance in autonomous vehicles. Integrating FL-MIMO SAR with other sensing modalities, such as LiDAR, cameras, and ultrasonic sensors, can further improve autonomous vehicle perception and scene reconstruction.

In the biomedical domain, radar-based physiological monitoring requires further validation through large-scale clinical trials to establish its reliability compared to traditional biomedical devices. Additionally, motion artifacts remain a challenge, necessitating the development of advanced filtering techniques and AI-driven correction models to enhance the accuracy of heart rate and breathing rate estimation. Future research can also explore personalized healthcare applications by leveraging adaptive machine learning models that tailor radar-based monitoring to individual patient characteristics, ensuring more accurate and user-friendly health assessments.

Another promising direction lies in advancements in radar signal processing and AI integration, where unsupervised and self-supervised learning approaches can reduce dependency on labeled data, making radar interpretation more efficient and scalable. Combining conventional radar signal processing with AI-based hybrid SAR reconstruction techniques can enhance image resolution while improving computational efficiency. Additionally, the exploration of multi-frequency FMCW radar for applications such as hydration monitoring in medical and sports

domains could unlock new capabilities in non-invasive physiological assessments.

Beyond these core areas, the methodologies developed in this research have the potential for cross-domain applications. In autonomous systems, continued advancements in FL-MIMO SAR imaging will be essential for navigating complex environments with higher precision. Similarly, radar-based smart healthcare solutions could be integrated into hospital settings, wearable devices, and home-based monitoring systems for continuous health tracking. Moreover, low-power radar processing using Edge AI can enable on-device radar inference, making FMCW radar viable for portable and IoT-based applications. Finally, the versatility of FMCW radar can be leveraged in security surveillance, industrial automation, and environmental monitoring, broadening its impact across multiple industries. By addressing these challenges and opportunities, future research can further refine radar-based solutions, paving the way for intelligent, real-time, and scalable innovations in automotive, healthcare, and beyond.

## 6.4 Final Remarks

This thesis demonstrates the transformative potential of deep learning in radar imaging and biomedical monitoring, significantly improving SAR resolution and non-contact physiological assessments. While deep learning-based methods show superior performance, real-world deployment still requires addressing computational efficiency, data variability, and hardware constraints.

The integration of a custom dehydration dataset has allowed for a more in depth understanding of hydration monitoring using radar, laying the groundwork for future research in non-invasive health diagnostics. By further expanding these datasets and refining deep learning approaches, more accurate, robust, and generalizable radar-based health monitoring solutions can be developed.

By bridging the gap between theoretical advancements and practical applications, future research can enable next-generation radar systems for healthcare, defense, and autonomous navigation, paving the way for real time, high resolu-

tion, and intelligent radar solutions.

## REFERENCES

- [1] M. Skolnik, *RADAR systems*. McGraw-Hill, 2001.
- [2] M.A.Richards, *Fundamentals of Radar Signal Processing*. New York, USA: McGraw-Hill Education, 2005.
- [3] M. Cheney and B. Borden, “Fundamentals of radar imaging,” in *SIAM*, 2009.
- [4] A.G.Stove, “Linear fmcw radar techniques,” *IEEE Proc. Radar Signal Processing*, vol. 139, pp. 343–350, 1992.
- [5] V. V. Kotte, S. Gishkori, M. Masood, and T. Y. Al-Naffouri, “Unsupervised deep basis pursuit based resolution enhancement for forward looking mimo sar imaging,” *IEEE Transactions on Aerospace and Electronic Systems*, vol. 59, no. 6, pp. 9080–9093, 2023.
- [6] —, “Enhanced imaging for forward looking mimo sar via un-supervised deep basis pursuit,” in *2022 IEEE Radar Conference (RadarConf22)*, 2022, pp. 1–5.
- [7] V. V. Kotte, S. Ahmed, M.-S. Alouini, and T. Y. Al-Naffouri, “Joint estimation of single target’s high amplitude difference doppler frequencies in fmcw radar,” *IEEE Transactions on Radar Systems*, vol. 2, pp. 112–124, 2024.
- [8] V. V. Kotte, S. Gishkori, and T. Y. Al-Naffouri, “Imaging for forward looking mimo sar with un-trained neural network,” in *15th European Conference on Synthetic Aperture Radar*, 2024, pp. 1–5.
- [9] Z.-S. Liu, H. Li, and J. Li, “Efficient implementation of capon and apes for spectral estimation,” *IEEE Transactions on Aerospace and Electronic Systems*, vol. 34, no. 4, pp. 1314–1319, 1998.
- [10] S. Jardak, M.-S. Alouini, T. Kiuru, M. Metso, and S. Ahmed, “Compact mmwave fmcw radar: Implementation and performance analysis,” *IEEE Aerospace and Electronic Systems Magazine*, vol. 34, no. 2, pp. 36–44, 2019.
- [11] W. M. Markus Andres, Karim Ishak and H.-L. Bloecher, “Extraction of micro-doppler signatures using automotive radar sensors,” *Frequenz*, vol. 66, pp. 11–12, 2012.
- [12] R. DeGroat, E. Dowling, and D. Linebarger, “The constrained music problem,” *IEEE Transactions on Signal Processing*, vol. 41, no. 3, pp. 1445–1449, 1993.

- [13] D. Kundu, "Modified music algorithm for estimating doa of signals," *Signal Processing*, vol. 48, no. 1, pp. 85–90, 1996. [Online]. Available: <https://www.sciencedirect.com/science/article/pii/0165168495001263>
- [14] J. Odendaal, E. Barnard, and C. Pistorius, "Two-dimensional superresolution radar imaging using the music algorithm," *IEEE Transactions on Antennas and Propagation*, vol. 42, no. 10, pp. 1386–1391, 1994.
- [15] S. Kay, *Modern Spectral Estimation: Theory and Application*. Englewood Cliffs N.J, 1988.
- [16] B. Kim, S. Kim, and J. Lee, "A novel dft-based doa estimation by a virtual array extension using simple multiplications for fmcw radar," *Sensors*, vol. 18, no. 5, 2018.
- [17] S. Jardak, S. Ahmed, and M.-S. Alouini, "Low complexity moving target parameter estimation for mimo radar using 2d-fft," *IEEE Transactions on Signal Processing*, vol. 65, no. 18, pp. 4745–4755, 2017.
- [18] J. Li and P. Stoica, "An adaptive filtering approach to spectral estimation and sar imaging," *IEEE Transactions on Signal Processing*, vol. 44, no. 6, pp. 1469–1484, 1996.
- [19] P. Stoica, Z. Wang, and J. Li, "Robust capon beamforming," *IEEE Signal Processing Letters*, vol. 10, no. 6, pp. 172–175, 2003.
- [20] P. Stoica, H. Li, and J. Li, "A new derivation of the apes filter," *IEEE Signal Processing Letters*, vol. 6, no. 8, pp. 205–206, 1999.
- [21] M. M. et al., "Requirements for next generation automotive radars," *2013 IEEE Radar Conference (RadarCon13)*, 2013.
- [22] T. Kan, G. xin, L. xiaowei, and L. zhongshan, "Implementation of real-time automotive sar imaging," in *2020 IEEE 11th Sensor Array and Multichannel Signal Processing Workshop (SAM)*, 2020, pp. 1–4.
- [23] A. Laribi, M. Hahn, J. Dickmann, and C. Waldschmidt, "Performance investigation of automotive sar imaging," in *2018 IEEE MTT-S International Conference on Microwaves for Intelligent Mobility (ICMIM)*, 2018, pp. 1–4.
- [24] S. Gishkori and B. Mulgrew, "Azimuth enhancement for automotive sar imaging," in *2018 International Conference on Radar (RADAR)*, 2018, pp. 1–5.
- [25] S. Gishkori, L. Daniel, M. Gashinova, and B. Mulgrew, "Imaging for a forward scanning automotive synthetic aperture radar," *IEEE Transactions on Aerospace and Electronic Systems*, vol. 55, no. 3, pp. 1420–1434, 2019.

- [26] S. Gishkori, D. Wright, L. Daniel, M. Gashinova, and B. Mulgrew, “Imaging moving targets for a forward-scanning automotive sar,” *IEEE Transactions on Aerospace and Electronic Systems*, vol. 56, no. 2, pp. 1106–1119, 2020.
- [27] S. Gishkori, D. Wright, L. Daniel, M. Gashinova, and M. Bernard, “Forward scanning automotive sar with moving targets,” in *2019 International Radar Conference (RADAR)*, 2019, pp. 1–4.
- [28] J. Li and P. Stoica, *MIMO Radar Signal Processing*. IEEE Press, 2009.
- [29] S.Rao, “Whitepaper: Mimoradar,” 2017. [Online]. Available: <https://www.ti.com/lit/an/swra554a/swra554a.pdf>
- [30] D. P. I. W. P. R. Y. Huang, P. V. Brennan and K. Hughes., “Fmcw based mimo imaging radar for maritime navigation,” in *Progress In Electromagnetics Research*, 2011.
- [31] J. H. G. Ender and J. Klare, “System architectures and algorithms for radar imaging by mimo-sar,” in *2009 IEEE Radar Conference*, 2009, pp. 1–6.
- [32] S. Gishkori and G. Leus, “Compressed sensing for block-sparse smooth signals,” in *2014 IEEE International Conference on Acoustics, Speech and Signal Processing (ICASSP)*, 2014, pp. 4166–4170.
- [33] S. Gishkori and B. Mulgrew, “Graph signal processing-based imaging for synthetic aperture radar,” *IEEE Geoscience and Remote Sensing Letters*, vol. 17, no. 2, pp. 232–236, 2020.
- [34] S. Gishkori, G. Leus, and V. Lottici, “Compressive sampling based differential detection of ultra wideband signals,” in *21st Annual IEEE International Symposium on Personal, Indoor and Mobile Radio Communications*, 2010, pp. 194–199.
- [35] R. Baraniuk and P. Steeghs, “Compressive radar imaging,” in *2007 IEEE Radar Conference*, 2007, pp. 128–133.
- [36] Y. Yu, A. P. Petropulu, and H. V. Poor, “Mimo radar using compressive sampling,” in *IEEE Journal of Selected Topics in Signal Processing*, vol. 4, no. 1, 2010, pp. 146–163.
- [37] G. Rilling, M. Davies, and B. Mulgrew, “Compressed sensing based compression of sar raw data,” in *SPARS’09 - Signal Processing with Adaptive Sparse Structured Representations*, 2009. [Online]. Available: <https://inria.hal.science/inria-00369560>
- [38] A. M. Alanazi, T. Ballal, M. Masood, and T. Y. Al-Naffouri, “Image deblurring using a perturbation-based regularization approach,” in *2017 25th European Signal Processing Conference (EUSIPCO)*, 2017, pp. 2383–2387.

- [39] A. Lucas, M. Iliadis, R. Molina, and A. K. Katsaggelos, “Using deep neural networks for inverse problems in imaging: Beyond analytical methods,” *IEEE Signal Processing Magazine*, vol. 35, no. 1, pp. 20–36, 2018.
- [40] G. E. Hinton, S. Osindero, and Y.-W. Teh, “A fast learning algorithm for deep belief nets,” *Neural Comput.*, vol. 18, no. 7, p. 1527–1554, 2006.
- [41] V. Jain and S. Seung, “Natural image denoising with convolutional networks,” in *Advances in Neural Information Processing Systems*, vol. 21. Curran Associates, Inc., 2008.
- [42] J. Xie, L. Xu, and E. Chen, “Image denoising and inpainting with deep neural networks,” in *Proceedings of the 26th International Conference on Neural Information Processing Systems - Volume 1*. Curran Associates Inc., 2012, p. 341–349.
- [43] R. Collobert and J. Weston, “A unified architecture for natural language processing: deep neural networks with multitask learning,” in *Proceedings of the 25th International Conference on Machine Learning*. Association for Computing Machinery, 2008, p. 160–167.
- [44] Z.-M. Liu, C. Zhang, and P. S. Yu, “Direction-of-arrival estimation based on deep neural networks with robustness to array imperfections,” *IEEE Transactions on Antennas and Propagation*, vol. 66, no. 12, pp. 7315–7327, 2018.
- [45] H. Huang, J. Yang, H. Huang, Y. Song, and G. Gui, “Deep learning for super-resolution channel estimation and doa estimation based massive mimo system,” *IEEE Transactions on Vehicular Technology*, vol. 67, no. 9, pp. 8549–8560, 2018.
- [46] E. Mason, B. Yonel, and B. Yazici, “Deep learning for radar,” in *2017 IEEE Radar Conference (RadarConf)*, 2017, pp. 1703–1708.
- [47] X. X. Zhu, S. Montazeri, M. Ali, Y. Hua, Y. Wang, L. Mou, Y. Shi, F. Xu, and R. Bamler, “Deep learning meets sar: Concepts, models, pitfalls, and perspectives,” *IEEE Geoscience and Remote Sensing Magazine*, vol. 9, no. 4, pp. 143–172, 2021.
- [48] J. Mun, H. Kim, and J. Lee, “A deep learning approach for automotive radar interference mitigation,” in *2018 IEEE 88th Vehicular Technology Conference (VTC-Fall)*, 2018, pp. 1–5.
- [49] Y. Dai, T. Jin, Y. Song, H. Du, and D. Zhao, “Srcnn-based enhanced imaging for low frequency radar,” in *2018 Progress in Electromagnetics Research Symposium (PIERS-Toyama)*, 2018, pp. 366–370.

- [50] J. Gao, B. Deng, Y. Qin, H. Wang, and X. Li, “Enhanced radar imaging using a complex-valued convolutional neural network,” *IEEE Geoscience and Remote Sensing Letters*, vol. 16, no. 1, pp. 35–39, 2019.
- [51] A. Stroescu, L. Daniel, D. Phippen, M. Cherniakov, and M. Gashinova, “Object detection on radar imagery for autonomous driving using deep neural networks,” in *2020 17th European Radar Conference (EuRAD)*, 2021, pp. 120–123.
- [52] Y. Dai, T. Jin, H. Li, Y. Song, and J. Hu, “Imaging enhancement via cnn in mimo virtual array-based radar,” *IEEE Transactions on Geoscience and Remote Sensing*, vol. 59, no. 9, pp. 7449–7458, 2021.
- [53] Y. Sun, Z. Huang, H. Zhang, Z. Cao, and D. Xu, “3drimr: 3d reconstruction and imaging via mmwave radar based on deep learning,” in *2021 IEEE International Performance, Computing, and Communications Conference (IPCCC)*, 2021, pp. 1–8.
- [54] H. Jing, S. Li, K. Miao, S. Wang, X. Cui, G. Zhao, and H. Sun, “Enhanced millimeter-wave 3-d imaging via complex-valued fully convolutional neural network,” *Electronics*, vol. 11, no. 1, 2022.
- [55] D. P. G. N.N. Aizenberg, Y.L. Ivaskiv, *Multivalued Threshold Functions in Boolean Complex-Threshold Functions and Their Generalization*. Cybern. Syst. Anal, 1971.
- [56] Hirose, *Complex-Valued Neural Networks: Advances and Applications*. Wiley, 2013.
- [57] R. G. W. Carrara and R. Majewski, *Spotlight Synthetic Aperture Radar*. Artech. House, 1995.
- [58] C. A. Balanis, *Antenna Theory: Analysis and Design*. Wiley, 2016.
- [59] J. Tamir, S. Yu, and M. Lustig, “Unsupervised deep basis pursuit: Learning inverse problems without ground-truth data,” 10 2019.
- [60] J. Schlemper, J. Caballero, J. Hajnal, A. Price, and D. Rueckert, “A deep cascade of convolutional neural networks for dynamic mr image reconstruction,” *IEEE Transactions on Medical Imaging*, vol. PP, 04 2017.
- [61] H. K. Aggarwal, M. P. Mani, and M. Jacob, “Modl: Model-based deep learning architecture for inverse problems,” *IEEE Transactions on Medical Imaging*, vol. 38, no. 2, pp. 394–405, 2019.
- [62] S. Boyd, N. Parikh, E. Chu, B. Peleato, and J. Eckstein, 2011, vol. 3, no. 1.

- [63] J. Lehtinen, J. Munkberg, J. Hasselgren, S. Laine, T. Karras, M. Aittala, and T. Aila, “Noise2noise: Learning image restoration without clean data,” 2018.
- [64] J. Batson and L. Royer, “Noise2self: Blind denoising by self-supervision,” 2019.
- [65] M. Z. Darestani and R. Heckel, “Accelerated mri with un-trained neural networks,” 2021. [Online]. Available: <https://arxiv.org/abs/2007.02471>
- [66] W. H. Organization, ““the impact of covid-19 on health and care workers: a closer look at deaths”,” *World Health Organization, Technical Document*, 2021.
- [67] S. Huynh, H.-P. Tan, and Y. Lee, “Towards unobtrusive mental well-being monitoring for independent-living elderly,” in *Proceedings of the 4th International on Workshop on Physical Analytics*. New York, NY, USA: Association for Computing Machinery, 2017, p. 1–6.
- [68] H. Rohmetra, N. Raghunath, P. Narang, V. Chamola, M. Guizani, and N. R. Lakkaniga, “Ai-enabled remote monitoring of vital signs for covid-19: methods, prospects and challenges,” *Computing*, vol. 105, no. 4, p. 783–809, 2021.
- [69] M. Nouman, S. Y. Khoo, M. A. P. Mahmud, and A. Z. Kouzani, “Recent advances in contactless sensing technologies for mental health monitoring,” *IEEE Internet of Things Journal*, vol. 9, no. 1, pp. 274–297, 2022.
- [70] V. L. Petrović, M. M. Janković, A. V. Lupšić, V. R. Mihajlović, and J. S. Popović-Božović, “High-accuracy real-time monitoring of heart rate variability using 24 ghz continuous-wave doppler radar,” *IEEE Access*, vol. 7, pp. 74 721–74 733, 2019.
- [71] P. Misans and M. Terauds, “Cw doppler radar based land vehicle speed measurement algorithm using zero crossing and least squares method,” in *2012 13th Biennial Baltic Electronics Conference*, 2012, pp. 161–164.
- [72] J. Tu and J. Lin, “Fast acquisition of heart rate in noncontact vital sign radar measurement using time-window-variation technique,” *IEEE Transactions on Instrumentation and Measurement*, vol. 65, no. 1, pp. 112–122, 2016.
- [73] H. Lee, B.-H. Kim, j. k. Park, and J.-G. Yook, “A novel vital-sign sensing algorithm for multiple subjects based on 24-ghz fmcw doppler radar,” *Remote Sensing*, vol. 11, p. 1237, 05 2019.
- [74] R. Coppola, S. Ahmed, and M.-S. Alouini, “Road users classification based on bi-frame micro-doppler with 24-ghz fmcw radar,” *Frontiers in Signal Processing*, vol. 2, 2022.

- [75] G. Brooker, "Understanding millimetre wave fmcw radars," *1st International Conference on Sensing Technology*, pp. 152–157, 01 2005.
- [76] S. I.V. Komarov, *Fundamentals of Short Range FM Radar*. Artech House Publishers, 2003.
- [77] H. F. Posada-Quintero, N. Reljin, A. Moutran, D. Georgopalis, E. C.-H. Lee, G. E. Giersch, D. J. Casa, and K. H. Chon, "Mild dehydration identification using machine learning to assess autonomic responses to cognitive stress," *Nutrients*, vol. 12, 2019.
- [78] S. Liaqat, K. Dashtipour, A. Rizwan, M. Usman, S. A. Shah, K. Arshad, K. Assaleh, and N. Ramzan, "Personalized wearable electrodermal sensing-based human skin hydration level detection for sports, health and wellbeing," *Scientific Report*, vol. 12, 2022. [Online]. Available: <https://doi.org/10.1038/s41598-022-07754-8>
- [79] N. Reljin, Y. Malyuta, G. Zimmer, Y. Mendelson, D. J. Blehar, C. E. Darling, and K. H. Chon, "Automatic detection of dehydration using support vector machines," in *2018 14th Symposium on Neural Networks and Applications (NEUREL)*, 2018, pp. 1–6.
- [80] N. K. Suryadevara, S. C. Mukhopadhyay, and L. Barrack, "Towards a smart non-invasive fluid loss measurement system," *Journal of medical systems*, vol. 39, pp. 1–10, 2015.
- [81] N. Kulkarni, C. Compton, J. Luna, and M. A. U. Alam, "A non-invasive context-aware dehydration alert system," in *Proceedings of the 22nd International Workshop on Mobile Computing Systems and Applications*. New York, NY, USA: Association for Computing Machinery, 2021, p. 157–159. [Online]. Available: <https://doi.org/10.1145/3446382.3448668>
- [82] S. Liaqat, K. Dashtipour, K. Arshad, and N. Ramzan, "Non invasive skin hydration level detection using machine learning," *Electronics*, vol. 9, no. 7, 2020. [Online]. Available: <https://www.mdpi.com/2079-9292/9/7/1086>
- [83] A. Rizwan, N. Abu Ali, A. Zoha, M. Ozturk, A. Alomainy, M. A. Imran, and Q. H. Abbasi, "Non-invasive hydration level estimation in human body using galvanic skin response," *IEEE Sensors Journal*, vol. 20, no. 9, pp. 4891–4900, 2020.
- [84] A. P. Carrieri, N. Haiminen, S. Maudsley-Barton, L.-J. Gardiner, B. Murphy, A. Mayes, S. Paterson, S. Grimshaw, M. Winn, C. Shand, and others., "Explainable ai reveals key changes in skin microbiome associated with menopause, smoking, aging and skin hydration," *Scientific report*, vol. 11, 2020.

- [85] S. I. Alekseev, I. Szabo, and M. C. Ziskin, “Millimeter wave reflectivity used for measurement of skin hydration with different moisturizers,” *Skin Research and Technology*, vol. 14, no. 4, pp. 390–396, Oct. 2008.
- [86] C. Baumgartner, P. A. Hasgall, F. Di Gennaro, E. Neufeld, B. Lloyd, M. C. Gosselin, D. Payne, A. Klingenböck, and N. Kuster, “It’is database for thermal and electromagnetic parameters of biological tissues,” April 2024, version 4.2. [Online]. Available: <https://itis.swiss/database>
- [87] B. Bank, “Converting infinite impulse response filters to parallel form [tips tricks],” *IEEE Signal Processing Magazine*, vol. 35, no. 3, pp. 124–130, 2018.
- [88] S. J. Orfanidis, *Introduction to signal processing*. USA: Prentice-Hall, Inc., 1995.
- [89] J. Andén and S. Mallat, “Deep scattering spectrum,” *IEEE Transactions on Signal Processing*, vol. 62, no. 16, pp. 4114–4128, 2014.
- [90] G. Inras, “Rdl-77g-tx2rx16 frontend (user manual).” [Online]. Available: [http://www.inras.at/uploads/media/RDL\\_77G\\_TX2RX1601.pdf](http://www.inras.at/uploads/media/RDL_77G_TX2RX1601.pdf)
- [91] Inras, “Radar system module.” [Online]. Available: <http://www.inras.at/en/products/modular-radar-system.html>

## APPENDICES

### A Proof of Case 2

For Case 2, the estimated value of  $\beta$  can be written as

$$\hat{\beta} = [1 \ 1] \begin{bmatrix} \alpha_{d_1,d_1} & \alpha_{d_1,2} \\ \alpha_{d_1,2}^* & \alpha_{2,2} \end{bmatrix}^{-1} \begin{bmatrix} \alpha_{d_1,d_1} & \alpha_{d_1,d_2} \\ \alpha_{2,d_1} & \alpha_{2,d_2} \end{bmatrix} \begin{bmatrix} \beta_1 \\ \beta_2 \end{bmatrix}.$$

By using the formula for inverting a  $2 \times 2$  matrix in the above equation and performing subsequent computations, we can obtain the estimated value of  $\beta$ , which can be written as

$$\hat{\beta} = \beta_1 + \frac{T_1 - T_2 - T_3 + T_4}{\eta} \beta_2, \quad (\text{A.1})$$

where

$$\begin{aligned} T_1 &= \alpha_{d_1,d_2} \alpha_{2,2}, T_2 = \alpha_{d_1,2} \alpha_{2,d_2}, \\ T_3 &= \alpha_{2,d_1} \alpha_{d_1,d_2}, T_4 = \alpha_{d_1,d_1} \alpha_{2,d_2}, \\ \text{and } \eta &= \alpha_{d_1,d_1} \alpha_{2,2} - |\alpha_{d_1,2}|^2. \end{aligned} \quad (\text{A.2})$$

To conduct a more in-depth analysis of (A.1), it is necessary to expand all  $T_i$  terms that involve the inverse of the covariance matrix  $\mathbf{R}_t$ . One way to approach

this is by utilizing the expression for the covariance matrix provided in (4.23)

$$\begin{aligned}
\mathbf{R}_t &= \mathbb{E} \{ \mathbf{Y}_t(\kappa) \mathbf{Y}_t^H(\kappa) \}, \\
&= \mathbb{E} \left\{ (\mathbf{c} \mathbf{a}^T(\theta) + \mathbf{V}_t) (\mathbf{c} \mathbf{a}^T(\theta) + \mathbf{V}_t)^H \right\}, \\
&= \sigma^2 \mathbf{I}_{N_c} + \mathbf{c} \mathbf{1} \mathbf{c}^H.
\end{aligned} \tag{A.3}$$

where  $\sigma^2$  is the variance of noise,  $\mathbf{I}_{N_c} \in \mathcal{R}^{N_c \times N_c}$  is the identity matrix and a column vector

$$\mathbf{c} = \begin{bmatrix} \mathbf{a}(f_{d_1}) & \mathbf{a}(f_{d_2}) \end{bmatrix} \begin{bmatrix} \beta_1 \\ \beta_2 \end{bmatrix}. \tag{A.4}$$

By setting  $\mathbf{B} = 1$  and  $\mathbf{A} = \sigma^2 \mathbf{I}_{N_c}$  in (A.3), the Woodbury identity can be applied to express the inversion of  $\mathbf{R}_t$  in a simplified form. The Woodbury identity is defined in [?]

$$(\mathbf{A} + \mathbf{C} \mathbf{B} \mathbf{C}^T)^{-1} = \mathbf{A}^{-1} - \mathbf{A}^{-1} \mathbf{C} (\mathbf{B}^{-1} + \mathbf{C}^T \mathbf{A}^{-1} \mathbf{C})^{-1} \mathbf{C}^T \mathbf{A}^{-1}.$$

Exploiting this identity, the inversion of the covariance matrix can be written in a simple form as

$$\begin{aligned}
\mathbf{R}_t^{-1} &= \frac{1}{\sigma^2} \left( \mathbf{I}_{N_c} - \frac{1}{\sigma^2} \mathbf{c} \left( 1 + \mathbf{c}^H \frac{\mathbf{I}_{N_c}}{\sigma^2} \mathbf{c} \right)^{-1} \mathbf{c}^H \right), \\
&= \frac{1}{\sigma^2} \left( \mathbf{I}_{N_c} - \frac{1}{\sigma^2} \mathbf{c} \left( \frac{\sigma^2}{\sigma^2 + \mathbf{c}^H \mathbf{c}} \right) \mathbf{c}^H \right), \\
&= \frac{1}{\sigma^2} \left( \mathbf{I}_{N_c} - \frac{\mathbf{c} \mathbf{c}^H}{\sigma^2 + \mathbf{c}^H \mathbf{c}} \right).
\end{aligned}$$

The use of this inverse of the covariance matrix presents a simplified approach for analyzing (A.1). Specifically, the terms in  $T_1$  and  $T_2$  share the same frequencies, as do the terms in  $T_3$  and  $T_4$ , albeit in a different order. Consequently, we may solve  $T_1$  and  $T_2$  concurrently and  $T_3$  and  $T_4$  concurrently, respectively. Therefore,

$T_1 - T_2$  in (A.1) can be resolved as

$$\begin{aligned}
T_1 - T_2 &= \frac{1}{\sigma^4} \left( \left( \gamma_{d_1, d_2} - \frac{\mathbf{a}^H(f_{d_1}) \mathbf{c} \mathbf{c}^H \mathbf{a}(f_{d_2})}{(\sigma^2 + \mathbf{c}^H \mathbf{c})} \right) \left( \gamma_{2, 2} - \frac{\mathbf{a}^H(f_2) \mathbf{c} \mathbf{c}^H \mathbf{a}(f_2)}{(\sigma^2 + \mathbf{c}^H \mathbf{c})} \right) \right. \\
&\quad \left. - \left( \gamma_{d_1, 2} - \frac{\mathbf{a}^H(f_{d_1}) \mathbf{c} \mathbf{c}^H \mathbf{a}(f_2)}{(\sigma^2 + \mathbf{c}^H \mathbf{c})} \right) \left( \gamma_{2, d_2} - \frac{\mathbf{a}^H(f_2) \mathbf{c} \mathbf{c}^H \mathbf{a}(f_{d_2})}{(\sigma^2 + \mathbf{c}^H \mathbf{c})} \right) \right) \\
&= \left( \frac{\gamma_{d_1, 2} \mathbf{a}^H(f_2) \mathbf{c} \mathbf{c}^H \mathbf{a}(f_{d_2})}{\sigma^4 (\sigma^2 + \mathbf{c}^H \mathbf{c})} - \frac{\gamma_{d_1, d_2} \mathbf{a}^H(f_2) \mathbf{c} \mathbf{c}^H \mathbf{a}(f_2)}{\sigma^4 (\sigma^2 + \mathbf{c}^H \mathbf{c})} + \frac{N_c \gamma_{d_1, d_2}}{\sigma^4} \right. \\
&\quad \left. - \frac{N_c \mathbf{a}^H(f_{d_1}) \mathbf{c} \mathbf{c}^H \mathbf{a}(f_{d_2})}{\sigma^4 (\sigma^2 + \mathbf{c}^H \mathbf{c})} + \frac{\gamma_{2, d_2} \mathbf{a}^H(f_{d_1}) \mathbf{c} \mathbf{c}^H \mathbf{a}(f_2)}{\sigma^4 (\sigma^2 + \mathbf{c}^H \mathbf{c})} - \frac{\gamma_{d_1, 2} \gamma_{2, d_2}}{\sigma^4} \right), \quad (\text{A.5})
\end{aligned}$$

where  $\gamma_{p, q} = \mathbf{a}^H(f_p) \mathbf{a}(f_q)$ . Further replacing the value of  $\mathbf{c}$ ,  $T_1 - T_2$  can be simplified to

$$\begin{aligned}
T_1 - T_2 &= \frac{1}{\sigma^4} \left( N_c \gamma_{d_1, d_2} + \frac{|\beta_1|^2 (-N_c^2 \gamma_{d_1, d_2} + N_c \gamma_{2, d_2} \gamma_{d_1, 2})}{(\sigma^2 + \mathbf{c}^H \mathbf{c})} \right. \\
&\quad + \frac{|\beta_2|^2 (-N_c^2 \gamma_{d_1, d_2} + N_c \gamma_{2, d_2} \gamma_{d_1, 2})}{(\sigma^2 + \mathbf{c}^H \mathbf{c})} - \gamma_{d_1, 2} \gamma_{2, d_2} \\
&\quad + \frac{\beta_1 \beta_2^* (N_c |\gamma_{2, d_1}|^2 - N_c^3 - \gamma_{d_1, d_2} \gamma_{2, d_1} \gamma_{d_2, 2} + N_c |\gamma_{2, d_2}|^2)}{(\sigma^2 + \mathbf{c}^H \mathbf{c})} \\
&\quad \left. + \frac{\beta_1^* \beta_2 (-N_c (\gamma_{d_1, d_2})^2 + \gamma_{d_1, 2} \gamma_{2, d_2} \gamma_{d_1, d_2})}{(\sigma^2 + \mathbf{c}^H \mathbf{c})} \right) \quad (\text{A.6})
\end{aligned}$$

Finally, employing  $\sigma^2 + \mathbf{c}^H \mathbf{c}$  most of the terms will be cancelled and (A.6) can be written in more compact form as

$$\begin{aligned}
T_1 - T_2 &= \frac{1}{\sigma^4 (\sigma^2 + \mathbf{c}^H \mathbf{c})} \left( \sigma^2 (N_c \gamma_{d_1, d_2} - \gamma_{d_1, 2} \gamma_{2, d_2}) + \right. \\
&\quad \beta_1 \beta_2^* \left( -N_c^3 - \gamma_{d_1, d_2} \gamma_{2, d_1} \gamma_{d_2, 2} - \gamma_{d_1, 2} \gamma_{2, d_2} \gamma_{d_2, d_1} + \right. \\
&\quad \left. \left. N_c |\gamma_{2, d_2}|^2 + N_c |\gamma_{2, d_1}|^2 + N_c |\gamma_{d_2, d_1}|^2 \right) \right). \quad (\text{A.7})
\end{aligned}$$

Similarly,  $T_4 - T_3$  can be simplified as

$$\begin{aligned}
T_4 - T_3 &= \frac{1}{\sigma^4} \left( \left( N_c - \frac{\mathbf{a}^H(f_{d_1})\mathbf{c}\mathbf{c}^H\mathbf{a}(f_{d_1})}{(\sigma^2 + \mathbf{c}^H\mathbf{c})} \right) \left( \gamma_{2,d_2} - \frac{\mathbf{a}^H(f_2)\mathbf{c}\mathbf{c}^H\mathbf{a}(f_{d_2})}{(\sigma^2 + \mathbf{c}^H\mathbf{c})} \right) \right. \\
&\quad \left. - \left( \gamma_{2,d_1} - \frac{\mathbf{a}^H(f_2)\mathbf{c}\mathbf{c}^H\mathbf{a}(f_{d_1})}{(\sigma^2 + \mathbf{c}^H\mathbf{c})} \right) \left( N_c - \frac{\mathbf{a}^H(f_{d_1})\mathbf{c}\mathbf{c}^H\mathbf{a}(f_{d_2})}{(\sigma^2 + \mathbf{c}^H\mathbf{c})} \right) \right) \\
&= \left( -\frac{\gamma_{2,d_2}\mathbf{a}^H(f_{d_1})\mathbf{c}\mathbf{c}^H\mathbf{a}(f_{d_1})}{\sigma^4(\sigma^2 + \mathbf{c}^H\mathbf{c})} + \frac{N_c\gamma_{2,d_2}}{\sigma^4} - \frac{N_c\mathbf{a}^H(f_2)\mathbf{c}\mathbf{c}^H\mathbf{a}(f_{d_2})}{\sigma^4(\sigma^2 + \mathbf{c}^H\mathbf{c})} \right. \\
&\quad \left. + \frac{\gamma_{d_1,d_2}\mathbf{a}^H(f_2)\mathbf{c}\mathbf{c}^H\mathbf{a}(f_{d_1})}{\sigma^4(\sigma^2 + \mathbf{c}^H\mathbf{c})} + \frac{\gamma_{2,d_1}\mathbf{a}^H(f_{d_1})\mathbf{c}\mathbf{c}^H\mathbf{a}(f_{d_2})}{\sigma^4(\sigma^2 + \mathbf{c}^H\mathbf{c})} - \frac{\gamma_{2,d_1}\gamma_{d_1,d_2}}{\sigma^4} \right). \quad (\text{A.8})
\end{aligned}$$

Next, employing the value of  $\mathbf{c}$ , (A.8) can be further simplified

$$T_4 - T_3 = \frac{\sigma^2(-\gamma_{d_1,d_2}\gamma_{2,d_1} + N_c\gamma_{2,d_2})}{\sigma^4(\sigma^2 + \mathbf{c}^H\mathbf{c})} \quad (\text{A.9})$$

Observing (A.7) and (A.9), we see the following facts

$$\begin{aligned}
\beta_1\beta_2^*N_c|\gamma_{d_2,d_1}|^2 &\gg \sigma^2N_c\gamma_{d_1,d_2} \\
\beta_1\beta_2^*N_c|\gamma_{2,d_2}|^2 &\gg \sigma^2N_c\gamma_{2,d_2} \\
\beta_1\beta_2^*N_c^3 &\gg \sigma^2\gamma_{d_1,2}\gamma_{2,d_2} \\
\text{and } \beta_1\beta_2^*N_c|\gamma_{2,d_1}|^2 &\gg \sigma^2\gamma_{d_1,d_2}\gamma_{2,d_1}.
\end{aligned}$$

Exploiting, these facts we can write

$$\begin{aligned}
T1 - T2 - T3 + T4 &= \frac{1}{\sigma^4(\sigma^2 + \mathbf{c}^H\mathbf{c})} \left( N_c\beta_1\beta_2^* \left( |\gamma_{2,d_1}|^2 \right. \right. \\
&\quad \left. \left. + |\gamma_{d_2,d_1}|^2 + |\gamma_{2,d_2}|^2 - N_c^2 - \frac{2\Re(\gamma_{d_1,d_2}\gamma_{2,d_1}\gamma_{d_2,2})}{N_c} \right) \right. \\
&\quad \left. + \sigma^2 \left( N_c\gamma_{2,d_2} + N_c\gamma_{d_1,d_2} - \gamma_{d_1,d_2}\gamma_{2,d_1} - \gamma_{d_1,2}\gamma_{2,d_2} \right) \right) \\
&= \frac{N_c\beta_1\beta_2^*}{\sigma^4(\sigma^2 + \mathbf{c}^H\mathbf{c})} \left( |\gamma_{2,d_2}|^2 + |\gamma_{2,d_1}|^2 + |\gamma_{d_2,d_1}|^2 - N_c^2 \right. \\
&\quad \left. - \frac{2\Re(\gamma_{d_1,d_2}\gamma_{2,d_1}\gamma_{d_2,2})}{N_c} \right). \quad (\text{A.10})
\end{aligned}$$

Now, we will analyze the denominator term given in (A.8) i.e.,

$$\begin{aligned}
\eta &= \frac{1}{\sigma^4} \left( \left( \gamma_{d_1, d_1} - \frac{\mathbf{a}^H(f_{d_1}) \mathbf{c} \mathbf{c}^H \mathbf{a}(f_{d_1})}{(\sigma^2 + \mathbf{c}^H \mathbf{c})} \right) \left( \gamma_{2, 2} - \frac{\mathbf{a}^H(f_2) \mathbf{c} \mathbf{c}^H \mathbf{a}(f_2)}{(\sigma^2 + \mathbf{c}^H \mathbf{c})} \right) \right. \\
&\quad \left. - \left( \gamma_{d_1, 2} - \frac{\mathbf{a}^H(f_{d_1}) \mathbf{c} \mathbf{c}^H \mathbf{a}(f_2)}{(\sigma^2 + \mathbf{c}^H \mathbf{c})} \right) \left( \gamma_{2, d_1} - \frac{\mathbf{a}^H(f_2) \mathbf{c} \mathbf{c}^H \mathbf{a}(f_{d_1})}{(\sigma^2 + \mathbf{c}^H \mathbf{c})} \right) \right) \\
&= \frac{1}{\sigma^4} \left( -|\gamma_{d_1, 2}|^2 - \frac{N_c \mathbf{a}^H(f_2) \mathbf{c} \mathbf{c}^H \mathbf{a}(f_2)}{(\sigma^2 + \mathbf{c}^H \mathbf{c})} - \frac{N_c \mathbf{a}^H(f_{d_1}) \mathbf{c} \mathbf{c}^H \mathbf{a}(f_{d_1})}{(\sigma^2 + \mathbf{c}^H \mathbf{c})} \right. \\
&\quad \left. + \frac{\gamma_{d_1, 2} \mathbf{a}^H(f_2) \mathbf{c} \mathbf{c}^H \mathbf{a}(f_{d_1})}{(\sigma^2 + \mathbf{c}^H \mathbf{c})} + \frac{\gamma_{2, d_1} \mathbf{a}^H(f_{d_1}) \mathbf{c} \mathbf{c}^H \mathbf{a}(f_2)}{(\sigma^2 + \mathbf{c}^H \mathbf{c})} + N_c^2 \right). \quad (\text{A.11})
\end{aligned}$$

Further, employing the value of  $\mathbf{c}$  in the numerator terms, (A.11) can be further simplified as

$$\begin{aligned}
\eta &= \frac{1}{\sigma^4} \left( N_c^2 - |\gamma_{d_1, 2}|^2 + \frac{N_c \beta_1^2}{(\sigma^2 + \mathbf{c}^H \mathbf{c})} (|\gamma_{2, d_1}|^2 - N_c^2) \right. \\
&\quad \left. - \frac{N_c \beta_2^2}{(\sigma^2 + \mathbf{c}^H \mathbf{c})} \left( |\gamma_{2, d_2}|^2 + |\gamma_{d_1, d_2}|^2 - \frac{2\Re(\gamma_{2, d_2} \gamma_{d_1, 2} \gamma_{d_2, d_1})}{N_c} \right) \right. \\
&\quad \left. + \frac{2\Re(\beta_1 \beta_2^* (-N_c^2 \gamma_{d_2, d_1} + |\gamma_{2, d_1}|^2 \gamma_{d_2, d_1}))}{(\sigma^2 + \mathbf{c}^H \mathbf{c})} \right) \quad (\text{A.12})
\end{aligned}$$

Finally, working with  $\sigma^2 + \mathbf{c}^H \mathbf{c}$  in the denominator, (A.12) can be further simplified as

$$\begin{aligned}
\eta &= \frac{1}{\sigma^4 (\sigma^2 + \mathbf{c}^H \mathbf{c})} \left( N_c \beta_2^2 \left( N_c^2 - |\gamma_{2, d_2}|^2 - |\gamma_{2, d_1}|^2 - |\gamma_{d_2, d_1}|^2 \right. \right. \\
&\quad \left. \left. + \frac{2\Re(\gamma_{d_1, d_2} \gamma_{2, d_1} \gamma_{d_2, 2})}{N_c} \right) + \sigma^2 (N_c^2 - |\gamma_{d_1, 2}|^2) \right) \quad (\text{A.13})
\end{aligned}$$

Observing (A.13), at typical SNR=10 dB or SNR=0 dB, following facts can be observed

$$|\beta_2|^2 N_c^3 \gg \sigma^2 N_c^2 \text{ and } N_c |\beta_2|^2 |\gamma_{2, d_1}|^2 \gg \sigma^2 |\gamma_{d_1, 2}|^2.$$

Exploiting, these facts we can write

$$\eta = \frac{N_c |\beta_2|^2}{\sigma^4 (\sigma^2 + \mathbf{c}^H \mathbf{c})} \left( N_c^2 - |\gamma_{2,d_2}|^2 - |\gamma_{2,d_1}|^2 - |\gamma_{d_2,d_1}|^2 + \frac{2\Re(\gamma_{d_1,d_2} \gamma_{2,d_1} \gamma_{d_2,2})}{N_c} \right) \quad (\text{A.14})$$

Substituting (A.14) and (A.10) in (A.1) results

$$\begin{aligned} \hat{\beta} &\approx \beta_1 + \frac{-\beta_1 \beta_2^*}{|\beta_2|^2} \beta_2 \\ &= 0. \end{aligned} \quad (\text{A.15})$$

## B Proof of Case 4

For Case 4, the estimated value of  $\beta$  can be written as

$$\hat{\beta} = [1 \ 1] \begin{bmatrix} \alpha_{1,1} & \alpha_{1,2} \\ \alpha_{1,2}^* & \alpha_{2,2} \end{bmatrix}^{-1} \begin{bmatrix} \alpha_{1,d_1} & \alpha_{1,d_2} \\ \alpha_{2,d_1} & \alpha_{2,d_2} \end{bmatrix} \begin{bmatrix} \beta_1 \\ \beta_2 \end{bmatrix}.$$

By using the formula for inverting a  $2 \times 2$  matrix in the above equation and performing subsequent computations, we can obtain the estimated value of  $\beta$ , which can be written as

$$\hat{\beta} = \frac{(S_1 - S_2 - S_3 + S_4) \beta_1 + (S_5 - S_6 - S_7 + S_8) \beta_2}{\eta}, \quad (\text{B.1})$$

$$\text{where } S_1 = \alpha_{2,2} \alpha_{1,d_1}, S_2 = \alpha_{1,2} \alpha_{2,d_1}, S_3 = \alpha_{2,1} \alpha_{1,d_1},$$

$$S_4 = \alpha_{1,1} \alpha_{2,d_1}, S_5 = \alpha_{2,2} \alpha_{1,d_2}, S_6 = \alpha_{1,2} \alpha_{2,d_2},$$

$$S_7 = \alpha_{2,1} \alpha_{1,d_2}, S_8 = \alpha_{1,1} \alpha_{2,d_2},$$

$$\text{and } \eta_1 = \alpha_{1,1} \alpha_{2,2} - |\alpha_{1,2}|^2. \quad (\text{B.2})$$

Similarly, employing  $|\beta_2|^2 N_c^2 \gamma_{1,d_1} \gg \sigma^2 N_c \gamma_{1,d_1}$  and  $|\beta_2|^2 N_c \gamma_{1,2} \gamma_{2,d_1} \gg \sigma^2 \gamma_{1,2} \gamma_{2,d_1}$ ,  $S_1 - S_2$  can be simplified as

$$\begin{aligned}
S_1 - S_2 = & \frac{1}{\sigma^4(\sigma^2 + \mathbf{c}^H \mathbf{c})} \left( |\beta_2|^2 \left( N_c^2 \gamma_{1,d_1} + \gamma_{1,2} \gamma_{2,d_2} \gamma_{d_2,d_1} \right. \right. \\
& + \gamma_{2,d_1} \gamma_{1,d_2} \gamma_{d_2,2} - N_c \gamma_{1,2} \gamma_{2,d_1} - N_c \gamma_{1,d_2} \gamma_{d_2,d_1} - \gamma_{1,d_1} |\gamma_{2,d_2}|^2 \left. \right) \\
& + \beta_1^* \beta_2 \left( N_c \gamma_{d_1,d_2} \gamma_{1,d_1} + N_c \gamma_{1,2} \gamma_{2,d_2} - N_c^2 \gamma_{1,d_2} - \gamma_{1,d_1} \gamma_{2,d_2} \gamma_{d_1,2} \right. \\
& \left. \left. + \gamma_{2,d_1} \gamma_{1,d_2} \gamma_{d_1,2} - \gamma_{d_1,d_2} \gamma_{1,2} \gamma_{2,d_1} \right) \right) \quad (\text{B.3})
\end{aligned}$$

Similarly, employing  $|\beta_2|^2 N_c^2 \gamma_{2,d_1} \gg \sigma^2 N_c \gamma_{2,d_1}$  and  $|\beta_2|^2 N_c \gamma_{2,1} \gamma_{1,d_1} \gg \sigma^2 \gamma_{2,1} \gamma_{1,d_1}$ ,  $S_4 - S_3$  can be simplified as

$$\begin{aligned}
S_4 - S_3 = & \frac{1}{\sigma^4(\sigma^2 + \mathbf{c}^H \mathbf{c})} \left( |\beta_2|^2 \left( N_c^2 \gamma_{2,d_1} - N_c \gamma_{2,d_2} \gamma_{d_2,d_1} \right. \right. \\
& - \gamma_{2,d_1} |\gamma_{1,d_2}|^2 + \gamma_{2,1} \gamma_{1,d_2} \gamma_{d_2,d_1} + \gamma_{1,d_1} \gamma_{2,d_2} \gamma_{d_2,1} - N_c \gamma_{2,1} \gamma_{1,d_1} \left. \right) \\
& + \beta_1^* \beta_2 \left( N_c \gamma_{d_1,d_2} \gamma_{2,d_1} - N_c^2 \gamma_{2,d_2} - \gamma_{2,d_1} \gamma_{1,d_2} \gamma_{d_1,1} + N_c \gamma_{2,1} \gamma_{1,d_2} \right. \\
& \left. \left. + \gamma_{1,d_1} \gamma_{2,d_2} \gamma_{d_1,1} - \gamma_{d_1,d_2} \gamma_{2,1} \gamma_{1,d_1} \right) \right) \quad (\text{B.4})
\end{aligned}$$

Similarly, employing  $|\beta_1|^2 N_c^2 \gamma_{1,d_2} \gg \sigma^2 N_c \gamma_{1,d_2}$  and  $|\beta_1|^2 N_c \gamma_{1,2} \gamma_{2,d_2} \gg \sigma^2 \gamma_{1,2} \gamma_{2,d_2}$ ,  $S_5 - S_6$  can be simplified as

$$\begin{aligned}
S_5 - S_6 = & \frac{1}{\sigma^4(\sigma^2 + \mathbf{c}^H \mathbf{c})} \left( |\beta_1|^2 \left( N_c^2 \gamma_{1,d_2} - N_c \gamma_{1,d_1} \gamma_{d_1,d_2} \right. \right. \\
& - \gamma_{1,d_2} |\gamma_{2,d_1}|^2 + \gamma_{1,2} \gamma_{2,d_1} \gamma_{d_1,d_2} + \gamma_{2,d_2} \gamma_{1,d_1} \gamma_{d_1,2} - N_c \gamma_{1,2} \gamma_{2,d_2} \left. \right) \\
& + \beta_1 \beta_2^* \left( N_c \gamma_{1,2} \gamma_{2,d_1} - N_c^2 \gamma_{1,d_1} - \gamma_{1,d_2} \gamma_{2,d_1} \gamma_{d_2,2} + N_c \gamma_{d_2,d_1} \gamma_{1,d_2} \right. \\
& \left. \left. + \gamma_{2,d_2} \gamma_{1,d_1} \gamma_{d_2,2} - \gamma_{d_2,d_1} \gamma_{1,2} \gamma_{2,d_2} \right) \right) \quad (\text{B.5})
\end{aligned}$$

Similarly, employing  $|\beta_1|^2 N_c^2 \gamma_{2,d_2} \gg \sigma^2 N_c \gamma_{2,d_2}$  and  $|\beta_1|^2 N_c \gamma_{2,1} \gamma_{1,d_2} \gg \sigma^2 \gamma_{2,1} \gamma_{1,d_2}$ ,  $S_8 - S_7$  can be simplified as

$$\begin{aligned}
S_8 - S_7 = & \frac{1}{\sigma^4(\sigma^2 + \mathbf{c}^H \mathbf{c})} \left( |\beta_1|^2 \left( N_c^2 \gamma_{2,d_2} - N_c \gamma_{2,d_1} \gamma_{d_1,d_2} \right. \right. \\
& - \gamma_{2,d_2} |\gamma_{1,d_1}|^2 + \gamma_{2,1} \gamma_{1,d_1} \gamma_{d_1,d_2} + \gamma_{1,d_2} \gamma_{2,d_1} \gamma_{d_1,1} - N_c \gamma_{2,1} \gamma_{1,d_2} \Big) \\
& + \beta_1 \beta_2^* \left( N_c \gamma_{2,1} \gamma_{1,d_1} + N_c \gamma_{d_2,d_1} \gamma_{2,d_2} - N_c^2 \gamma_{2,d_1} - \gamma_{2,d_2} \gamma_{1,d_1} \gamma_{d_2,1} \right. \\
& \left. \left. + \gamma_{1,d_2} \gamma_{2,d_1} \gamma_{d_2,1} - \gamma_{d_2,d_1} \gamma_{2,1} \gamma_{1,d_2} \right) \right) \quad (\text{B.6})
\end{aligned}$$

Substituting (B.3), (B.4), (B.5) and (B.6) in (B.1) results

$$\hat{\beta} = 0. \quad (\text{B.7})$$

## C Papers Submitted and Under Preparation

### Publications

- **V. V. Kotte**, S. Ahmed, M. S. Alouini and T. Y. Al-Naffouri, “Joint Estimation of Single Target’s High Amplitude Difference Doppler Frequencies in FMCW Radar”, in IEEE Transactions on Radar Systems, vol. 2, pp. 112-124, 2024.
- **V. V. Kotte**, S. Gishkori, and T. Y. Al-Naffouri, “Imaging for Forward Looking MIMO SAR with Un-Trained Neural Network”, 15th European Conference on Synthetic Aperture Radar, Munich, Germany, 2024.
- **V. V. Kotte**, S. Gishkori, M. Masood and T. Y. Al-Naffouri, “Unsupervised Deep Basis Pursuit Based Resolution Enhancement for Forward Looking MIMO SAR Imaging,” in IEEE Transactions on Aerospace and Electronic Systems, vol. 59, no. 6, pp. 9080-9093, Dec. 2023.
- **V. V. Kotte**, S. Gishkori, M. Masood and T. Y. Al-Naffouri, “Enhanced Imaging for Forward Looking MIMO SAR Via Un-Supervised Deep Basis Pursuit,”

2022 IEEE Radar Conference (RadarConf22), New York City, NY, USA, 2022.

## Papers Under Preparation

- **V. V. Kotte**, M. M. U. Rahman, S. Ahmed, T. Y. Al-Naffouri and M. S. Alouini, “Non-Contact Dehydration Monitoring with Wavelet Scattering Transform Using FMCW Radar,” (draft available).
- Ruiqi Wang, Pinjun Zheng, **Vijith Varma Kotte**, Sakandar Rauf, Yiming Yang, Muhammad Mahboob Ur Rahman, Tareq Y. Al-Naffouri, Atif Shamim “Electromagnetically Reconfigurable Fluid Antenna System for Wireless Communications: Design, Modeling, Algorithm, Fabrication, and Experiment” (draft available).